2-P

NAS9-12077
T-638
Line Item No. 7
MA-129T
R-9136
NASA CR-134388

FINAL REPORT

ADVANCED ACOUSTIC CAVITY TECHNOLOGY

June 1974

by

W. S. Hines, C. L. Oberg, and L. Kusak

Rocketdyne Division, Rockwell International
6633 Canoga Avenue, Canoga Park, California

Prepared For

National Aeronautics and Space Administration

Lyndon B. Johnson Space Center

Contract NAS9-12077

R. C. Kahl, Technical Monitor

NAS9-12077
T-638
Line Item No. 7
MA-129T
R-9136

FINAL REPORT

ADVANCED ACOUSTIC CAVITY TECHNOLOGY

June 1974

by

W. S. Hines, C. L. Oberg, and L. Kusak

Rocketdyne Division, Rockwell International
6633 Canoga Avenue, Canoga Park, California

Prepared For

National Aeronautics and Space Administration

Lyndon B. Johnson Space Center

Contract NAS9-12077

R. C. Kahl, Technical Monitor

FOREWORD

The technology program described herein was sponsored by the National Aeronautics and Space Administration, Lyndon B. Johnson Space Center, Houston, Texas, under Contract NAS9-12077. The study was conducted during the 21-month period from 1 July 1971 to 31 March 1973. The NASA technical monitor was Mr. W. L. Brasher and, subsequently, Mr. R. C. Kahl. At Rocketdyne, Mr. L. P. Combs was program manager and Dr. C. L. Oberg was project engineer. Dr. Oberg was assisted by Mr. W. S. Hines and Mr. L. Kusak.

This report has been assigned Rocketdyne Report Number R-9136. A Separate summary report has also been prepared (R-9206).

ABSTRACT

A series of rocket motor firings was performed in a modified linear aerospike thrust chamber with the H_2/O_2 propellant combination to allow determination of the physical properties of the combustion gases in acoustic cavities located in the chamber side walls. A preliminary analytical study was first conducted to define theoretically both the appropriate cavity dimensions and the combustion gas flow field adjacent to the cavity openings. During the subsequent motor firings, cavity gas temperature profiles were measured and gas samples were withdrawn from the bottom of the cavities for compositional analysis by measurement of pressure/temperature variation and gas chromatography. Data were obtained with both "radially" and "axially" oriented cavities and with and without hydrogen bleed flow through the cavities. The resultant experimental data were then combined with the theoretical results to develop a simplified procedure for predicting gas cavity and acoustic velocity for use in acoustic cavity design analyses.

The motor firings were made at a nominal mixture ratio of 6.0 and over a chamber pressure range of 486 to 1107 psia. Measured cavity gas temperatures ranged from 70 to 1510 F, depending on cavity configuration, bleed rate, and location within the cavity. The cavity gas was composed of 93 to 100 mole percent hydrogen with the remainder being essentially all water vapor with traces of atmospheric contaminants.

CONTENTS

ILLUSTRATIONS

TABLES

INTRODUCTION

Recently, considerable attention has been directed toward rocket engines that are operated at high chamber pressures and with the hydrogen/oxygen propellant combination, e.g., the Space Shuttle Main Engine. Undoubtedly, some method of preventing combustion instability will be required in such engines. One of the most attractive ways of obtaining this stability is the use of acoustic cavities or absorbers to damp acoustic modes of combustion instability.

Absorbers may comprise acoustic resonators distributed in some manner along the interior walls of a thrust chamber. One such arrangement, which is particularly attractive from a design and manufacturing standpoint, is a single row of acoustic resonators along the periphery of the injector. The term "acoustic cavity" has been loosely used to describe this simple arrangement of resonators, generally quarter-wave resonators. These cavities are simply narrow slots, either axially or radially directed, with uniform cross-sectional area. The slots are partitioned to prevent circumferential flow of hot gases. However, interest is not restricted to these simple slots. Any form of acoustic resonator should be useful, although some forms may be more effective than others.

Acoustic cavities may be used as the sole means of instability suppression or as a supplement to injector-mounted baffles. If used as a supplement to baffles, a less elaborate baffle configuration is required. This is important because baffles are difficult to cool at the high chamber pressures. Moreover, the use of baffles may be accompanied by problems with fabrication, durability, performance losses, and excess weight. Most of these problems do not occur with the use of cavities, although others, such as the spatial requirements for the cavities, do. Thus, the use of acoustic cavities or a suitable combination of baffles and cavities is likely to be the best means of preventing combustion instability in high chamber pressure H_2/O_2 engines.

Acoustic absorbers are generally designed through the use of analytical procedures that include a calculation of the oscillatory behavior of the resonator itself. This analysis requires a knowledge of the sound velocity and density of the gases contained in the cavity as well as the cavity dimensions. As this program began, little information pertaining to cavity sound velocity and density for high-pressure H_2/O_2 engines was available. Acoustic cavities have been applied with considerable success to engines employing storable propellants but not to H_2/O_2 engines. The available information was obtained almost exclusively from limited testing with acoustic liners (an array of Helmholtz resonators usually distributed over the entire chamber wall from the injector to the nozzle entrance). Therefore, this program was undertaken.

The purpose of the program described herein was to determine experimentally the sound velocity and density of the gases contained in the acoustic cavities of moderately high chamber pressure H_2/O_2 engines. These properties were to be determined over a sufficient range of operating conditions and cavity configurations to allow correlations to be developed that would be applicable to the entire range of interest (nominally, chamber pressures from 500 to 3000 psia and injection mixture ratios between 5.0 and 6.5).

To meet the objectives of the program within available funds it was deemed necessary to utilize an existing thrust chamber. Moreover, it was desired that an engine be selected that would be suitable for subsequent stability rating tests if so desired. A Rocketdyne linear aerospike segment thrust chamber (Ref. 1) was selected for several reasons including availability and operating pressure capability. This engine has a rectangular cross section that has the advantage to this program of a relatively low thrust and propellant consumption rate for a particular fundamental mode instability frequency, when compared with a cylindrical engine. A cylindrical engine with an equivalent instability frequency would have a thrust level of 80,000 lbf as compared with a 9000 lbf for the linear engine. A low instability frequency would be desirable for subsequent instability testing because, typically, stability is more difficult to achieve at low (acoustic) frequencies so that the test of cavity stabilization would be more stringent. In addition, the injector design of the linear aerospike was thought to be resentative of the state of the art.

The approach taken during this program was to install acoustic cavities in the selected aerospike thrust chamber and then measure, during motor firings, the temperature distribution within the acoustic cavities and withdraw gas samples from them for subsequent compositional analysis. The cavity sound velocity and gas density were calculated from the measured temperature and composition.

A number of difficulties encountered during the program led to diminished extent of testing and analysis from that originally planned. The principal difficulties were encountered in obtaining a suitable thrust chamber, which proved less available than anticipated when the aerospike segment was selected for testing, for use during the test program and then installing the cavities in the fragile structure of the regeneratively cooled engine. Nevertheless, a substantial number of tests were made and sufficient data were obtained to allow useful correlations to be developed for the cavity gas temperature and composition.

This report describes (1) analytical studies which are made to aid in selection of the cavity configurations to be tested, to predict the nature of the combustion flow field, and to predict stability variations with chamber pressure, (2) design and fabrication of the hardware used during the test program, (3) results from the test program, and (4) analysis and correlation of the results.

ANALYTICAL STUDIES

The effects of varying cavity dimensions and engine operating conditions on cavity damping, the combustion flow field (cavity environment), and engine stability were examined analytically. The primary purpose of these studies was to ensure that the experimental results from the motor firing program would be as completely applicable as possible to high chamber pressure H_2/O_2 engines of current interest, e.g., the Space Shuttle Main Engine. More specifically, analytical studies were done for the following reasons:

1. To aid selection of representative acoustic cavity configurations
2. To assess the effects of chamber pressure variations on the cavity environment (combustion flow field) and engine stability
3. To provide information on the cavity environment that could be used to rationally correlate measured variations in cavity conditions with engine operating conditions and cavity configurations

To meet these objectives, three kinds of analyses were used, all of which had been developed previously. An analytical model that predicts the damping contributed by an acoustic cavity array was used to predict the variation in cavity damping with changes in cavity configuration. Another analytical model that predicts the steady-state combustion flow field in an engine with concentric tube-type injection elements was used to calculate the flow field environment of the acoustic cavities. Finally, a Priem-type combustion instability model was used, employing results from the steady-state combustion model calculation, to predict engine stability.

SELECTION OF CAVITY CONFIGURATIONS TO BE TESTED

An analytical procedure has been developed to aid in the design of acoustic cavities (Ref. 2). With this procedure, the variation in damping produced by an acoustic cavity (independently of other gain or loss processes) is calculated with variations in cavity dimensions. Because there is presently no method for analytically estimating the amount of damping required to achieve stability, a cavity that is calculated to produce near-maximum damping is generally selected for use. This procedure was used to aid selection of the cavity configurations to be tested because it is the procedure that would normally be used to design cavities for a new application. This analytical procedure is outlined in Appendix A.

An analysis was made for a cylindrical engine with an instability frequency of the first tangential mode equal to that of the first transverse of the linear aerospike selected for testing. Thus, the linear aerospike was chosen as an experimental model of the corresponding cylindrical engine because cylindrical engines are currently of a greater interest to NASA. From a practical standpoint, this only affects the size and location of the individual cavities.

In a cylindrical engine, acoustic cavities are generally located along the periphery of the injector. The corresponding location in the linear aerospike is the

junction between the injector and the side walls of the chamber. Moreover, because of the welded construction of the linear aerospike with integral regenerative cooling passages, the only practical locations for acoustic cavities in this hardware were the straight end walls adjacent to the injector. The two types of cavity configurations chosen for this location are sketched below.

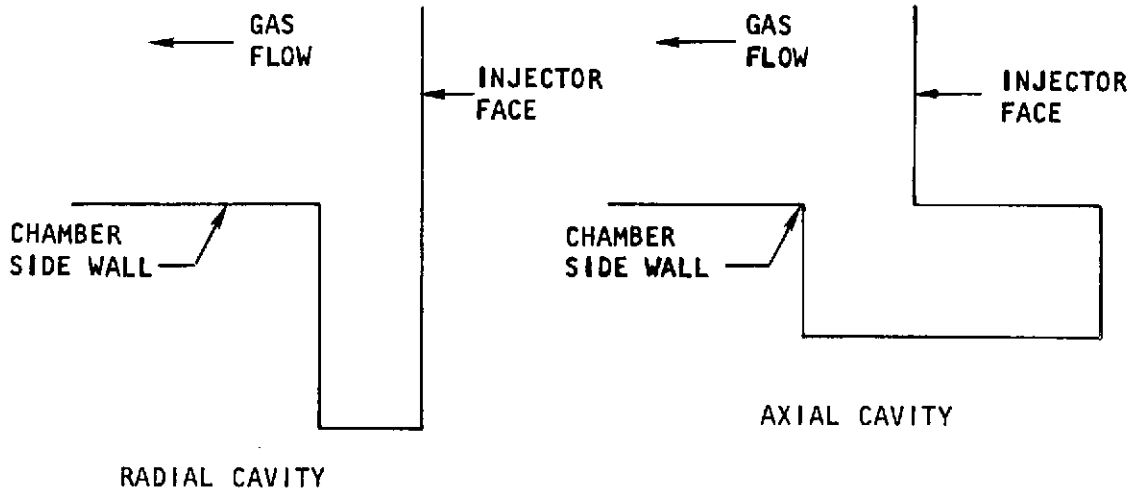

For a cylindrical engine, these configurations would be called "radial" and "L-shaped semiaxial." Therefore, for this program they have been termed simply "radial" and "axial" cavities. Both configurations were selected because one purpose of the program was to evaluate the effect of orientation on the cavity gas properties.

Cavity damping calculations were made for each of these configurations (cylindrical chamber) with cavity gas properties being estimated from the experimental data of Phillips (Ref. 3) which were obtained from tests with an acoustic liner. Average cavity gas temperature was assigned a value of 1125 R while the gas composition was assumed to consist of 90 mole percent hydrogen and 10 mole percent water vapor. The assumption of ideal gas behavior and a specific heat ratio of 1.37 then resulted in an estimated gas density of 0.304 lbm/ft^3 and sonic velocity of 4625 ft/sec at a chamber pressure of 1000 psia. Based upon stability results from tests with acoustic cavities in an unbaffled Lunar Module (LM) ascent-type engine (Ref. 4), a value of 0.15 was assigned to the amplitude parameter $\Gamma\hat{p}/\gamma p_o$.

The results from these calculations are shown in Fig. 1 and 2. Based upon these results, single cavity depths of 4.30 and 5.0 inches were chosen for the radial and L-shaped cavities respectively. The basic cavity width was chosen as 0.8 inch with provision for variation of the width to 0.4 or 0.6 inch by means of inserts in the cavity. These cavity dimensions were selected because they correspond to near maximum predicted damping and, therefore, are representative of dimensions that would be chosen for an application of cavities. It is of interest to observe that the predicted damping for the two basic configurations is similar in magnitude but maximum damping occurs at different physical depths. However, even if the depth of the L-shaped axial cavity is scaled to correspond to that of the radial cavity, assuming the "effective" depth of the axial cavity which gives maximum

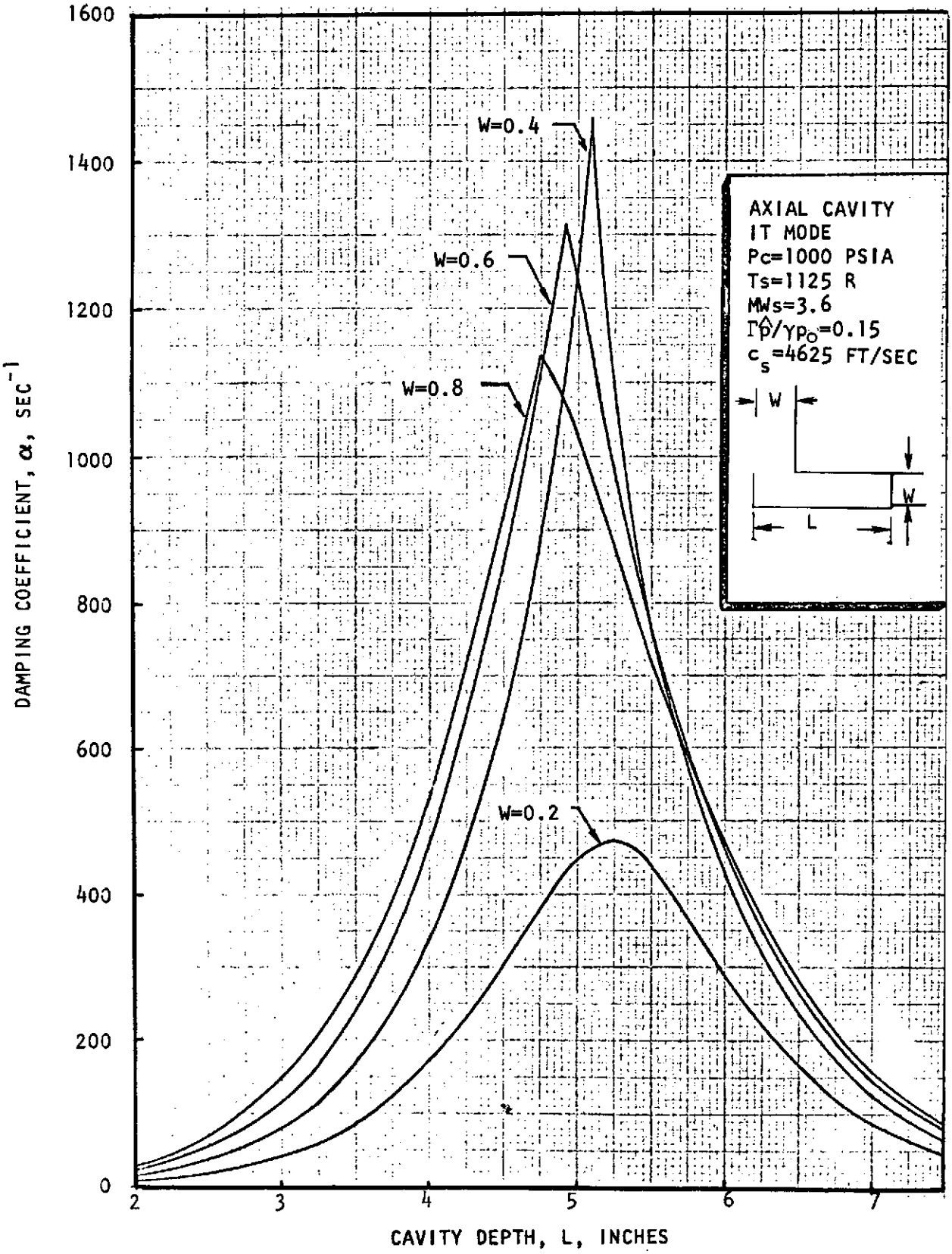

Figure 1. Predicted Cavity Damping With L-Shaped Axial Cavity

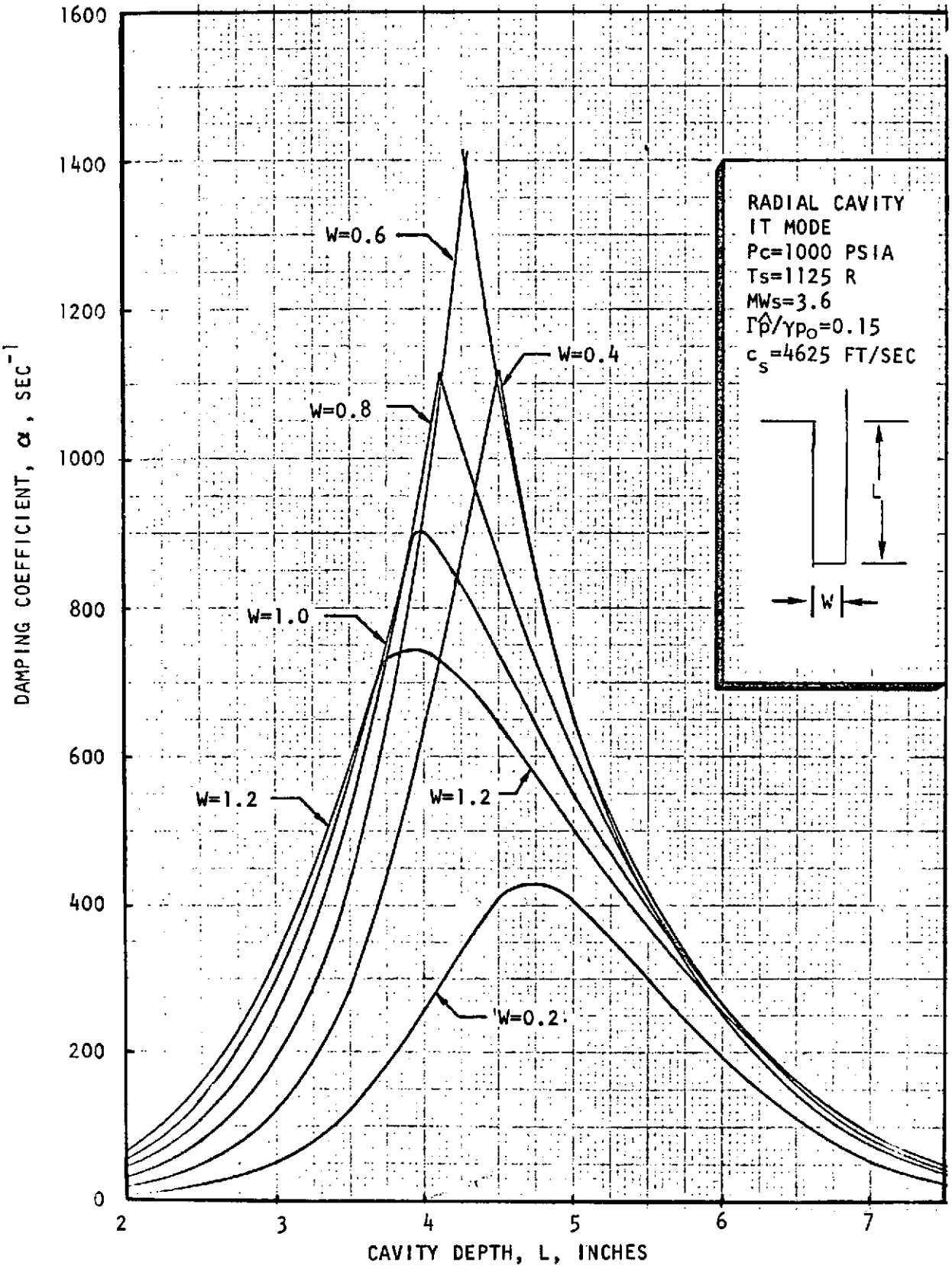

Figure 2. Predicted Cavity Damping With Radial Cavity

damping is the same as the physical depth of the radial cavity at maximum damping, the predicted damping is noticeably different. Nevertheless, the differences are not large enough to justify selecting one orientation over the other on this basis.

ANALYSIS OF COMBUSTION GAS FLOW FIELD

A quasi-one-dimensional computerized steady-state combustion model was used to predict the combustion flow field that existed in the engine and, thus, the environment for the acoustic cavities. This model, the CSS combustion model, is set up for the analysis of concentric tube injection elements and has been extensively used to analyze various H_2/O_2 engines. This model is briefly described in Appendix B and more thoroughly in Ref. 5. Three series of calculations were made with this model.

The objective of the first series was to determine the effects of a varying chamber pressure with a fixed hardware configuration, as would later be tested in the motor firing experiments. For this series of calculations, the injector configuration of the cast segment linear aerospike engine originally scheduled* for use in this program was analyzed for chamber pressures of 800, 1000, and 1200 psia and an injected mixture ratio of 6.0. In this injector, a LO_2 post recess of 0.15 inch was used. Such a recess promotes vaporization and mixing in the cup formed by the recess.

Results from a combustion model calculation for a chamber pressure of 1000 psia are shown in Fig. 3 with the calculated extent (fraction) of propellant combustion, gas mixture ratio, temperature, and axial velocity of the combustion gas for the initial 3.0 inches downstream of the injector being shown. The calculated variation of the extent of combustion over the initial 2.4 inches downstream of the injector at 800 and 1000 psia is shown in Fig. 4 . There is little variation in the calculated propellant burning rate over this pressure range. Because the axial dependence of mixture ratio, gas temperature, and velocity are all closely related to the variation in burning rate, the gas flow field described by Fig. 3 can be considered to be essentially independent of pressure over the range of 800 to 1200 psia. It is interesting to note that the extent of combustion curves shown in Fig. 4 cross each other about 1.7 inches downstream of the injector. This appears to result from a complex interaction of several processes in the model and cannot be explained simply.

During the second series of calculations, the propellant combustion flow field was calculated for chamber pressures of 500 to 3000 psia. However, during these calculations, the injector element configuration (particularly the dimensions of the annular hydrogen flow passage) was varied until maximum performance was obtained with a fixed gas velocity and constant ratio of injector pressure drop to chamber pressure. A recess of 0.15 inch for the LO_2 post was chosen in both cases. For the optimized injector configurations, the calculated variations of fraction LO_2 burned and gas mixture ratio, temperature, and velocity with distance from the injector at these two extreme chamber pressures are compared in Fig. 5 through 8

*Another aerospike segment engine was actually made available and used.

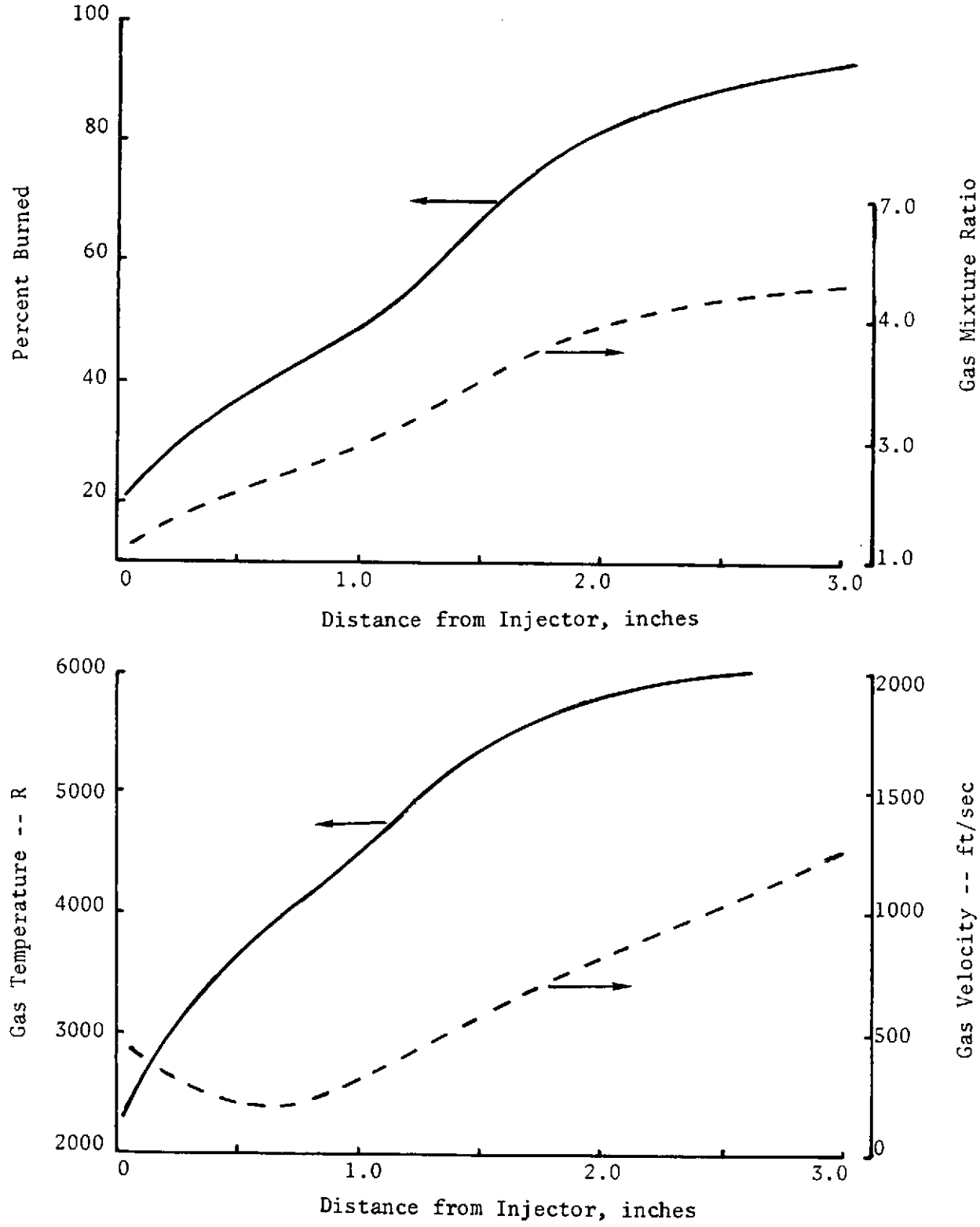

Figure 3. Predicted Variation of Combustion Gas Parameters With Distance From Injector for a Chamber Pressure of 1000 psia (0.15-Inch LO_2 Post Recess)

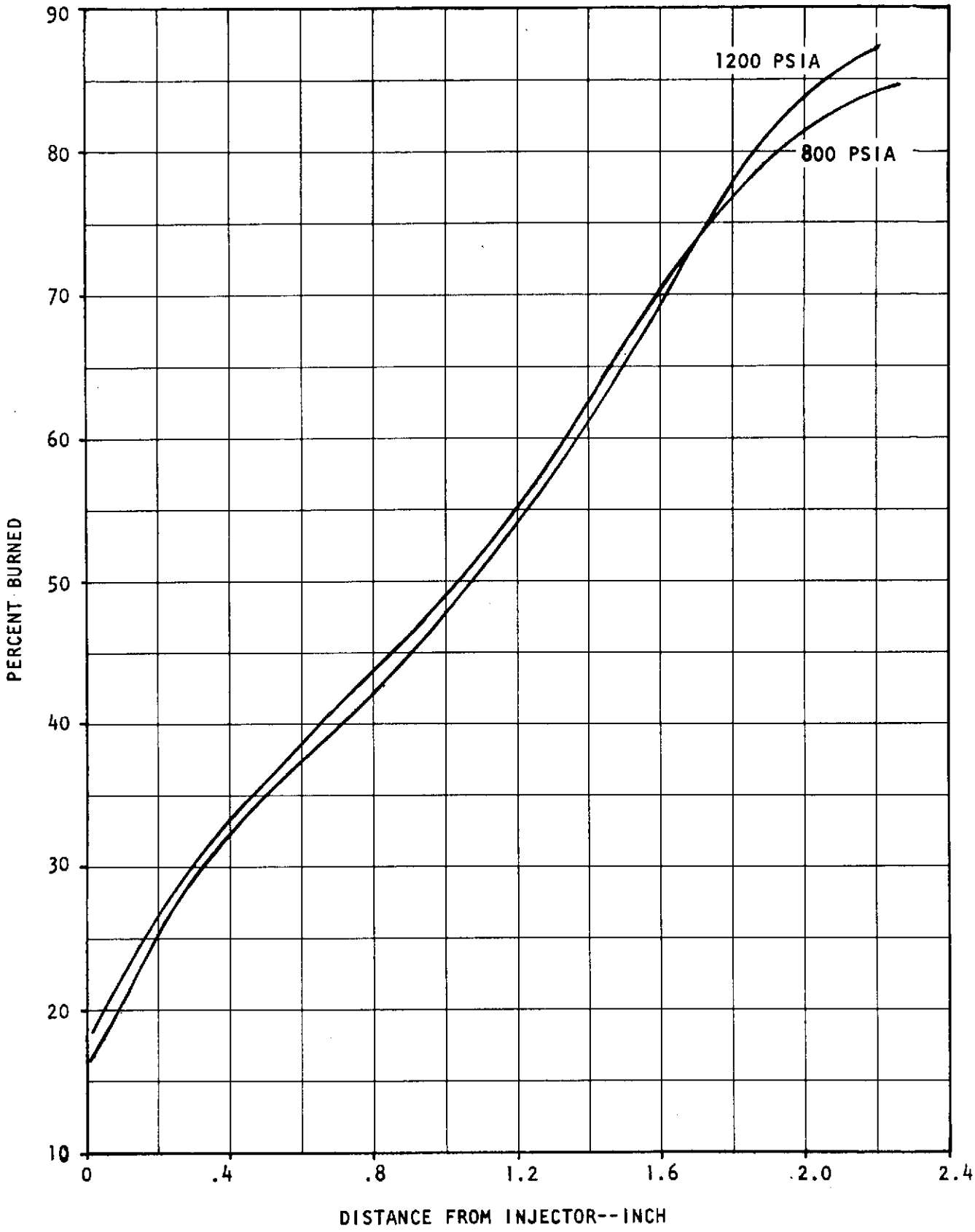

Figure 4. Comparison of Predicted Near Injector Burning Rates at Chamber Pressures of 800 and 1200 psia (0.15-Inch LO_2 Post Recess)

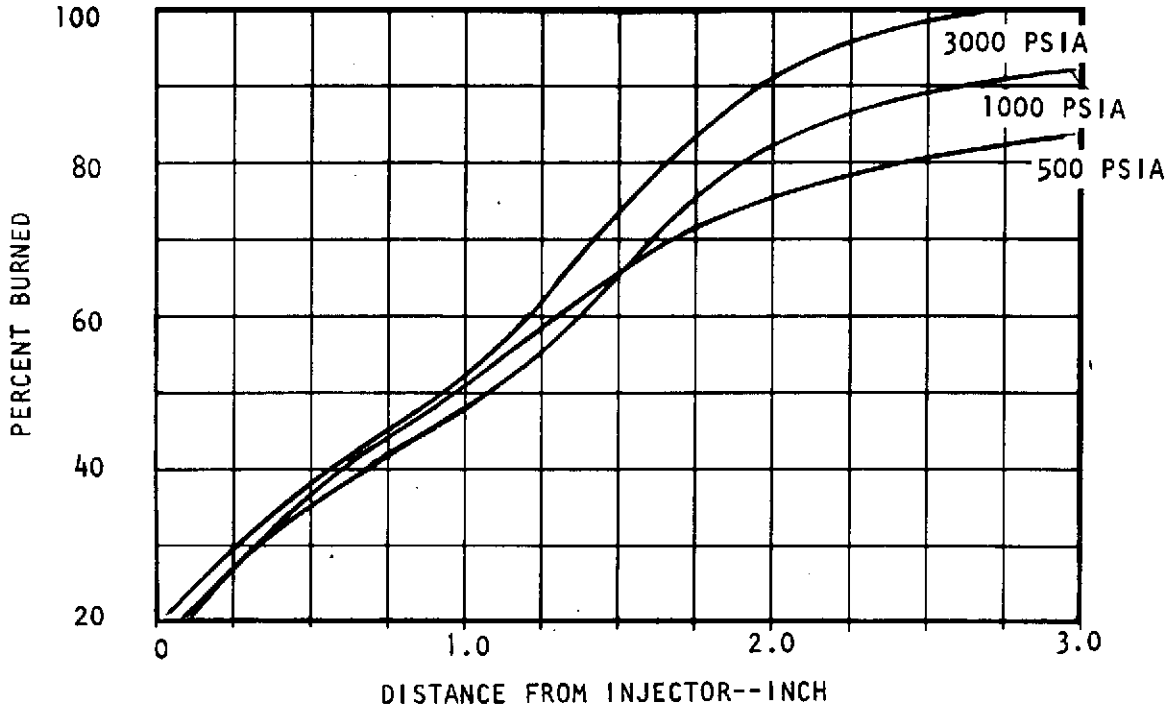

Figure 5. Predicted Variation of Percent Combustion With Distance From Injector (0.15-Inch LO_2 Post Recess)

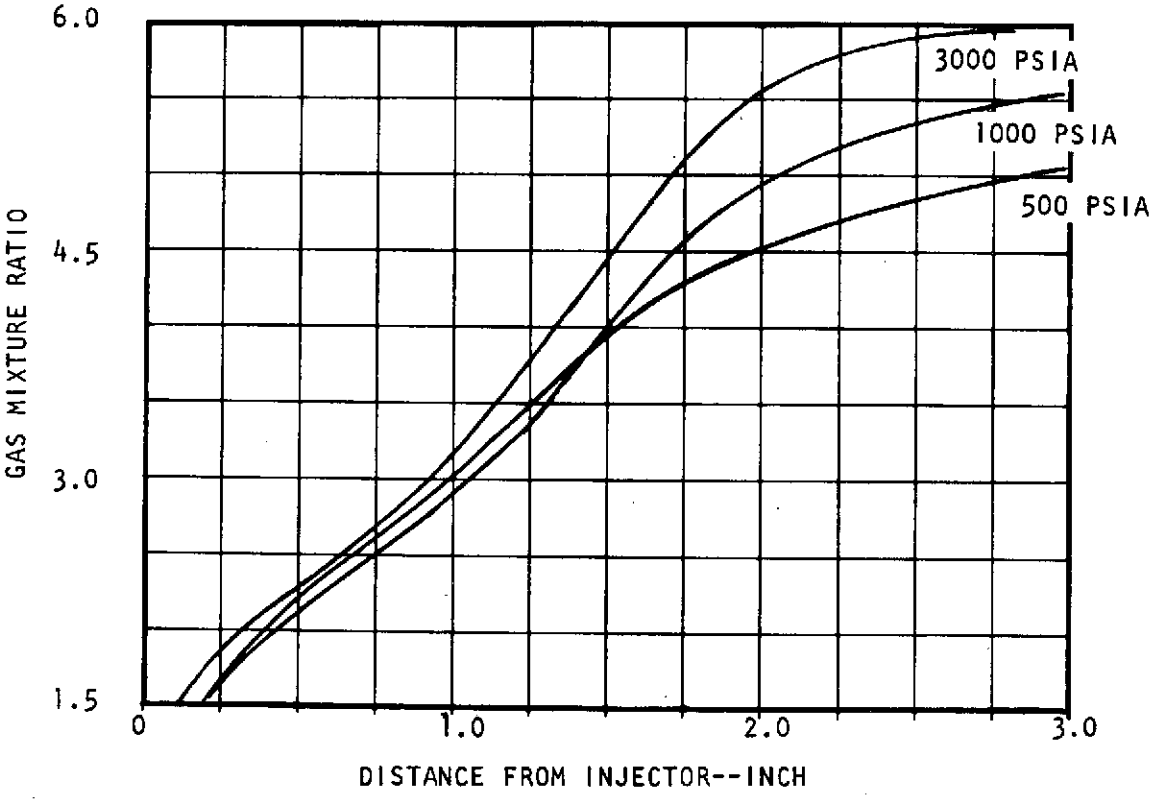

Figure 6. Predicted Variation of Mixture Ratio With Distance From Injector (0.15-Inch LO_2 Post Recess)

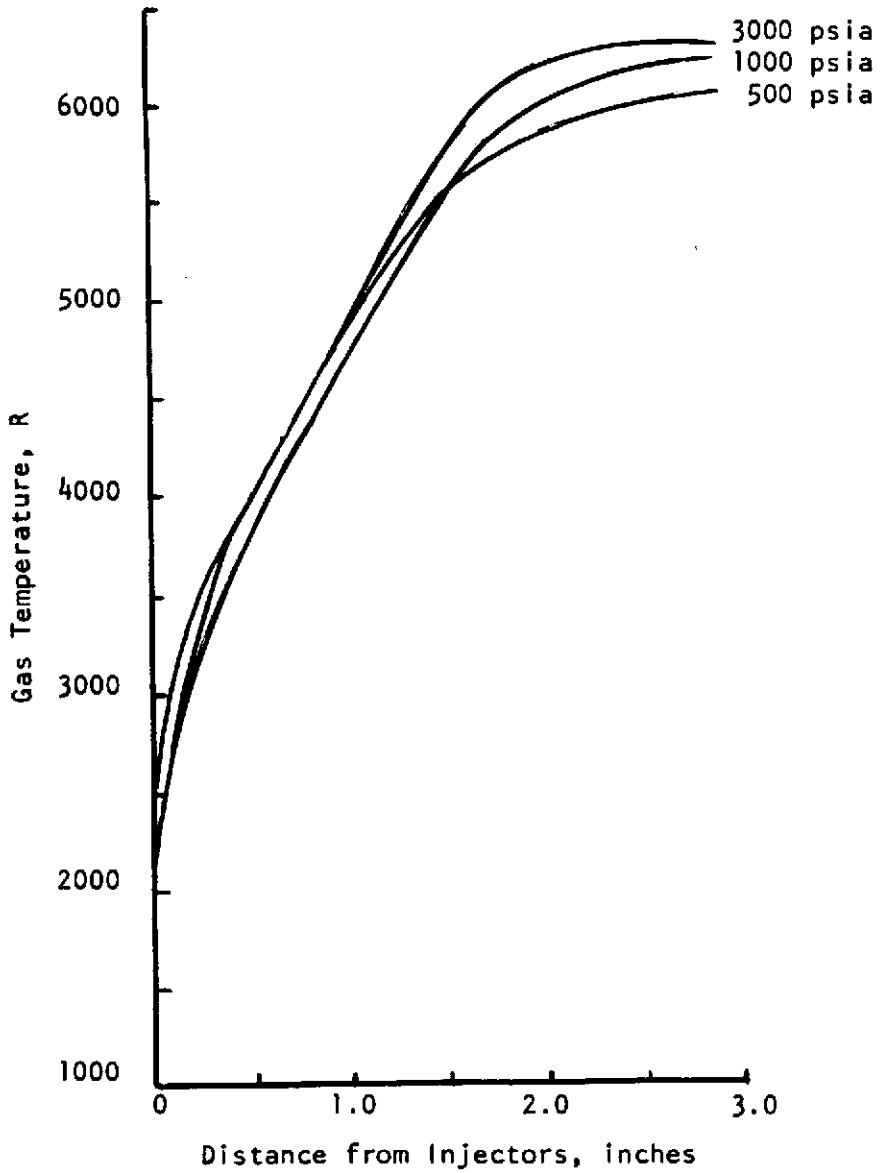

Figure 7. Predicted Variation of Gas Temperature With Distance From Injector (0.15-Inch LO_2 Post Recess)

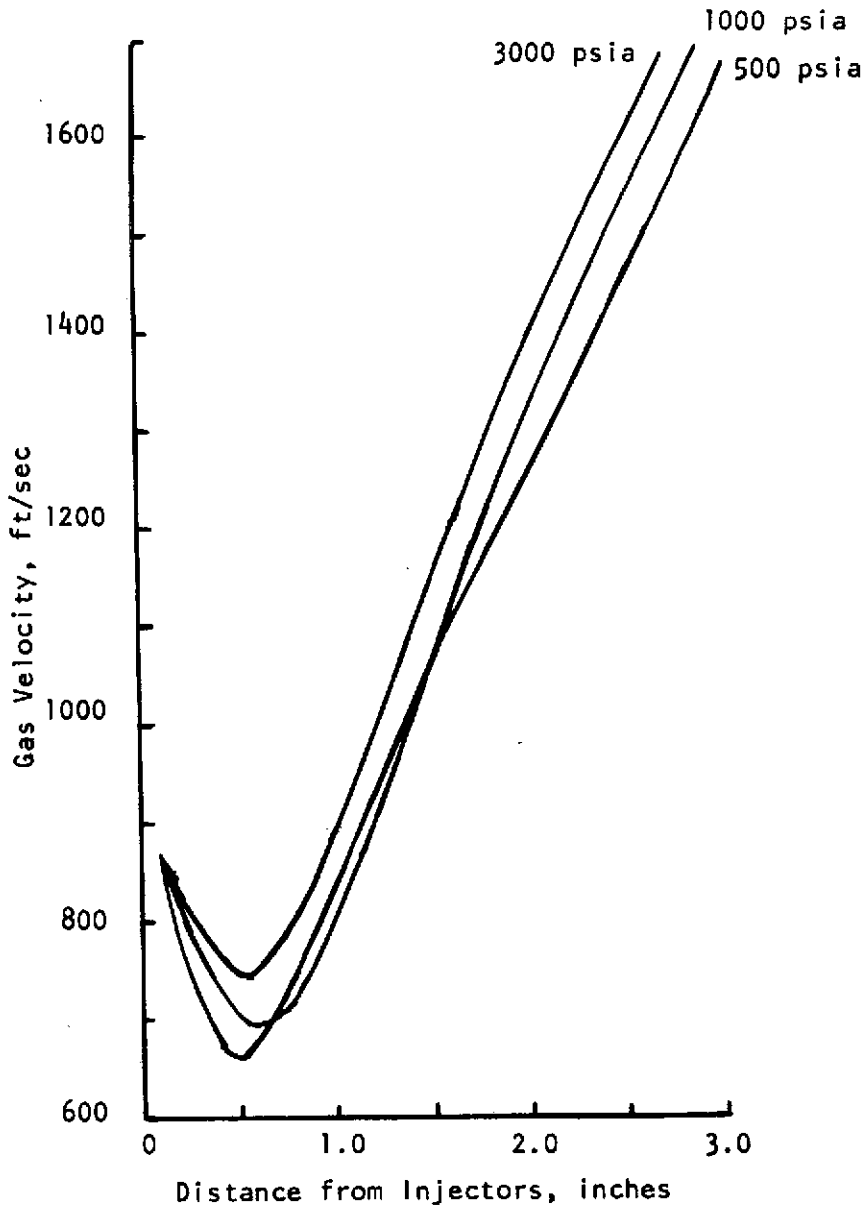

Figure 8. Predicted Variation of Axial Gas Velocity With Distance From Injector (0.15-Inch LO_2 Post Recess)

with the results from the 1000-psia case. The results shown in Fig. 5 indicate that the burning rate over about the first inch of the chamber is essentially independent of pressure, but becomes more rapid with increasing pressure at greater distances from the injector. The curves shown in Fig. 5 cross as they did in Fig. 4, as a result of the same type of complex interaction.

During the third series of calculations, the combustion flow field was calculated for chamber pressures of 800 and 1000 psia and an injector configuration with no LO_2 post recess. This configuration corresponded to the actual thrust chamber assembly employed in the motor firings. In Fig. 9 are shown the calculated variations with longitudinal position of the fraction burned, gas mixture ratio, temperature, and gas velocity over the initial 3.0 inches with the nonrecessed LO_2 post and at 1000-psia chamber pressure. The gas flow field parameters calculated at a chamber pressure of 800 psia for the case of no LO_2 post recess were essentially the same as those shown in Fig. 9.

The difference in LO_2 post recess between zero and 0.15 inch caused very significant differences between the near-injector burning rates and flow fields. Figure 10 shows the variation in the percent burned for the two geometries at a chamber pressure of 1000 psia; Fig. 11 shows a similar comparison for the resultant gas mixture ratio and temperature. It is clear from the graphs that lower mixture ratios and temperatures are predicted in the gas flow field adjacent to the acoustic cavities if no LO_2 post recess is used in the injector.

Probably of particular significance to the cavity behavior are the size and nature of the recirculation region close to the injector. In the calculation, this region occurs where the main flow field does not fill the complete cross-sectional area of the combustion chamber. The extent of this zone for the injector with no LO_2 post recess is shown in Fig. 12, where the fraction of unfilled chamber area is plotted as a function of distance from the injector face. This figure shows that the flow attaches at approximately 0.60 to 0.65 inch from the injector. The temperature and composition of the gas at the entrance to a cavity which does not extend beyond the attachment distance is presumably defined by conditions at some point intermediate between the conditions at the attachment point and the mean distance of the cavity opening from the injector.

STABILITY ANALYSIS

The manner in which the acoustic cavity requirements for stable operation will change with variations in engine operating pressure cannot be predicted at present. However, the amount of cavity damping required will vary as the degree of instability varies which can be predicted through the use of an analytical model for the instability processes. Therefore, a Priem-type combustion instability model was used to predict the variation of engine stability with chamber pressure using the steady-state model results for these calculations. The Priem model calculations are outlined in Appendix C. From this model, a stability index, A_p, is obtained as a function of axial position in the chamber. A_p is a measure of the degree of stability of an engine; higher values correspond to greater stability.

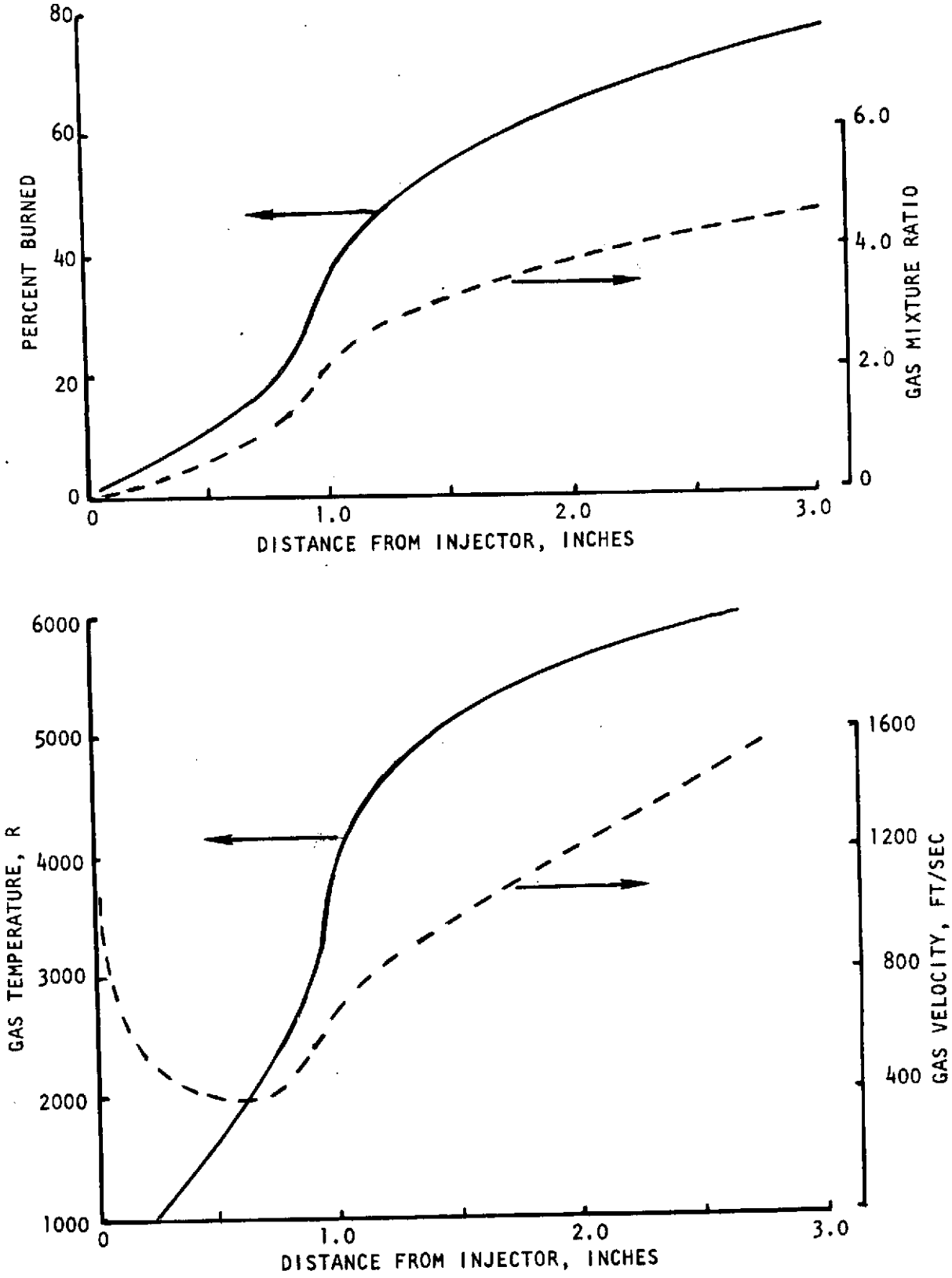

Figure 9. Predicted Variation of Combustion Gas Parameters With Distance From Injector at 1000 psia and a Mixture Ratio of 6.0 (No LO_2 Post Recess)

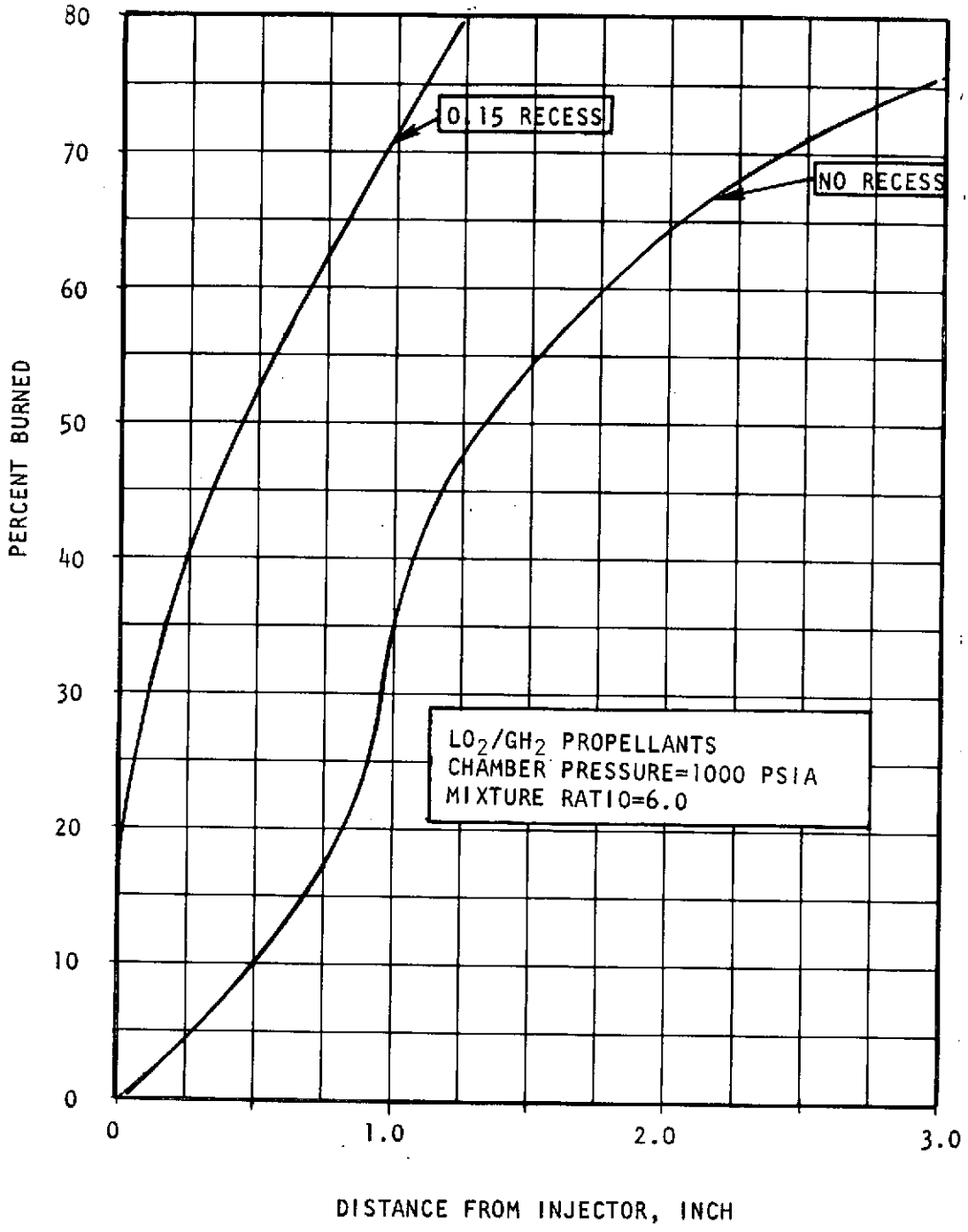

Figure 10. Effect of Post Recess Upon the Degree of Propellant Vaporization Near the Injector for Coaxial Element Injector

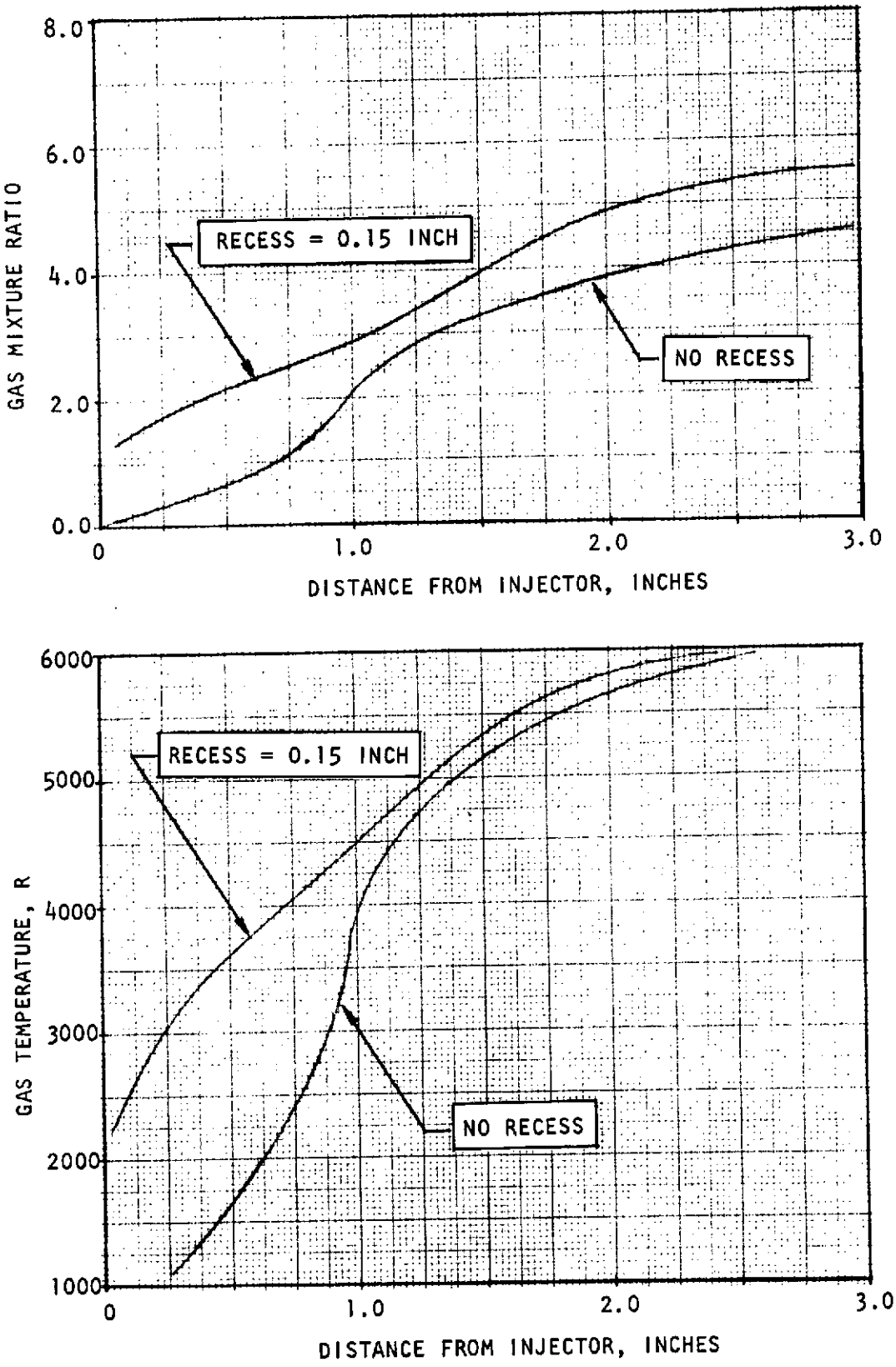

Figure 11. Comparison of Predicted Gas Mixture Ratio and Temperature Between Injectors With No LO_2 Post Recess and a Recess of 0.15 Inch

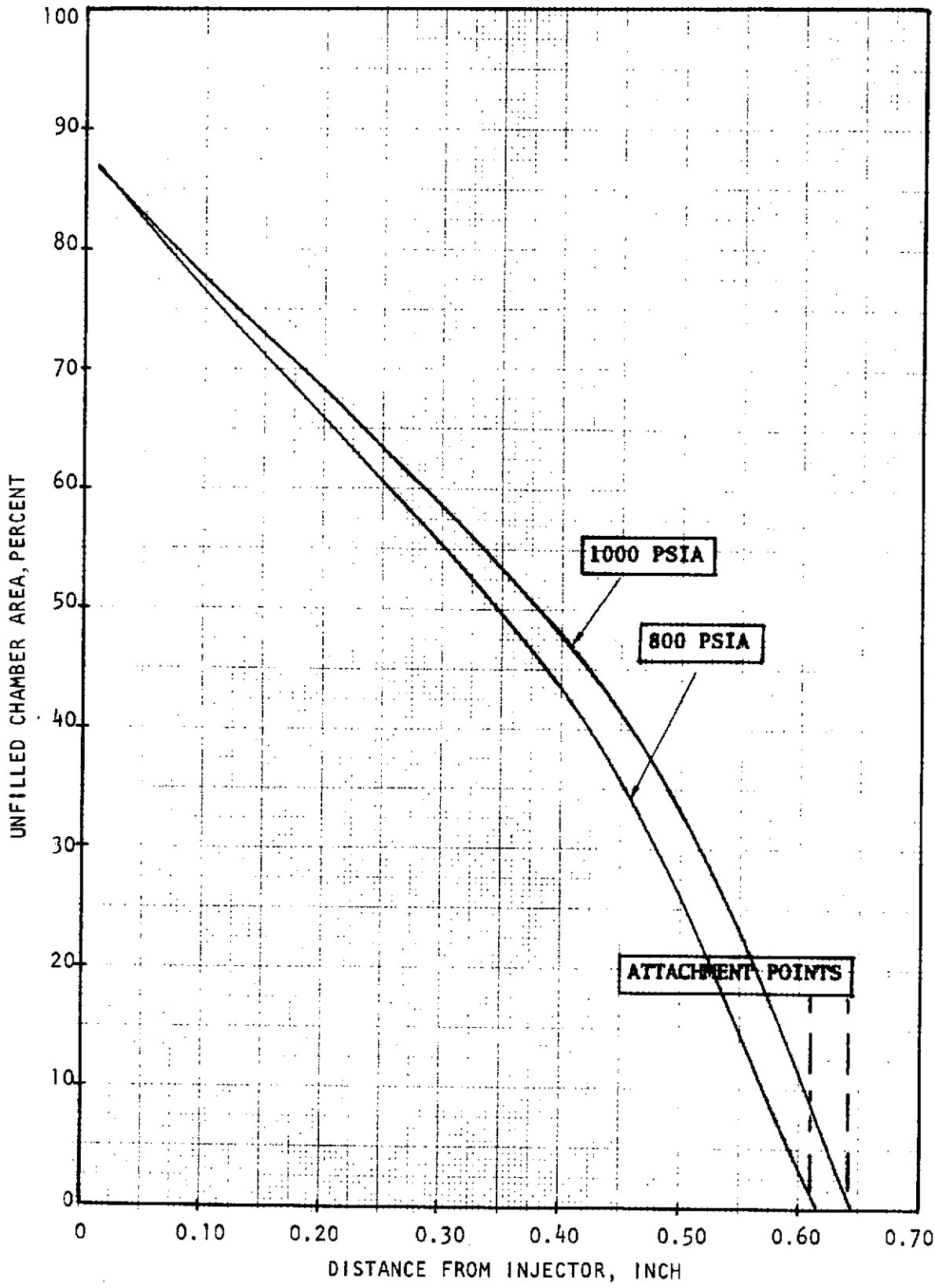

Figure 12. Variation With Distance From the Injector of Chamber Area Fraction Not Filled by the Main Combustion Gas Flow at 800 and 1000 psia for Coaxial Injector Without Post Recess

Calculated results for the cylindrical equivalent of the linear aerospike engine (13.2 inches in diameter) are shown in Fig. 13 and 14. The calculated values of A_p for chamber pressures of 800 and 1200 psia (originally planned pressures for the motor firing program) are shown in Fig. 13, while the values of A_p for the 500-, 1000-, and 3000-psia chamber pressures are shown in Fig. 14. The minimum values of A_p (most unstable point or most sensitive zone) and their locations for each chamber pressure are listed in Table 1.

TABLE 1. LOCATION AND VALUE OF STABILITY INDEX AT THE MOST SENSITIVE ZONE WITH 0.15-INCH LO_2 POST RECESS

Chamber Pressure, psia	Distance From Injector, inch	A_p
500	0.50	1.30
800	2.25	0.625
1000	2.25	0.33
1200	2.25	0.21
3000	2.25	0.092

Except for the 500-psia chamber pressure case (below the critical pressure of liquid oxygen), the most sensitive location is calculated to be a short distance downstream of the point of final disintegration of the liquid oxygen jet into discrete droplets. A clear trend of decreasing stability with pressure is indicated from the values of A_p listed above, which implies more stringent cavity damping requirements.

The foregoing analytical indication of decreasing stability with increasing chamber pressure is recognized as being inconsistent with the general experience of H_2/O_2 engine developments, wherein stability has usually not changed markedly (and sometimes has improved) with increased chamber pressure. A partial explanation for the anomolous results may lie in the assumption of constant hydrogen injection temperature in analyzing the linear aerospike, whereas higher P_c usually entails higher injection temperatures for the regenerative coolant propellant. Another partial explanation may be that the CSS computer model was used at an intermediate state of its continuing development and may have overpredicted the response of LO_2 spray combustion to pressure changes. By the time the model had evolved further, program funding limitations did not permit undertaking further analytical work, so these and other possibilities remain unresolved. The salient point remains, however, that selection of the degree of cavity damping provided must be related to the expected inherent stability at the engine operating conditions. At present, reliance must be placed on whatever relative stability comparisons are available or can be developed.

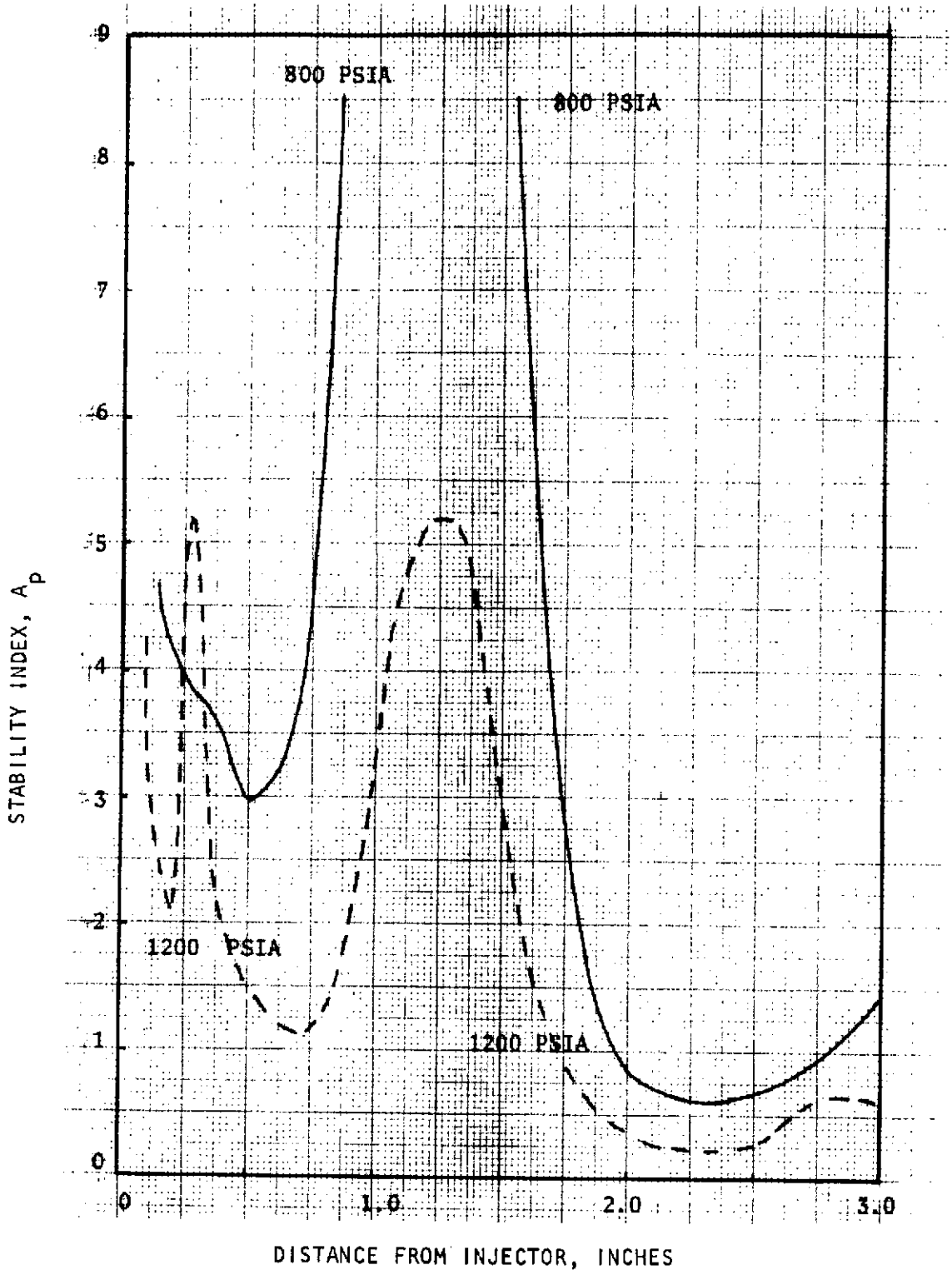

Figure 13. Variation of A_p With Distance From Injector for Chamber Pressures of 800 and 1200 psia With 0.15-Inch LO_2 Post Recess

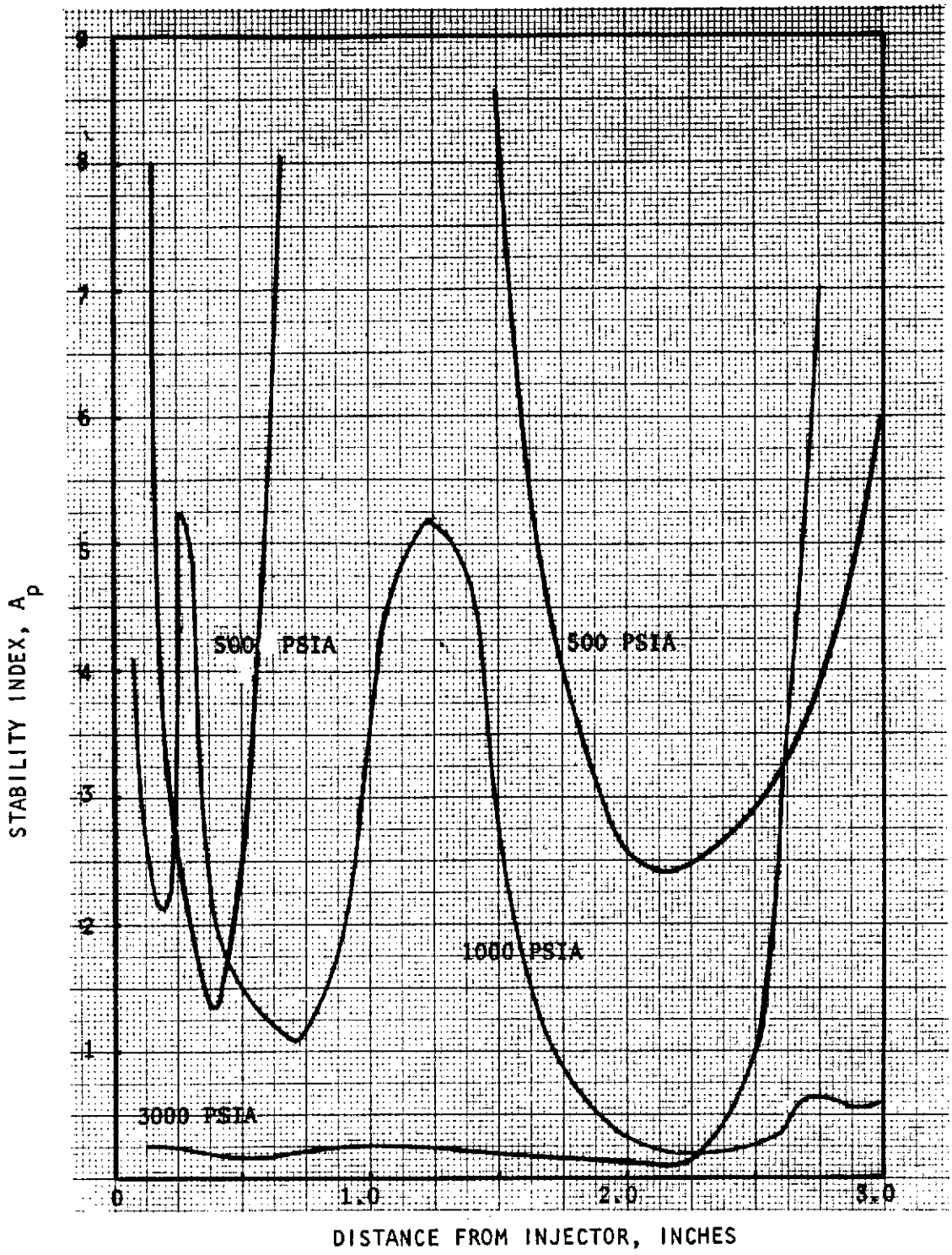

Figure 14. Variation of A_p With Distance From Injector for Chamber Pressure of 500, 1000, and 3000 psia With 0.15-Inch LO_2 Post Recess

EXPERIMENTAL STUDIES

The objective of the experimental effort was to determine the sound velocity and density of the gases contained in the acoustic cavities of moderately high chamber pressure H_2/O_2 engines. These properties were to be determined over a sufficient range of operating conditions and cavity configurations to allow correlations to be developed that would be applicable to the entire range of interest. However, a number of difficulties encountered during the program led to diminished amounts of testing and analysis from that originally planned. Nevertheless, a substantial number of tests were made and sufficient data were obtained to allow useful correlations to be developed for the cavity gas temperature and composition.

The approach taken during this program was to install acoustic cavities in a linear aerospike segment thrust chamber and then, during motor firings, measure the temperature distribution within the acoustic cavities and withdraw gas samples from them for subsequent compositional analysis. The cavity sound velocities and gas densities could then be calculated from the measured temperatures and compositions.

In addition to evaluating the effects of varying normal engine operating conditions, the effect of purging the cavity with a hydrogen injected from the closed end of the cavity was studied. The purpose of this hydrogen bleed is to control the gas sound velocity and density in the cavity at known levels. However, to achieve this purpose, the bleed flowrate and injection conditions necessary to control the conditions in the cavity must be determined. Therefore, tests were made to indicate these requirements.

During the test program, chamber pressure was varied over a nominal range of 500 to 900 psia with a single radial cavity width of 0.59 inch and over a nominal range of 850 to 1100 psia with two axial cavity configurations with widths of 0.59 and 0.42 inch. The effect of hydrogen bleed into the cavities was investigated at nominal flowrates of 0.007 and 0.025 lbm/sec/cavity with the radial cavity and for a single flowrate of 0.007 lbm/sec/cavity with the two axial cavities. Gas samples were withdrawn from the bottom of the cavities during a number of motor firings and later analyzed by a combination of pressure/temperature measurements (to determine the amounts at water and noncondensibles) and gas chromatography (to analyze the noncondensibles). A description of the hardware used in the tests, the results of the motor firings, and a correlation of these results are presented in the following paragraphs.

HARDWARE

Thrust Chamber

The engine configuration used for the motor firing tests was obtained by modifying a linear aerospike thrust chamber (identified by the number RL001562X). The basic features of the unmodified thrust chamber are shown schematically in Fig. 15. The chamber has a rectangular cross section that has a constant width of 11.585 inches and a height that tapers uniformly from 1.48 inches at the injector face to 0.458 inches at the throat 4.88 inches from the injector face. The nominal throat area is 5.31 sq in. in the unstressed conditions, but it expands to an area of 5.58 sq in. at a chamber pressure of 1000 psia, primarily because the long wall of the rectangular cross section behaves as a uniformly loaded beam.

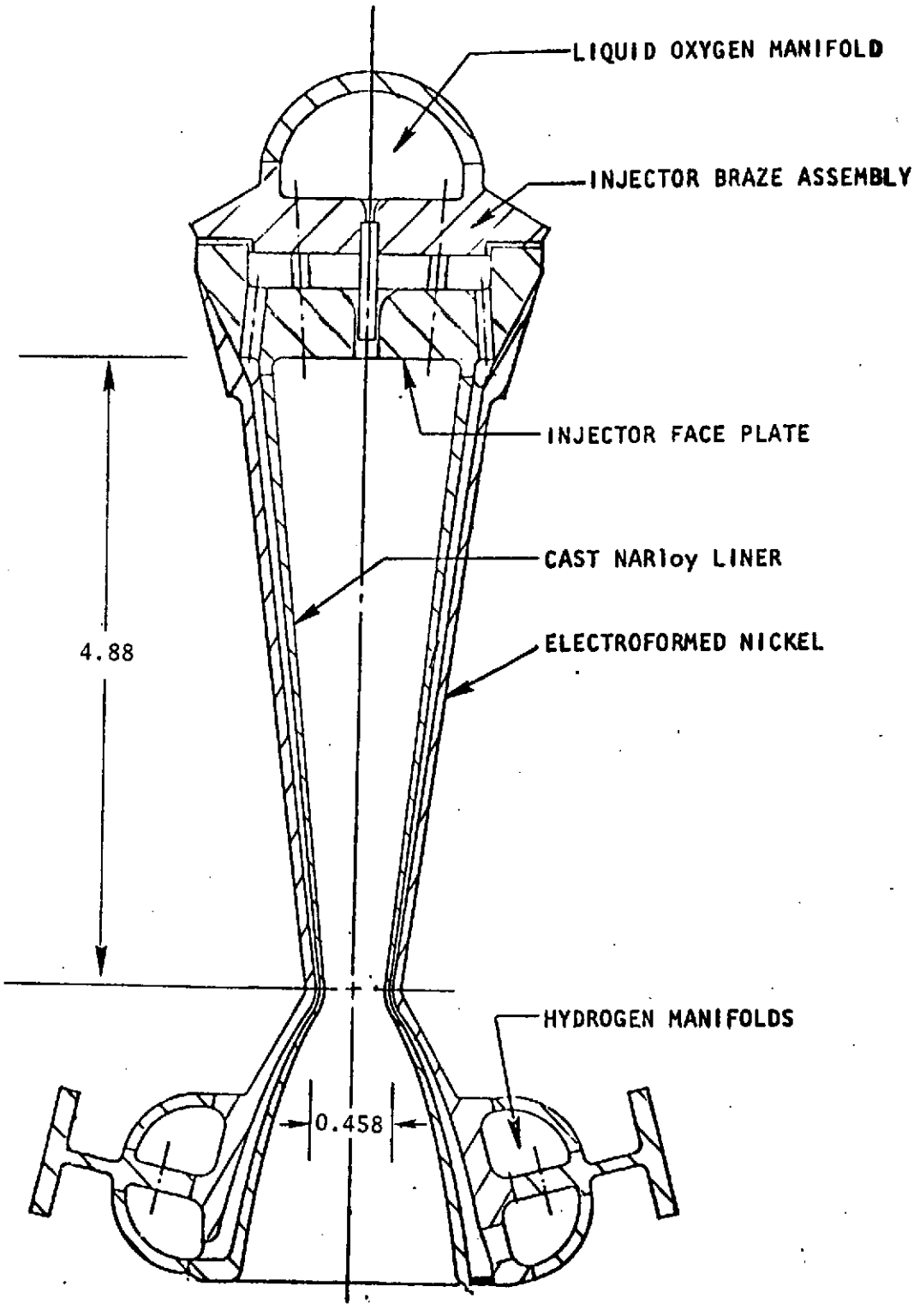

Figure 15. Schematic Representation of Cast Segment Linear Aerospike Thrust Chamber

The chamber walls are made of NARloy (copper alloy) and are cooled by gaseous hydrogen flowing through passages produced by electroforming a nickel outer wall over slots machined into the outside of the NARloy inner wall structure. The hydrogen is introduced into the coolant passages from a manifold at the exit end of the nozzle and flows toward the injector in a single-pass system. The hydrogen that cools the contoured walls then flows into the injector while the hydrogen that cools the straight side walls is used to cool the periphery of the acoustic cavity openings and is then dumped overboard through orifices on each side.

Injector

The injector, which is welded to the chamber body, consists of 67 coaxial gas/liquid H_2/O_2 elements arranged in three parallel rows and an H_2/F_2 igniter element. The outside diameter of each of the annular gaseous hydrogen fuel passages is 0.189 inch, while the inside diameter (i.e., the LO_2 post outside diameter) is 0.134 inch. The inside diameters of the LO_2 posts are each 0.106 inch. Tubular inserts were used in the LO_2 posts to increase the pressure drop and were 0.084-inch inside diameter and 0.78-inch long. The total oxidizer orifice length was 0.92 inch. The injector was designed originally to have a propellant mixing cup formed by an 0.16-inch recess of the LO_2 post tips from the injector face. However, previous to this program the effect of this cup was effectively eliminated by a flaring of the fuel annulus outside diameter to approximately twice its original dimension with a corresponding fivefold decrease in relative velocity between the concentric propellant streams at the injector face.

Acoustic Cavities

Acoustic cavities were fabricated in the chamber side walls immediately downstream of the injector face. Because the engine was being used as a two-dimensional experimental model of a cylindrical engine (corresponding to a diametrical section of the cylindrical engine) this cavity location corresponds to the conventional location of the cavities along the periphery of the injector. Moreover, this is the only location where the cooled chamber walls could be pierced practicably to install the cavities. The cavities were formed by welding and TIG brazing a multipurpose Nickel 200 housing (shown schematically in Fig. 16) to the chamber. The modified thrust chamber is shown in Fig. 17. The basic cavity housing configuration permitted the investigation of either radial cavities with a maximum depth of 4.30 inches and a maximum width of 0.80 inch, or the study of semiaxial cavities with a maximum depth of 5.0 inches and a maximum width of 0.80 inch. The cavity height was 1.30 inches in all cases. The cavity dimensions to be tested were selected from the damping calculations described in the Analytical Studies section.

The various radially or axially directed cavity configurations and the cavity widths were obtained through use of TZM molybdenum alloy filler blocks inserted through flanged openings at the bottom of the cavities (Fig. 16). These filler blocks, which were held in place by shoulders that slide into keyway slots in the housing walls, permitted either a complete closure of the cavity or a reduction in cavity width to 0.59 or 0.42 inch. The acoustic cavity body was cooled to a

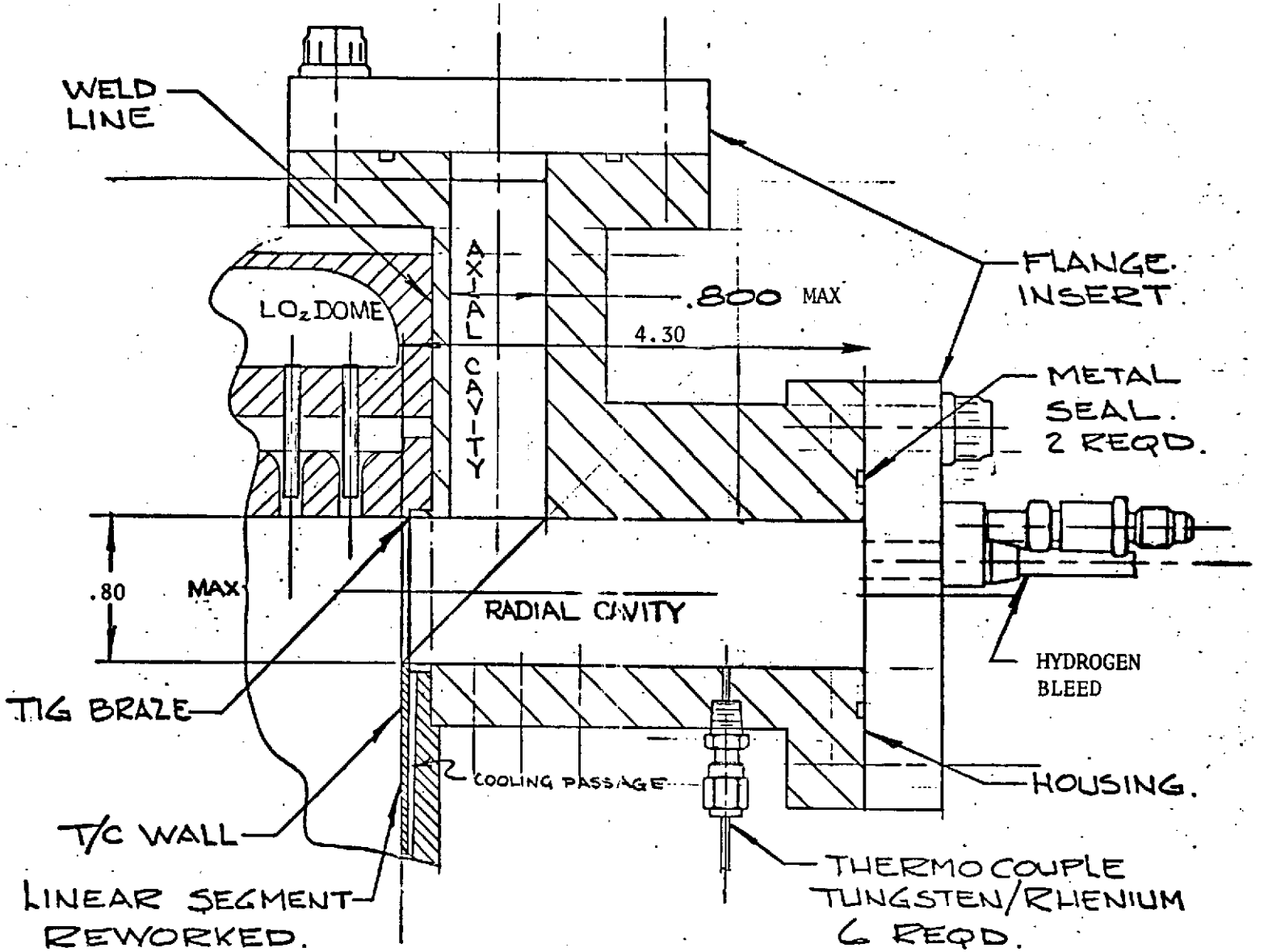

Figure 16. Schematic Representation of Acoustic Cavity Assembly

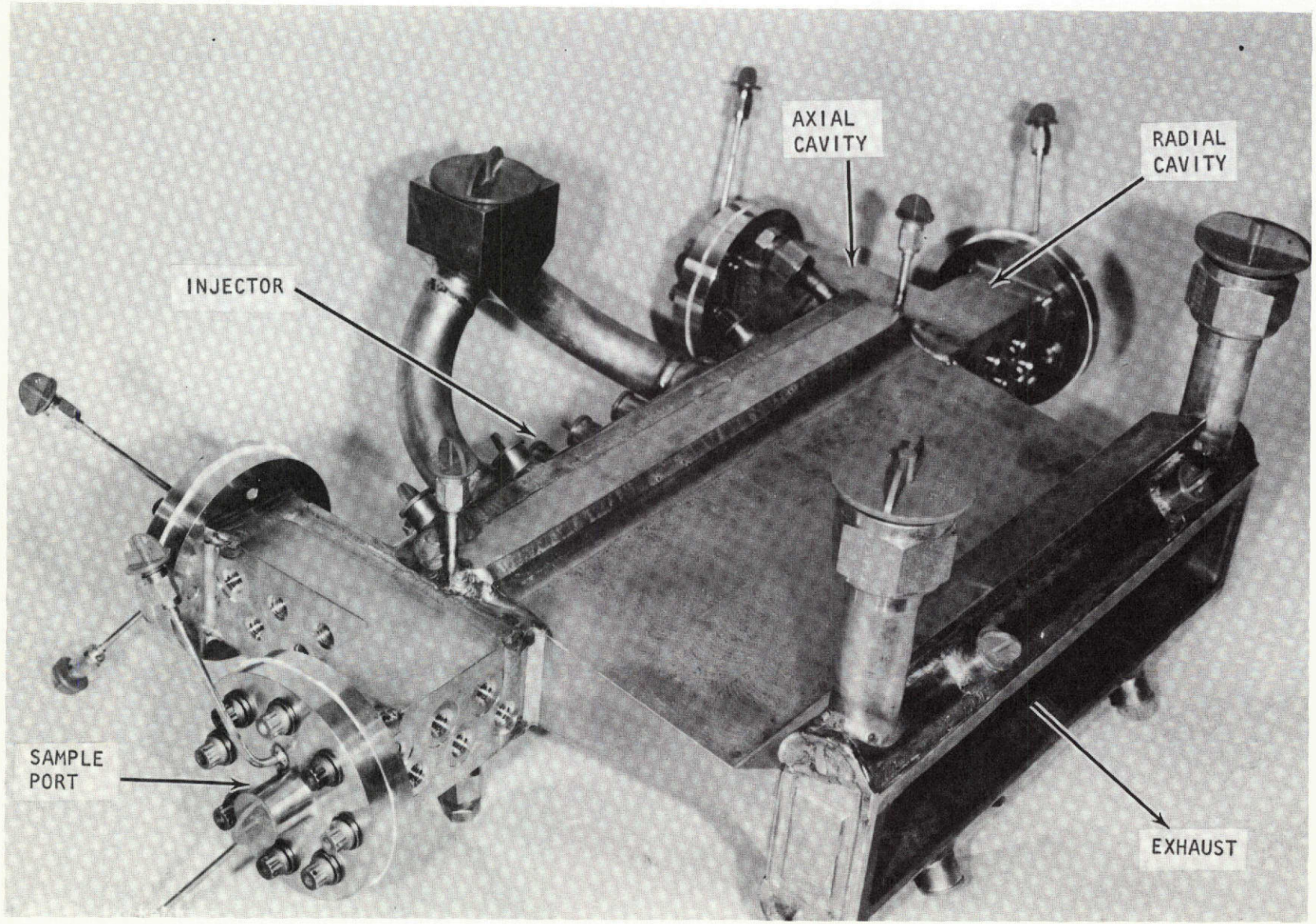

5AA-34-8/21/72-S1A

Figure 17. Linear Aerospike Thrust Chamber Modified for Acoustic Cavity Studies

depth of approximately 0.6 inch from the open end of the cavity by hydrogen flowing from the combustion chamber side walls through passages drilled in the nickel cavity walls. Additional cooling was provided around the cavity lip by hydrogen flowing in another passage beneath the copper-nickel braze joint.

The cavities were each instrumented with six exposed junction thermocouples (tungsten-5 percent rhenium/tungsten-26 percent rhenium). The thermocouples were inserted through the cavity walls and sealed by means of CONAX-type packing glands with crushable ceramic bushings.

Three ports were located at the closed end of each cavity, two for introducing a gas bleed and the third for withdrawing cavity gas samples. A 0.020-inch orifice used in the sampling port was selected to permit a 70-milliliter sample bottle to be pressurized to 100 psia with the sample gas over a period of approximately 300 milliseconds at a combustion chamber pressure of 1000 psia. The sampling time was selected in turn by the desire to limit the combustion gas velocity in the cavities to less than 2 ft/sec, a level which would cause the cavity gas to be displaced ~1.4 times during the sampling period and, therefore, was not expected to markedly change the gas composition or the temperature distribution within the cavities. However, flow through the sample line was vented to the atmosphere when not being collected in the sample bottle.

Backup Structure

Because of its rectangular cross section, the linear aerospike chamber requires reinforcement by a strong backup structure, particularly in the nozzle region where a close tolerance must be maintained on the throat gap. The outward forces from high chamber pressures were balanced by a system in which fitted spacer blocks transferred the beam loading from the chamber walls to the bolted-together aluminum alloy backup plates shown in Fig. 18 and 19.

TEST STAND

The motor firings were made on Nan Stand of the Rocketdyne Propulsion Research Area. A schematic diagram of this test facility is shown in Fig. 20. Gaseous hydrogen, with temperatures adjustable over a wide range, and liquid oxygen are available on this test stand. The hydrogen temperature is controlled by mixing liquid and ambient temperature gaseous hydrogen. Nitrogen was used as both tank pressurant and line purge gas in the oxidizer system, and hydrogen gas was used to pressurize the liquid hydrogen supply tank. Liquid flowrates were controlled by the tank pressure settings and through the use of cavitating venturis. The gaseous hydrogen flowrate was controlled through use of parallel dome-type pressure regulators and a sonic line orifice. Gaseous fluorine was employed to provide a hypergolic ignition system.

Gas Sampling System

Gas samples were withdrawn from the closed end of an acoustic cavity through an orifice, the thermal conditioning system shown in Fig. 21 and into 75- or 300-milliliter high-pressure stainless cylinders. Sample pressure was reduced by flow through a 0.020-inch-diameter, long sonic orifice. The conditioning system reduced the temperature from the cavity temperature to the 250 to 300 F level, which allowed

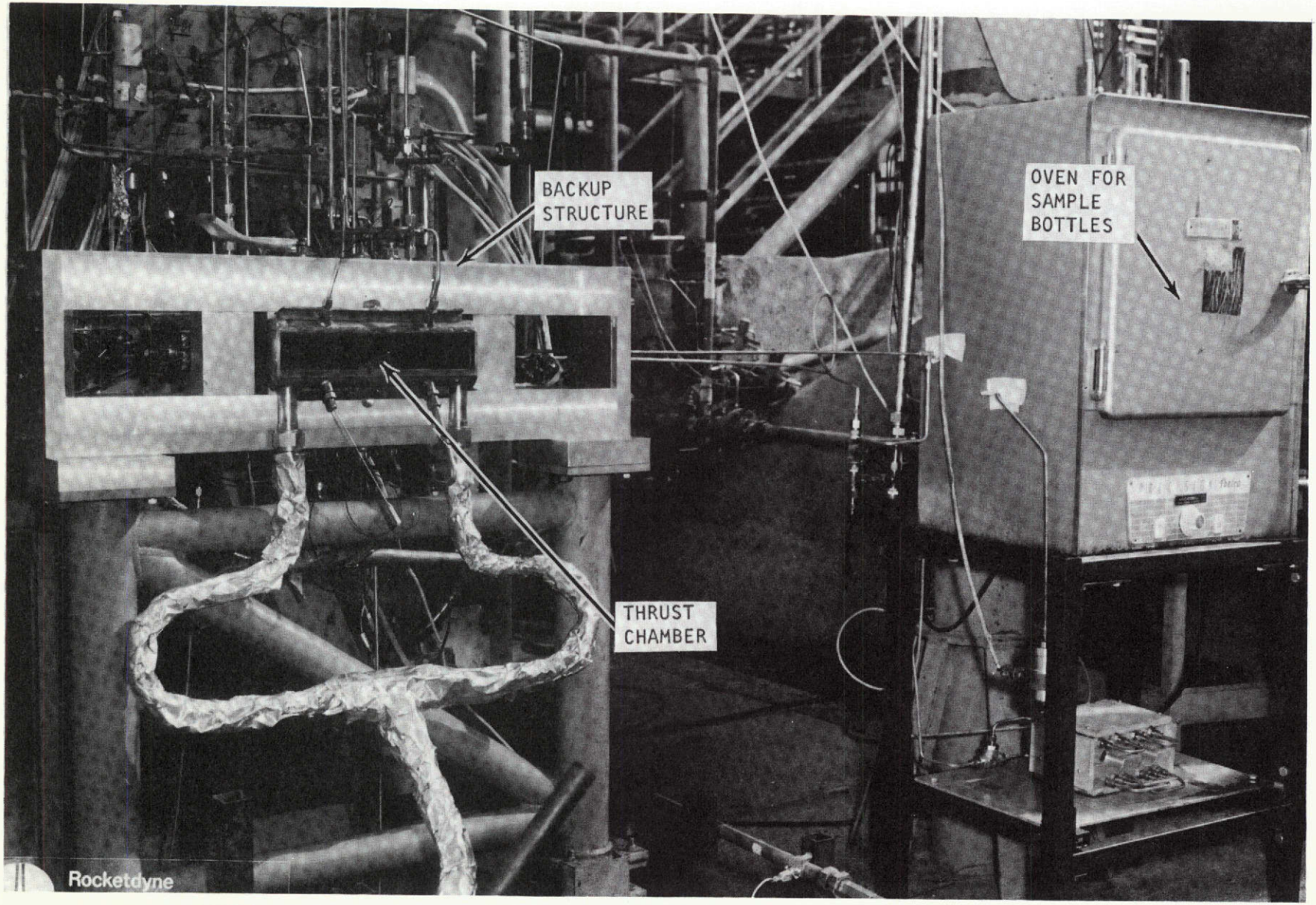

5AA-10/12/72-S1B

Figure 18. Nan Stand Showing Nozzle End View of Linear Aerospike Thrust Chamber Inside Backup Structure

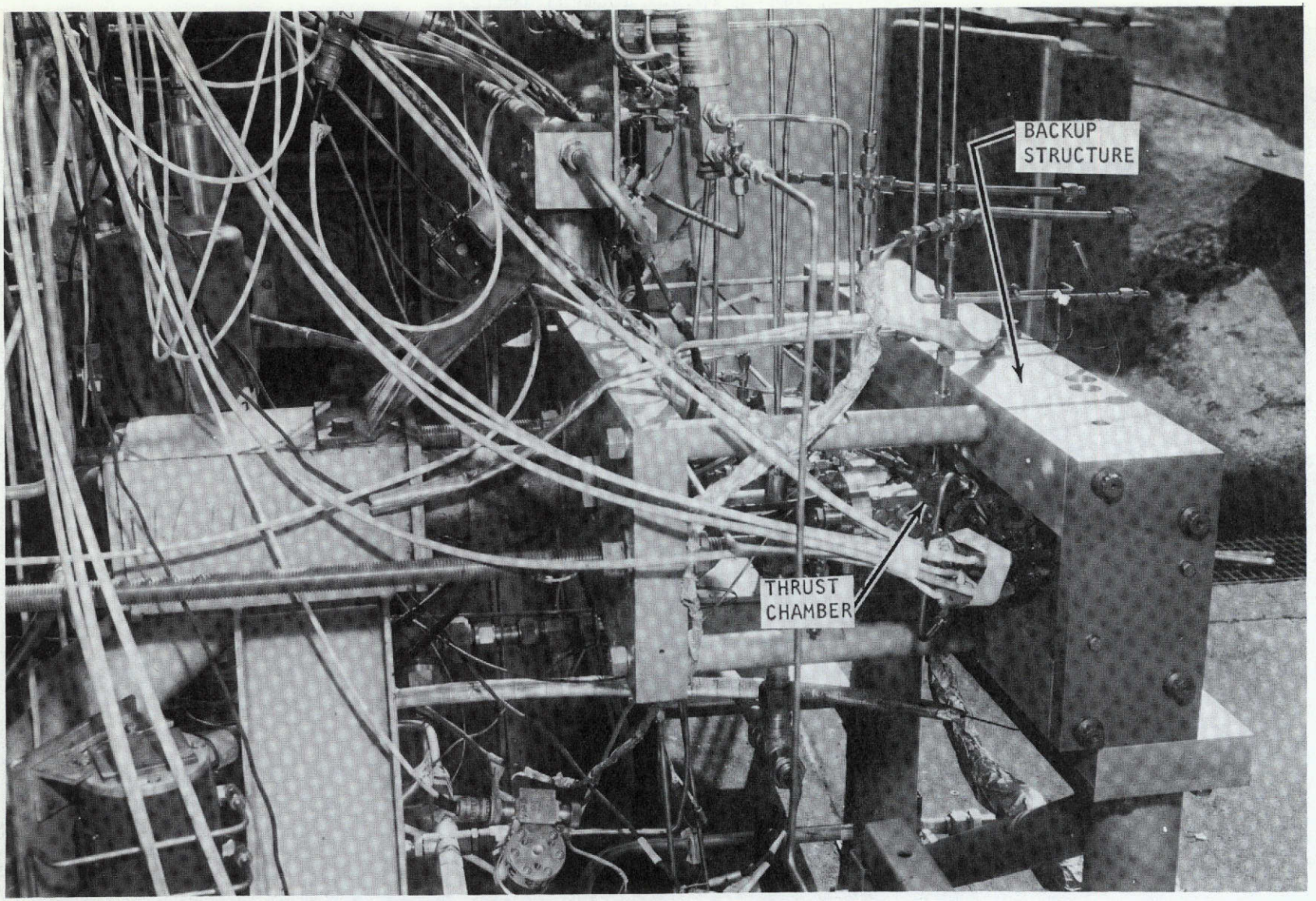

5AA34-10/2/72-S1C

Figure 19. Nan Stand Showing Side View of Linear Aerospike Thrust Chamber Inside Backup Structure

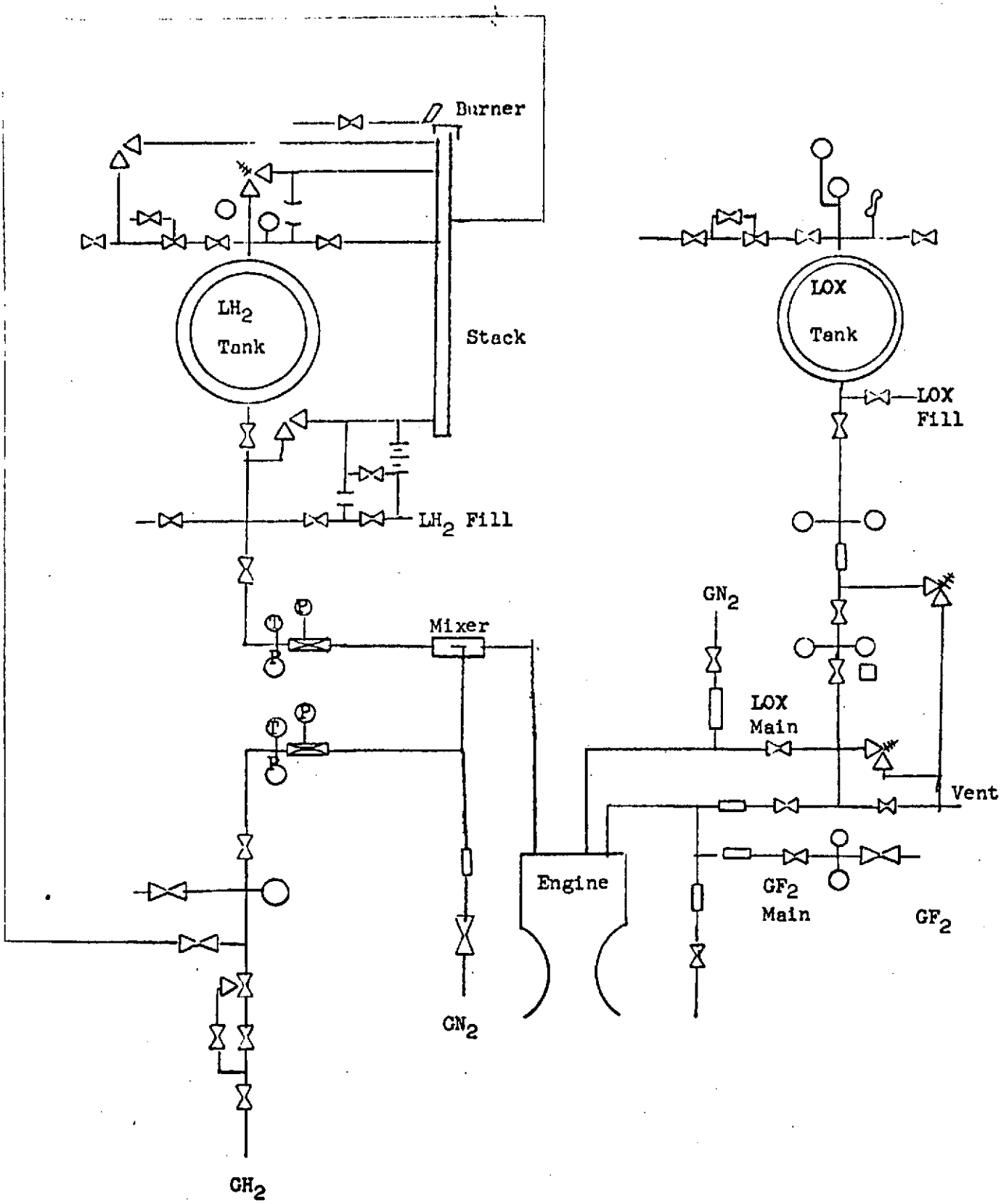

Figure 20. Schematic Representation of Nan Stand Test Facility Used for Acoustic Cavity Motor Firings

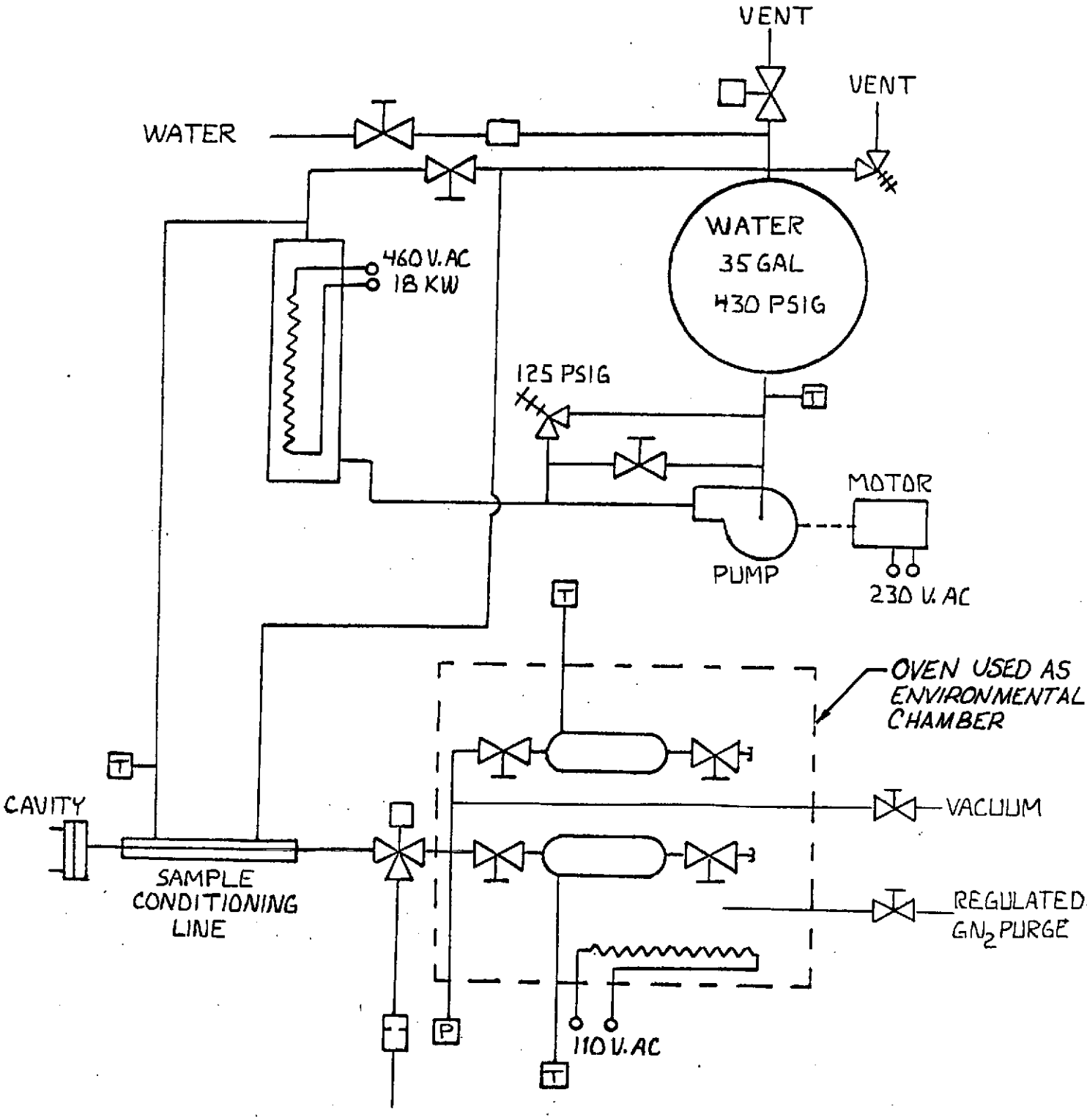

Figure 21. Schematic Representation of Acoustic Cavity Gas Sampling System

the gas to pass through valves without damage to the valve components but, nonetheless, prevented condensation of water. The sample gas temperature was reduced by passage through a coaxial heat exchanger formed by jacketing 30-inch lengths of stainless-steel tubing (a 0.125-inch outside diameter by 0.020-inch wall tube inside of a 0.250-inch outside diameter by 0.025-inch wall tube). Hot water was circulated through the annulus of the heat exchanger in a closed-loop system, passing in turn from a 35-gallon supply tank, through a 2.5-gpm Burke pump, a 15-kilowatt Chromalux heater, either the coaxial heat exchanger or a bypass loop, then back to the supply tank. Water temperature was maintained at 230 to 250 F. This water temperature was sufficient (with the 150 equivalent diameters of heat transfer length through which the gas sample passes in the heat exchanger) to ensure a gas temperature between 250 and 300 F, regardless of the temperature in the cavity itself.

As shown in Fig. 21, the sample gas passed from the heat exchanger through a remotely operated Hoke three-way ball valve into a sample bottle manifold or through a vent to the atmosphere. Two sample bottles, each equipped with hand-operated shutoff valves, were connected to the manifold. To prevent condensation of water from the sample, the entire system downstream of the heat exchanger was located inside the oven shown in Fig. 22. This maintained temperatures at approximately 300 F during the motor firings. The vent to atmosphere allowed a purging of atmospheric contaminants from the acoustic cavity and coaxial heat exchanger during the initial portion of a motor firing before the actual sample was withdrawn. Provision was made for evacuating the manifold and sample bottles downstream of the three-way valve with a Kinney vacuum pump before the motor firing. The hand-operated shutoff valves permitted the gas sample to be sealed in the bottle immediately after the motor firing.

MEASUREMENTS

During the linear aerospike engine firings, measurements were made of chamber pressure, overall propellant flowrates, and the flowrate of hydrogen sidewall coolant dumped overboard after passage around the acoustic cavities. Measurements were also made of injection temperature and pressure drop and of coolant jacket temperature increase and pressure drop. Additionally, the sample bottle temperature and pressure and the temperature of the sampling system water supply were measured. The operational parameters and the instrumentation used to measure them are summarized in Table 2.

The cavity temperature distribution was measured with six tungsten-5 percent rhenium/tungsten-26 percent rhenium thermocouples in each of the open cavities. Locations of the thermocouple junctions are shown in Table 3.

The electrical outputs of the various transducers were recorded by both direct reading Dynalog recorders and by a Beckman multichannel Model 210 digital data acquisition system.

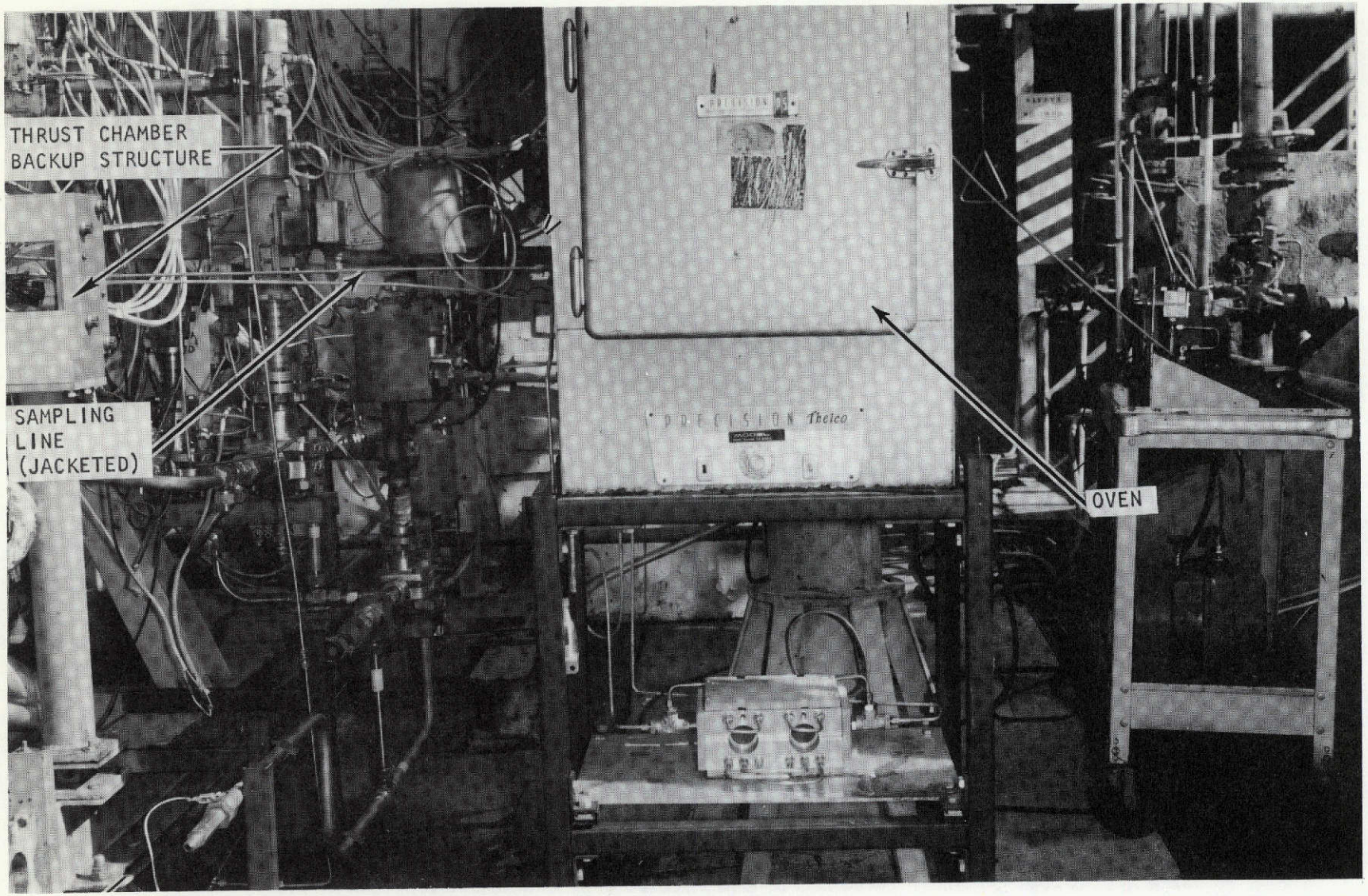

5AA-10/2/72-S1A

Figure 22. Cavity Gas Sampling System With Electric Oven for Sampling Bottles

TABLE 2. PARAMETERS MEASURED DURING LINEAR AEROSPIKE MOTOR FIRINGS

Parameter	General Method	Measurements	Transducer
Hydrogen Fuel System			
LH_2 Flowrate	Venturi ΔP	Upstream Temperature	Rosemount
		Upstream Pressure	Taber
		Throat Pressure	Taber
GH_2 Flowrate	Subsonic Venturi	Upstream Temperature	I/C T/C
		Upstream Pressure	Taber
		Venturi ΔP	Taber
	Sonic Venturi	Upstream Temperature	I/C T/C
		Upstream Pressure	Taber
		Throat Pressure	Taber
Coolant Jacket ΔP	In and Out Pressure	Inlet Pressure (2)	Taber
		Sidewall Outlet (2)	Taber
		Contour Wall Outlet (2)	Taber
Coolant Jacket ΔT	In and Out Temperature	Inlet Temperature (2)	I/C T/C
		Sidewall Outlet (2)	I/C T/C
		Contour Wall Outlet (2)	I/C T/C
Side Wall Coolant Dump	Critical Orifice	Upstream Dump Temperature (2)	I/C T/C
		Upstream Dump Pressure (2)	Taber
Liquid Oxygen System			
LO_2 Flowrate	Turbine Flowmeter	Flowmeter Pressure	Taber
		Flowmeter Temperature	I/C T/C
		Volume Flow	Flowmeter
Thrust Chamber			
Chamber Pressure		Injector Face Pressure	Taber
H_2 Injector ΔP		Fuel Manifold Pressure	Taber
LO_2 Injector ΔP		Oxidizer Manifold Pressure	Taber
Acoustic Cavity			
Gas Temperature		T/C Probes (12)	W/R T/C
Cavity Wall Heat Flux	Transient Temperature	Backwall Temperature	I/C T/C
Cavity Bleed Rate	Critical Orifice	Upstream Pressure	Taber
Other Measurements			
Sample Temperature		Sample Bottle Temperature	I/C T/C
Sample Line Temperature		Conditioning Water Temperature	I/C T/C
Sample Pressure		Sample Manifold Pressure	Taber

TABLE 3. CAVITY THERMOCOUPLE (TC) LOCATIONS

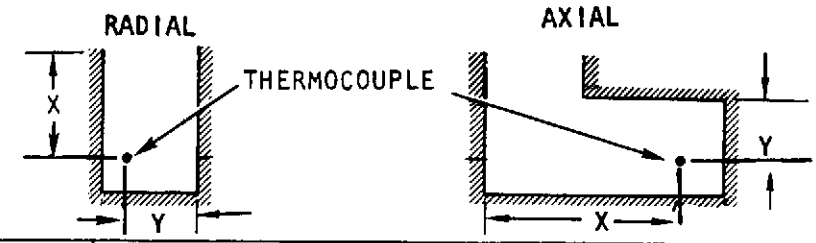

Cavity Type	Cavity Location*	Thermocouple	X-Position, inches	Y-Position, inch
Radial	Left	TC-A	0.95	0.2
		TC-B	1.44	0.4
		TC-C	1.93	0.2
		TC-D	2.41	0.4
		TC-E	2.89	0.2
		TC-F	3.39	0.4
	Right	TC-G	0.95	0.4
		TC-H	1.44	0.2
		TC-J	1.93	0.4
		TC-K	2.41	0.2
		TC-L	2.89	0.4
		TC-M	3.39	0.2
Axial	Left	TC-A	1.47	0.4,0.2**
		TC-B	1.96	0.2
		TC-C	2.45	0.4,0.2
		TC-D	2.95	0.2
		TC-E	3.44	0.4,0.2
		TC-F	3.94	0.2
	Right	TC-G	1.47	0.2
		TC-H	1.96	0.4,0.2
		TC-J	2.45	0.2
		TC-K	2.95	0.4,0.2
		TC-L	3.44	0.2
		TC-M	3.94	0.4,0.2

*Chamber side as viewed in the flow direction, i.e., from injector to throat

**0.4 for 0.59-inch-wide cavity; 0.2 for 0.42-inch-wide cavity

CAVITY GAS SAMPLE ANALYSIS

Pressure-Volume-Temperature (PVT) Determination

The composition of the cavity gas samples was expected to comprise essentially only H_2 and H_2O, and the compositional analysis scheme was set up accordingly. With significant concentrations of water in a sample, the only practical method of analysis was through pressure-volume-temperature measurements, which allow the condensible and noncondensible species to be distinguished. If the only noncondensible species is H_2, then only PVT measurements are required to analyze the cavity gas samples. However, because of the possibility of other noncondensible constituents, e.g., trapped air or purge gas, the noncondensible portion of selected gas samples was also analyzed by gas chromatography.

The relative mole fractions of condensible and noncondensible species in the samples withdrawn from the bottom of the acoustic cavities during the motor firings with the linear aerospike thrust chamber were determined by measuring the variation of gas pressure within the sampling cylinder at temperatures varying from approximately 50 to 270 F. These measurements were made with the system shown schematically in Fig. 23. The Tabor ΔP pressure transducer and the silicone oil-filled lines were used to ensure that the entire volume of sample gas could be maintained at the nominal sample bottle temperature while the Heise pressure gage was maintained at ambient temperature; otherwise, condensation of water vapor in the cooler portions of the system would produce erroneous results.

The analysis of the pressure-temperature data was made through use of vapor pressure data for water and Dalton's law of partial pressures

$$p_t = p_{H_2O} + p_{NC}$$

where p_t, p_{H_2O}, p_{NC} are the total pressure and the partial pressures of water vapor and noncondensible gas respectively. The partial pressure of the noncondensible gas will obey the gas law as temperature is varied. If the partial pressure of the water is less than the vapor (saturation) pressure, it will obey the gas law; otherwise, the partial pressure will equal the vapor pressure. Therefore, the sample pressure will vary with sample temperature as

$$p = \frac{nRT}{V} = \frac{p_o T}{T_o}; \qquad X_{H_2O,o}\left(\frac{p_o T}{T_o}\right) < p_{vap}$$

$$p = p_{vap} + X_{NC,o}\left(\frac{p_o T}{T_o}\right); \qquad X_{H_2O,o}\left(\frac{p_o T}{T_o}\right) > p_{vap}$$

where the volume of the condensed liquid has been neglected compared to the sample volume. This pressure-temperature behavior is illustrated in Fig. 24. Although a numerical curve-fitting procedure (least squares) could have been used quite readily, the available data could be analyzed with sufficient accuracy by examining the asymptotic pressure variations at high and low temperatures, as

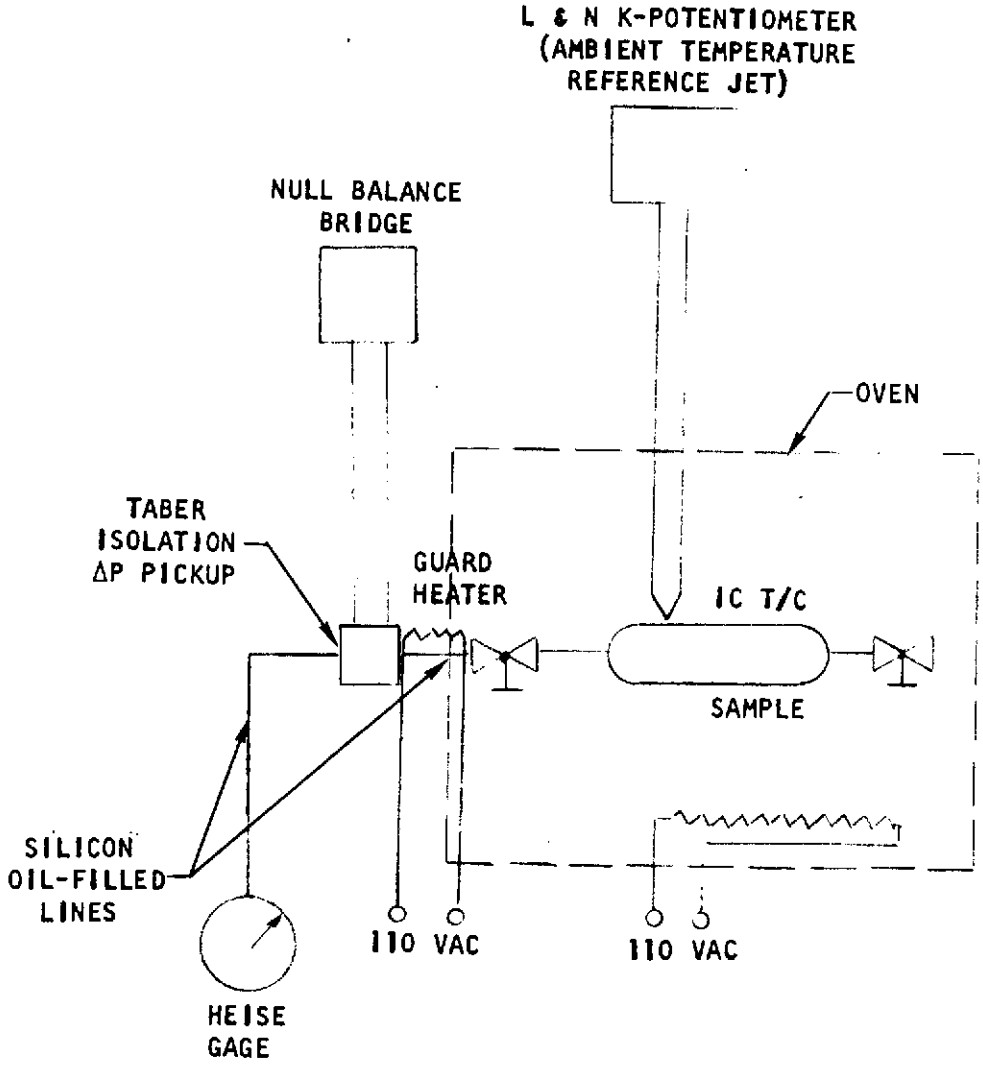

Figure 23. Schematic Representation of Test Apparatus for P-V-T Determination of Cavity Gas Samples

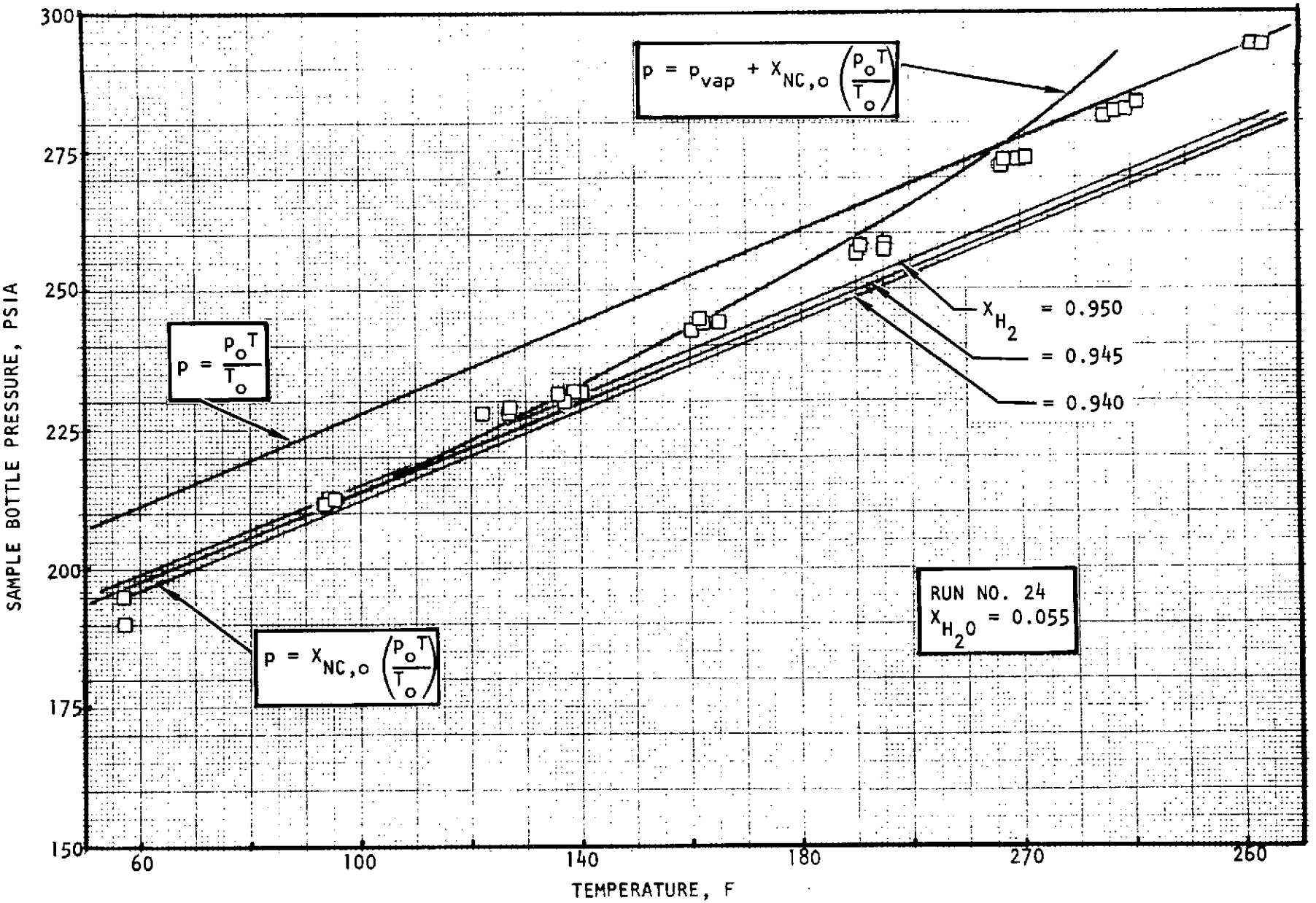

Figure 24. Variation of Sample Bottle Pressure With Temperature for Sample Taken During Run 24

shown in Fig. 24. From inspection of the data at high temperatures, the upper straight line could be drawn, i.e., select values for p_o and T_o. Similarly, from inspection of the data at low temperatures, the lower straight line (asymptote) could be drawn, i.e., select $X_{NC,o}$. The transition curve could then be calculated by simply adding the vapor pressure to the expression for the lower asymptote. The mole fractions could thus be estimated within ~0.5 percent. This procedure was used with all of the pressure-temperature sample data to determine the mole fractions of condensibles (water) and noncondensibles.

Chromatographic Analysis

After making pressure-temperature measurements, the noncondensible fraction of an acoustic cavity gas sample was analyzed directly for H_2, O_2, N_2, and argon by gas chromatography. Water was first removed by passing the sample through a dry ice cold trap before it entered the gas chromatograph. A 5-Angstrom molecular sieve column was used in the gas chromatograph with a helium carrier and a thermal conductivity detector. The detector's response, displayed as peaks on a strip chart recorder, was made quantitative by comparison to the responses of high-purity neat gases and standard gas mixtures.

MOTOR FIRING RESULTS

Cavity gas temperature data were obtained during 32 motor firings made with the linear aerospike thrust chamber. The first 19 of these firings were made with a radial cavity, 0.59 inch wide. Seven of the remaining 15 tests were made with an 0.59-inch-wide axial cavity; the remainder were made with an 0.42-inch-wide axial cavity. Gas samples were taken during 11 of the tests. The operating conditions for these tests are summarized in Table 4, along with the calculated c* efficiencies.

Cavity Gas Temperatures

Cavity gas temperatures were measured at the thermocouple locations shown in Table 3. The measured temperatures exhibited significant transient behavior of the kinds illustrated in Fig. 25 and 26. The temperature fluctuated continuously around a mean temperature which approached a steady-state condition in a manner that varied both with location in the cavity and from firing to firing. Consequently, cavity gas temperature data were summarized both in terms of the maximum local temperatures recorded in each motor firing (Table 5) and in terms of the time-averaged local temperatures averaged over the last 1.0 second of each 4.0-second motor firing (Table 6). Time-averaged temperatures measured during firings without hydrogen bleed in the cavities are plotted in Fig. 27 and 28 for the radial cavities and the 0.59-inch-wide axial cavity, respectively. The extent of the run-to-run variation in temperatures is evident from these plots. However, as discussed below, this variation is believed to reflect an actual variation in temperature rather than measurement uncertainty. In spite of this variability, it may be observed that the temperatures in the right cavity tend to be distinctly higher than those in the left cavity.

TABLE 4. SUMMARY OF OPERATING AND PERFORMANCE DATA FROM LINEAR AEROSPIKE MOTOR FIRINGS

Run	Chamber Pressure, psia	Mixture Ratio	Total Propellant Flow, lbm/sec	η_{c^*} (1)	Gas Sample
4	486	5.04	11.66	0.915	
6	516	5.16	12.07	0.945	
7	606	5.98	15.43	0.89	
9					
10	604	5.54	15.46	0.87	Yes
11	608	5.49	15.40	0.88	Yes
12	602	5.48	15.43	0.87	
14	886	6.97	22.07	0.94	
15	888	6.59	21.65	0.945	Yes
16	--(2)	6.67	21.85	--	
17	909	6.64	21.97	0.955	Yes
18	912	6.67	21.89	0.96	
19	917	6.65	21.97	0.965	
20	853	7.41	20.35	0.995	
21	871	6.64	20.16	1.00	Yes
22	883	6.83	20.89	0.985	
23	896	7.03	21.34	0.98	Yes
24	898	6.90	21.50	0.985	Yes
25	911	6.66	21.75	0.96	
26	844	6.65	19.50	1.00	
27	841	7.16	20.05	0.985	
29	870	6.36	20.07	0.99	
31	1063	6.73	25.13	0.98	
32	1073	6.70	25.89	0.955	
33	862	5.91	18.44	1.05	Yes
34	868	6.36	20.25	0.98	
35	893	6.84	20.80	1.00	
36	900	6.52	21.25	0.975	Yes
37	1095	5.82	27.78	0.985	
38	1109	5.69	28.73	0.86	Yes
39	1107	5.68	28.50	0.865	Yes
40	1106	5.74	29.07	0.85	

(1) Based on measured injector face pressure with corrections for Rayleigh loss and for variation of throat are during a firing

(2) No valid pressure measurement

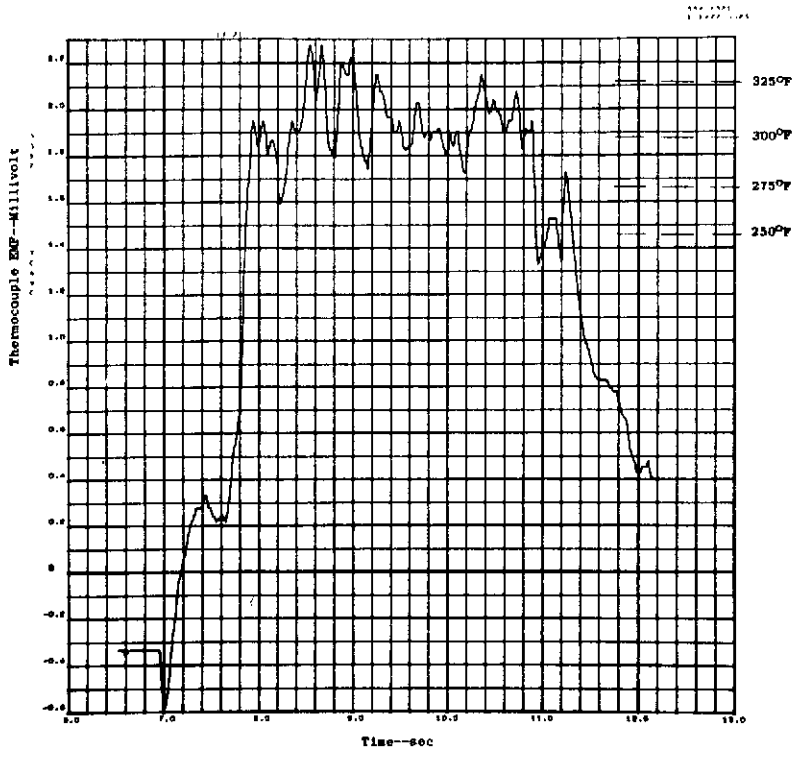

Figure 25. Thermocouple EMF for Thermocouple TC-C Table 3 During Run No. 21

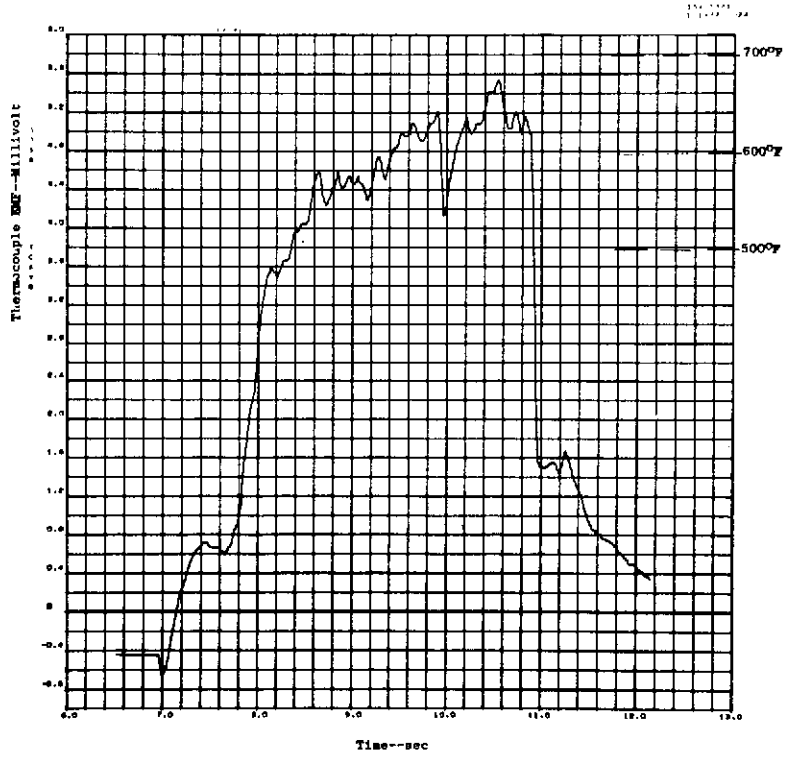

Figure 26. Thermocouple EMF for Thermocouple TC-B Table 3 During Run No. 21

TABLE 5. MAXIMUM CAVITY GAS TEMPERATURES MEASURED DURING LINEAR AEROSPIKE MOTOR FIRINGS

Run	Cavity*	Cavity Bleed, lbm/sec	Maximum Cavity Gas Temperature, F											
			TC-A	TC-B	TC-C	TC-D	TC-E	TC-F	TC-G	TC-H	TC-J	TC-K	TC-L	TC-M
4	Radial-1	0.000	1095	960	650	660	430	--	1510	--	--	780	660	705
6		0.000	900	815	585	505	315	--	1090	990	--	645	595	545
7		0.000	990	975	675	665	455	--	1280	1095	--	785	775	725
9		0.000	915	580	515	545	420	490	--	640	610	--	510	425
10		0.000	1095	980	845	700	570	630	--	1170	1070	--	860	760
11		0.000	1115	990	830	690	580	620	--	1140	1050	--	725	730
12		0.000	1050	965	795	645	395	495	--	1100	1000	--	715	625
14		0.007	710	490	550	355	275	345	--	740	525	--	470	385
15		0.007	670	435	525	345	270	325	--	695	515	--	455	315
16		0.000	1105	1190	840	860	615	515	--	1245	1075	--	915	1000
17		0.000	1085	1180	810	815	585	495	--	1215	955	--	850	940
18		0.025	545	360	260	305	240	275	--	355	380	--	370	290
19		0.025	495	345	230	285	225	260	--	350	360	--	330	275
20		0.000	330	755	460	--	340	350	--	860	555	745	535	615
21		0.000	355	670	340	--	285	300	--	795	510	690	455	520
22		0.0071	280	210	210	--	200	200	--	220	225	225	215	205
23		0.0071	290	205	205	--	195	195	--	225	225	230	225	215
24		0.0255	195	180	175	--	135	175	--	175	185	180	180	175
25		0.0255	180	175	175	--	175	175	--	170	180	180	175	165
26	Axial-1	0.000	315	655	365	--	290	315	--	765	595	585	400	450
27		0.000	350	700	370	--	310	335	--	860	645	690	450	560
29		0.0070	--	245	245	--	--	220	425	265	270	265	250	250
31		0.0071	--	240	260	--	240	235	425	255	255	245	235	230
32		0.000	--	705	430	--	425	395	750	800	475	745	500	580
33	Axial-2	0.000	--	280	405	270	--	250	195	270	--	130	115	110
34		0.000	--	255	335	215	--	180	200	280	--	125	110	105
35		0.0071	--	140	75	70	--	80	160	165	--	115	105	80
36		0.0069	--	140	75	70	--	70	160	155	--	120	105	85
37		0.000	--	710	435	645	--	525	235	310	--	165	145	135
38		0.000	--	465	510	505	--	330	225	300	--	170	145	125
39		0.0070	--	270	150	90	--	90	275	185	--	110	110	90
40		0.0068	--	200	145	90	--	85	255	170	--	140	140	100

*Radial-1 dimensions:depth = 4.30, width = 0.59; Axial-1 dimensions:depth = 5.0, width = 0.59; Axial-2 dimensions:depth = 5.0, width = 0.42

**See Table 3 for thermocouple locations in cavities

TABLE 6. TIME-AVERAGED CAVITY GAS TEMPERATURES DURING FINAL 1.0 SECOND OF LINEAR AEROSPIKE MOTOR FIRINGS

Run	Cavity	Cavity Bleed, lbm/sec	Time Average* Cavity Gas Temperature, F											
			TC-A	TC-B	TC-C	TC-D	TC-E	TC-F	TC-G	TC-H	TC-J	TC-K	TC-L	TC-M
4	Radial-1	0.000	975	855	550	430	300	--	1470	--	--	620	550	500
6		0.000	790	725	480	395	290	--	1050	900	--	565	545	345
7		0.000	960	955	660	605	365	--	1230	1060	--	700	725	545
9		0.000	905	575	495	535	410	480	--	615	595	--	495	415
10		0.000	1070	975	805	695	520	720	--	1145	1040	--	830	725
11		0.000	1075	990	810	690	530	605	--	1125	1030	--	795	705
12		0.000	1110	865	695	580	345	400	--	1045	910	--	655	440
14		0.007	695	485	520	335	270	330	--	690	515	--	460	330
15		0.007	670	430	505	335	265	315	--	645	495	--	445	315
16		0.000	960	1035	780	685	605	505	--	1205	1060	--	910	985
17		0.000	885	960	730	720	565	455	--	1115	915	--	850	925
18		0.025	490	355	260	305	235	270	--	340	370	--	335	280
19		0.025	480	305	225	280	225	250	--	330	345	--	315	270
20		0.000	325	745	410	--	315	340	--	790	410	730	500	600
21		0.000	335	630	310	--	275	295	--	775	795	620	380	500
22		0.0071	275	205	205	155	195	195	--	205	215	210	200	195
23		0.0071	275	200	195	145	190	190	--	215	220	220	210	210
24		0.0255	185	175	170	115	170	170	--	160	170	170	160	160
25		0.0255	135	170	170	110	170	170	--	170	175	170	165	155
26	Axial-1	0.000	300	600	310	105	275	300	835	700	555	490	345	390
27		0.000	295	670	315	110	300	320	915	835	535	635	370	520
29		0.0070	--	230	235	95	--	215	400	250	245	245	235	240
31		0.0071	--	255	250	95	235	230	390	245	255	245	230	230
32		0.000	--	665	405	125	375	370	700	750	375	690	465	540
33	Axial-2	0.000	--	260	385	215	--	210	180	250	--	110	110	95
34		0.000	--	250	320	175	--	135	180	265	--	115	100	90
35		0.0071	--	110	75	75	--	75	145	145	--	105	100	80
36		0.0069	--	125	75	70	--	70	150	145	--	105	95	80
37		0.000	--	645	390	625	--	480	220	270	--	155	135	130
38		0.000	--	405	490	375	--	310	205	265	--	145	125	110
39		0.0070	--	205	100	70	--	70	170	125	--	100	100	75
40		0.0068	--	170	125	75	--	85	225	150	--	120	125	90

*Obtained by numerically integrating the temperature data

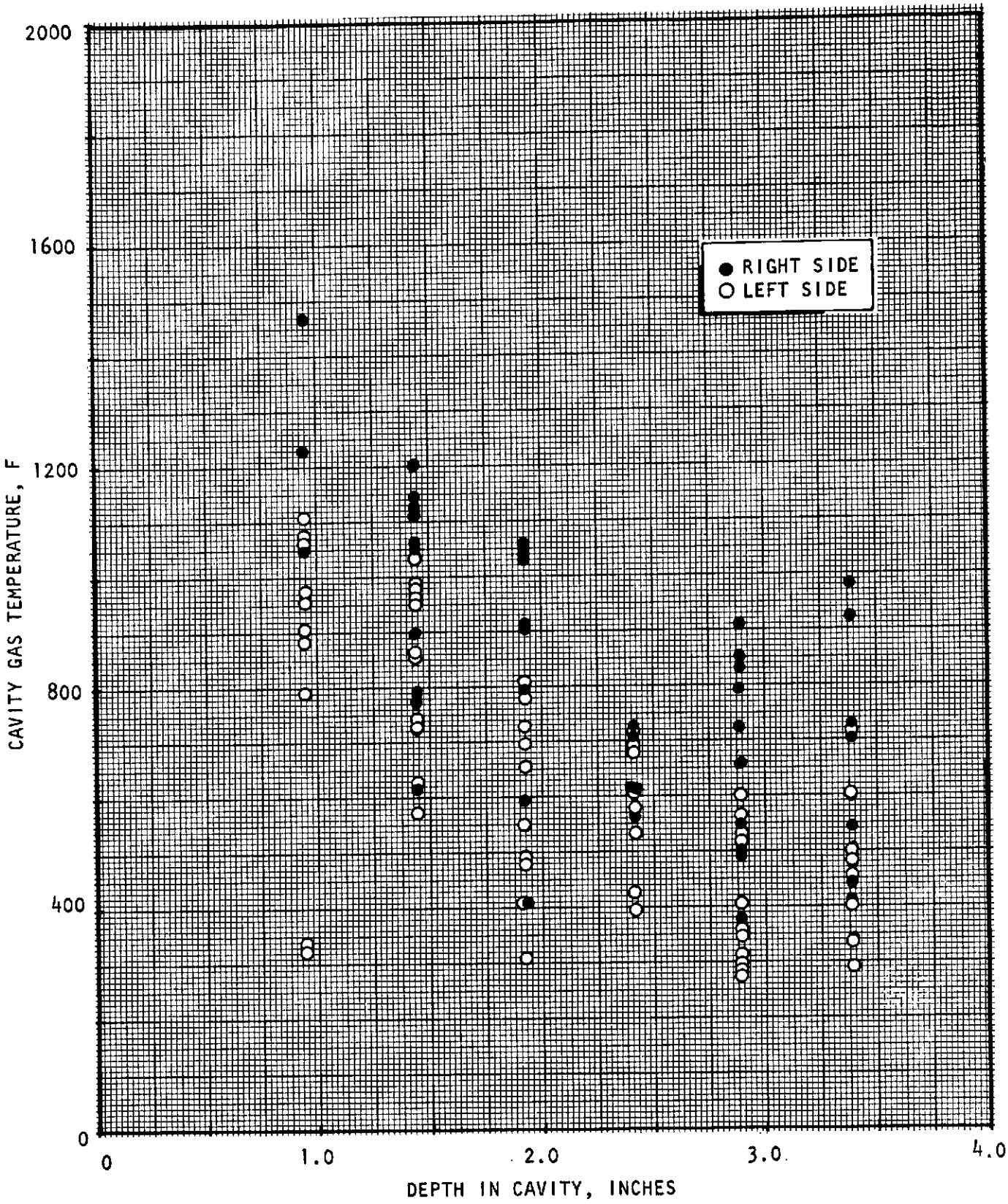

Figure 27. Time-Averaged Cavity Gas Temperature Distribution in Radial Cavities Without Hydrogen Bleed

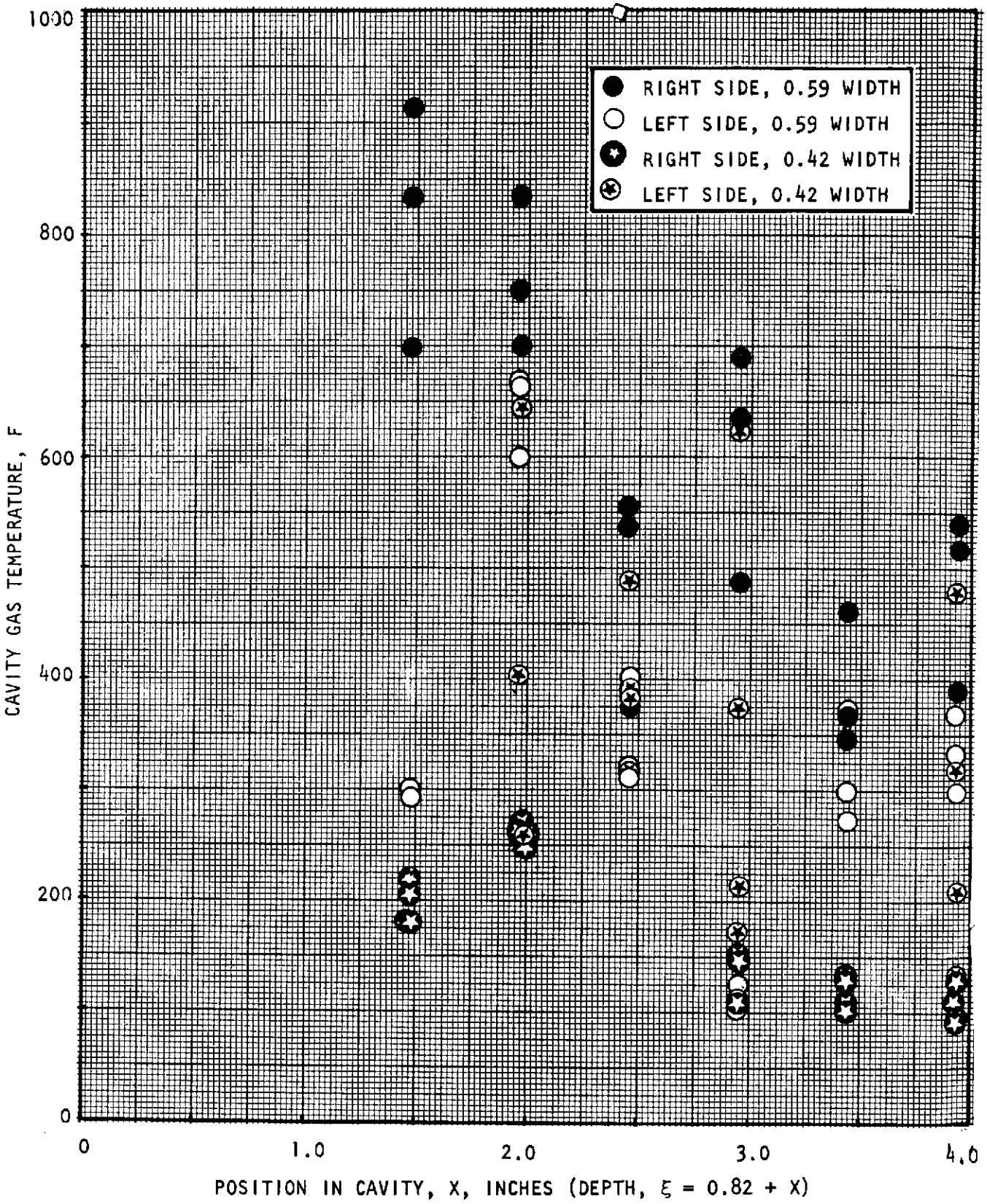

Figure 28. Time-Averaged Cavity Gas Temperature Distribution in Axial Cavities Obtained Without Hydrogen Bleed

Time-averaged temperatures measured during firings with a bleed flow of hydrogen through the cavities are plotted in Fig. 29 and 30. With bleed into the cavities, both the overall temperature level and the difference between the right and left side of the chamber are reduced; however, careful examination indicates that there is a relatively high degree of scatter for data obtained at nominally similar conditions.

The cavity temperatures may have been affected by hydrogen leaks that developed during the course of the motor firing program. Visual examination of the thrust chamber during the test program indicated that a number of small leaks developed in the braze joints sealing the hydrogen coolant passages at the downstream edge of the basic cavity structure, 0.80 inch from the injector face. However, the effects of these leaks on the cavity gas temperatures should be reduced by the presence of the TZM cavity filler blocks, which were used in all the motor firings and which reduced the cavity width, or distance from downstream cavity edge to the injector, to either 0.59 or 0.42 inch. During the combustion model calculations, described in the preceding Analytical Studies section of this report, the boundary layer attachment point was calculated to occur at 0.65 inch from the injector. Beyond the attachment point, no upstream recirculation is expected. Consequently, any leaking gas from the sidewall coolant passages should be swept downstream rather than back into the cavity. The cold hydrogen sidewall coolant is not expected to move up the wall against the main flow except, possibly, if massive leakage were to occur. An overall heat balance calculation was made to aid evaluation of the importance of these leaks. The value of a normalized heat transfer parameter ψ, which corresponds to a normalized ratio of coolant temperature rise to wall heat flux, was calculated.* The variation in the value of ψ should be inversely proportional to the change in leakage from the sidewall.

The variation in ψ through the course of the motor firing program, as calculated for tests without cavity bleed, is shown in Fig. 31. The curves were calculated from a least-square fit of the data. Not only is the shift in the parameter less than the scatter in the data, but the shift is positive rather than negative, as required for developing leaks. Consequently, the development of leakage during the program can be considered to be small and, therefore, the effect on the cavity gas temperatures should be negligible.

The aforementioned systematic difference between the gas temperatures measured in the right and left sidewall cavities cannot be explained readily. As just discussed, hydrogen coolant leaks at the cavity entrance do not appear significant, or, at least did not change during the test series. Therefore, leakage is not a likely explanation. However, it is possible that a minor leak may have developed at the left sidewall cavity during the three preliminary checkout firings and not changed during subsequent tests. The effect of such a leak would not be evident from the analysis, but could produce some reduction in gas temperature at the cavity opening. Secondly, the removal of the gas samples from the bottom of the left sidewall cavity could, possibly, draw cooler gas into the

*Derivation of ψ is presented in Appendix D.

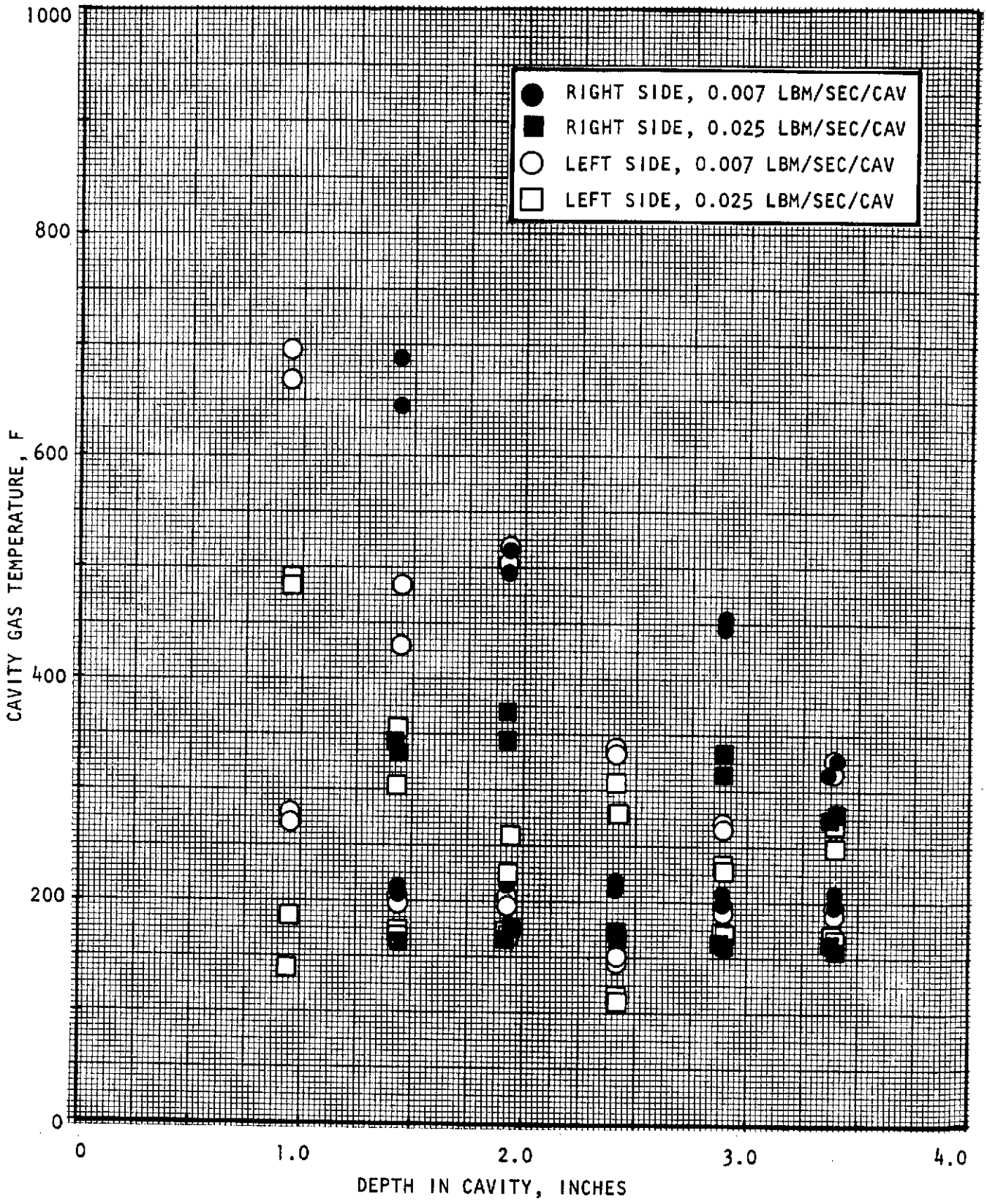

Figure 29. Time-Averaged Cavity Gas Temperature Distribution in Radial Cavities With Hydrogen Bleed

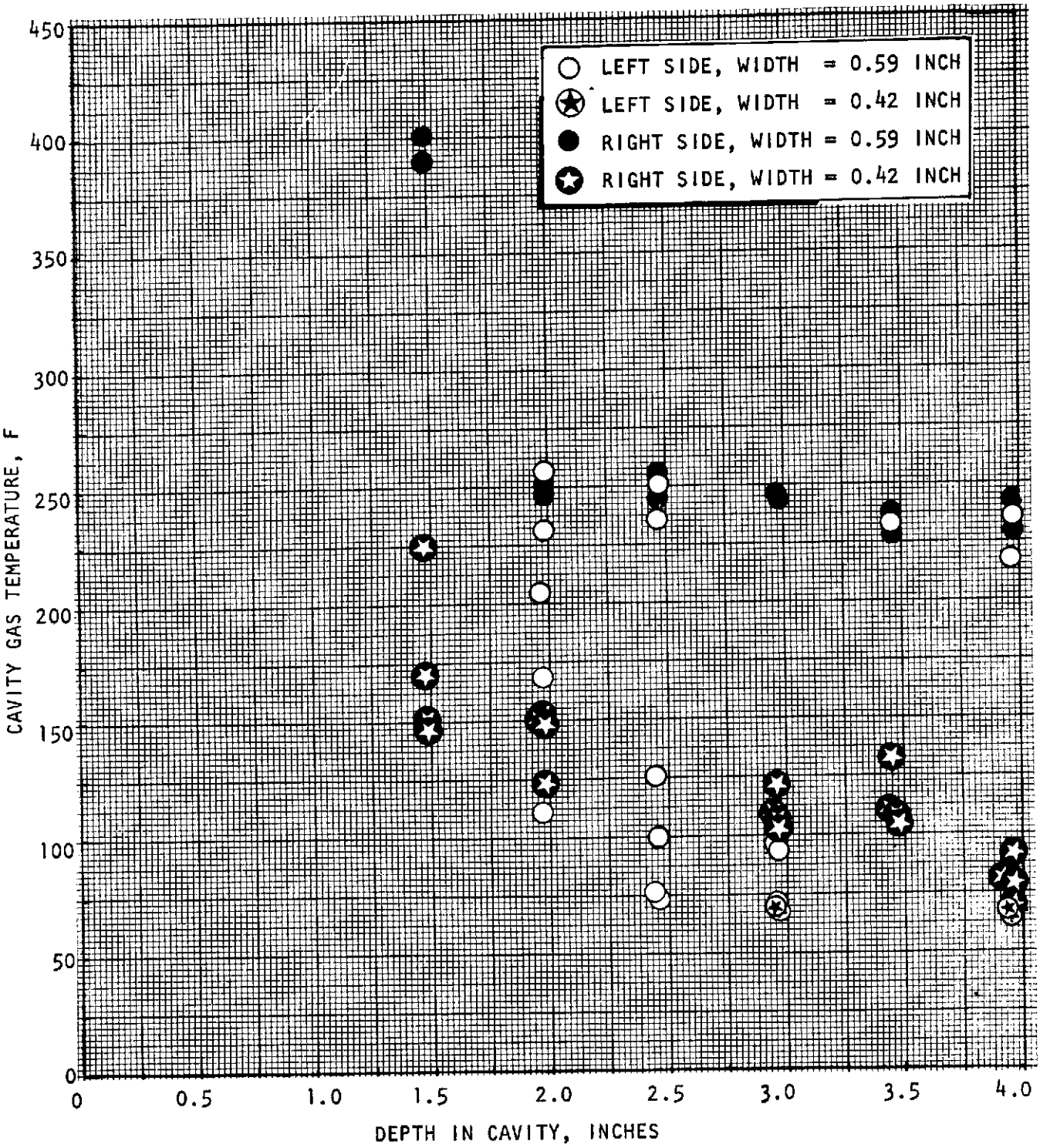

Figure 30. Time-Averaged Cavity Gas Temperature Distribution in Axial Cavities With a Hydrogen Bleed Rate of 0.007 lbm/sec Into Each Cavity

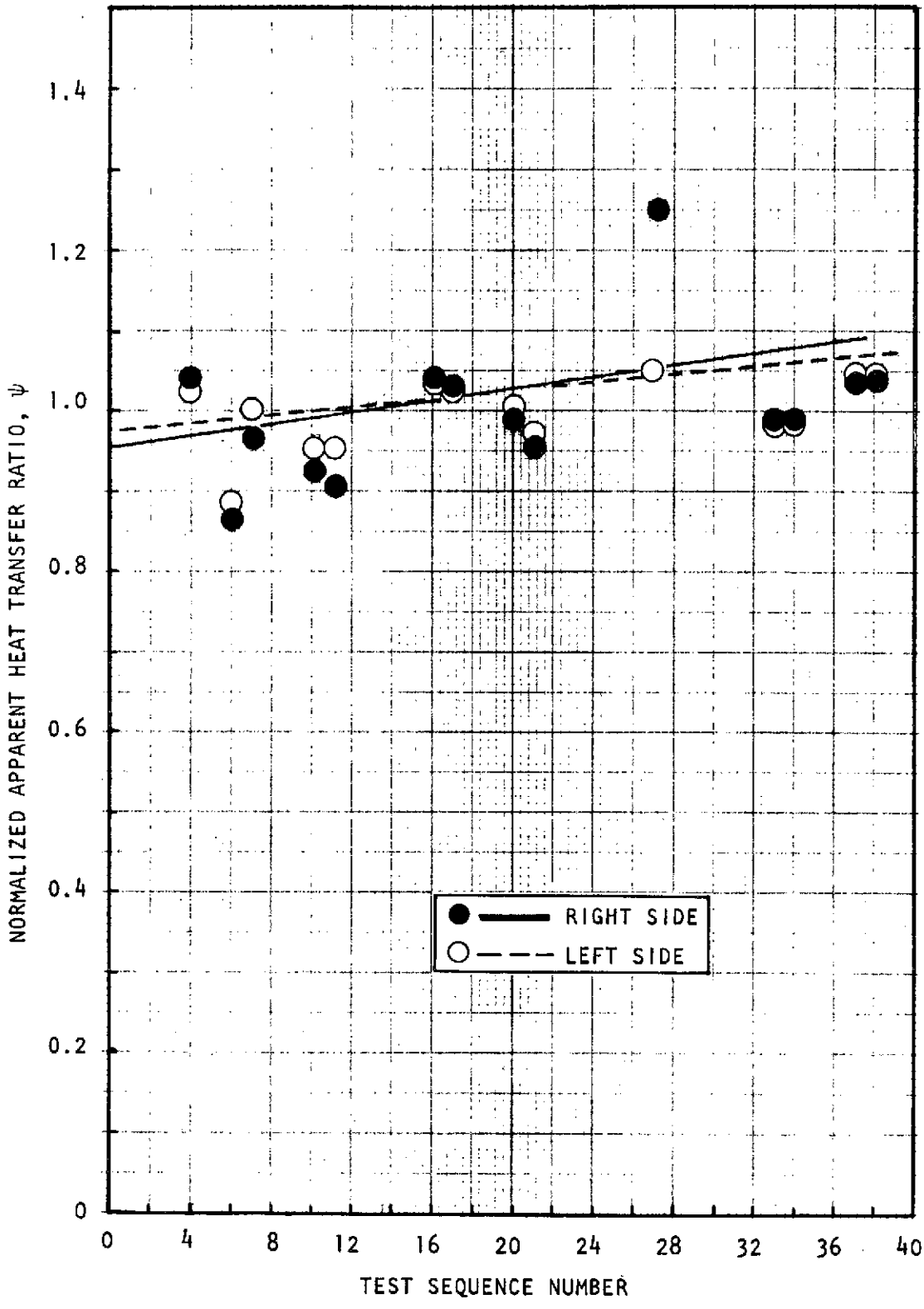

Figure 31. Variation of Normalized Apparent Heat Transfer Parameter ψ Through Motor Firing Program

cavity from the region immediately downstream of the injector face. Because neither of these effects occur in an engine application of acoustic cavities, it was considered appropriate to base the correlation of cavity temperatures upon the data obtained in the right sidewall cavity whenever possible.

From Tables 5 and 6, it is evident that temperature measurements were not obtained at all thermocouple locations during the various motor firings. This was the result of the failure of the thermocouples (usually at the hot junction) during the course of the firings. Moreover, the emf output of the thermocouples in the tests preceding a complete failure was sometimes erratic. All thermocouple data were recorded in Tables 5 and 6, but a few suspicious values were disregarded in developing the temperature correlations described below.

Correlation of Cavity Temperatures

Generally, for acoustic cavity design, the sound velocity and time-averaged density of the gas contained in the cavity have been assumed spatially uniform for simplicity. A nonuniform sound velocity and density is more difficult to utilize analytically with confidence and has been avoided except for calculations to assess the importance of particular assumed sound velocity distributions. Nevertheless, allowance should be made for this nonuniformity. Therefore, it appears appropriate to utilize the temperature data from the motor firings to define both the temperature distribution and a spatial average temperature because each may be appropriate for cavity design calculations. Moreover, because the temperature data tend to be scattered, the influence of changes in cavity configuration or operating conditions may appear more clearly in the spatial average temperature than in the distributions themselves.

Correlations for the cavity temperature distributions were developed by curve fitting the temperature data with the correlation equation described in Appendix E, which was developed from a simplified heat transfer analysis. This equation may be written as

$$T(\xi) = T_s + (T_o - T_s)e^{-M\xi} \tag{1}$$

where

ξ is a streamwise coordinate (see sketch below)

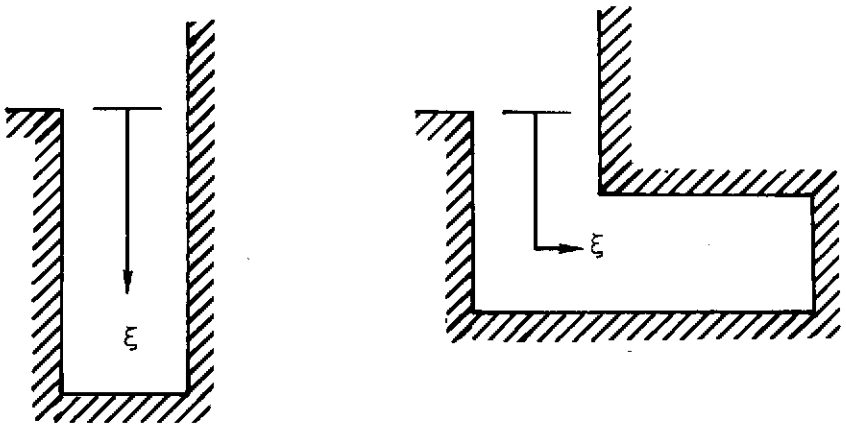

(The coordinate ξ is taken along the midwidth of the cavity.)

T_s is the cavity wall temperature (assumed constant and equal to its initial value)

T_o is the gas temperature at the entrance to the cavity

M is an empirically based coefficient defined by

$$M = \frac{1}{2}\left\{K_1\left(\frac{w_{H_2}}{A_c}\right)^n + \left[K_1^2\left(\frac{w_{H_2}}{A_c}\right)^{2n} + K_2\left(\frac{P_c}{A_c}\right)\right]^{1/2}\right\}$$

in which

w_{H_2} is the cavity bleed mass flowrate. P_c is the perimeter of the cavity, A_c is the cross-sectional area of the cavity. K_1, K_2, and n are empirical coefficients, to be determined from the data.

For correlation purposes, a value of 50 F was assigned to the wall temperature, T_s. The values of T_o and M were determined by a least-squares fit of the relation

$$\ln (T - T_s) = \ln (T_o - T_s) - M\xi$$

to the data. For the radial cavity, the analysis results are given in Table 7.

TABLE 7. EVALUATION OF EMPIRICALLY BASED COEFFICIENTS T_o AND M FROM RADIAL CAVITY TEMPERATURE DATA

Bleed Rate, lbm/sec	T_o, F	M, $inch^{-1}$	Bleed Mass Flux, $lbm/in.^2$-sec
0.000	1550	0.306	0.000
0.007	945	0.447	0.0091
0.0255	750	0.493	0.0332

The results for T_o are also plotted as the upper curve of Fig. 32. From the variation of M with cavity bleed flowrate, values of K_1, K_2, and n were calculated directly. The numerical values determined for these constants are $K_1 = 0.580$, $K_2 = 0.076$, and $n = 0.19$. Also it was found possible to fit the data from the 0.59-inch-wide axial cavities equally well with the same empirical coefficients T_o, M, K_1, K_2, and n.

Because insufficient data were available from the 0.42-inch-wide cavity, it was not possible to explicitly determine the effect of the bleed coolant flowrate on T_o from these data. Therefore, the results obtained from the 0.59-inch-wide cavity were employed to estimate this effect by assuming the fractional change of the difference $T_o - T_s$ was the same in both cases. Employing this assumption, the lower curve shown on Fig. 32 was obtained. A check on the validity of this estimate was obtained by comparing spatially averaged temperatures, as described below.

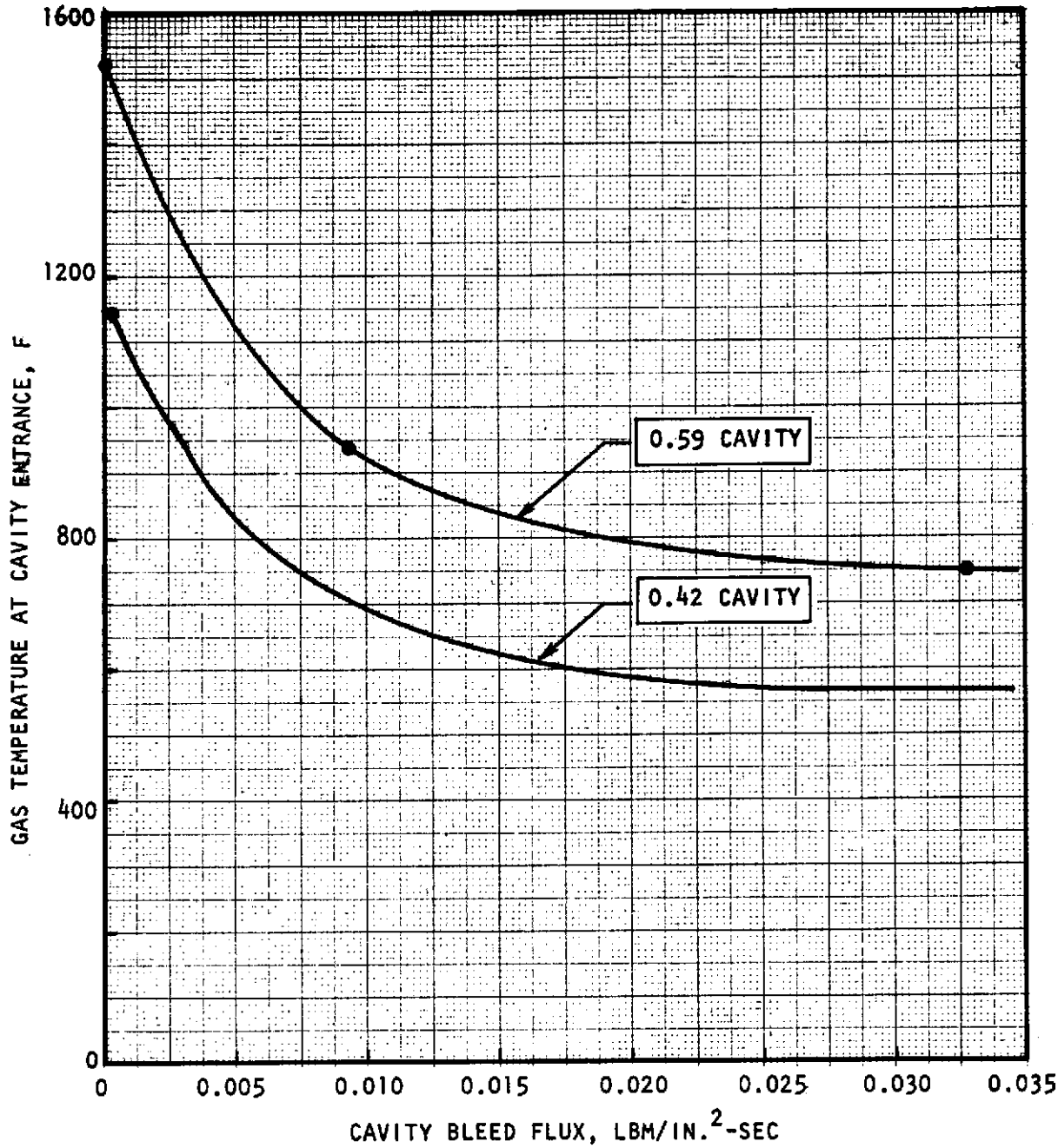

Figure 32. Predicted Effect of Cavity Hydrogen Bleed Upon Gas Temperature at Open End of Acoustic Cavity

Figure 33 shows the results of the correlation of the experimental cavity temperature data with the cavity temperature model for the 0.59-inch-wide radial and axial cavities (right side of the chamber) with no hydrogen bleed into the cavity. Figure 34 shows the correlation between the experimental data and the temperature model for the radial cavity on the opposite side (left) of the chamber at various levels of cavity bleed. Considering the extent of data scatter in both Fig. 33 and 34, there is satisfactory agreement between the data and the model.*

The fact that temperature data from both the 0.59-inch-wide axial and radial cavities could be correlated with the same value for T_o (1550 F) lends some support to the approach being used. An attempt was made to relate this temperature to the results from the combustion model calculations. Figures 9 and 12 show that 1550 F corresponds to the mainstream combustion gas temperature at a distance of 0.60 to 0.65 inch from the injector face, which corresponds, in turn, to the attachment point location of the mainstream flow. This suggests that the gas next to the cavity entrance in the recirculation region upstream of the attachment point consists primarily of gases swept back from the attachment point with approximately the same temperature as at that point. With cavity bleed, the combustion gas outside the cavity entrance would be cooled by mixing with the hydrogen gas leaving the cavity. Consequently, the reduction in T_o obtained from the data with increasing bleed flowrate shown in Table 7 would be expected.

Because the spatial-average temperature appears to be a significant parameter, either for estimating average cavity sound velocity and density or for assessing the influence of changes in operating conditions, this average temperature was calculated from the correlations and from the temperature data directly.

Spatially averaged temperatures were calculated from the data directly by either integration (trapezoidal rule) over the cavity depth interval spanned by the six thermocouple locations (Table 3) when temperature data were available from all locations, or simple linear average of available thermocouple data when data were missing from some locations. The average temperatures thus obtained are shown in Table 8.

*It may be noted from Fig. 33 and 34 that, with no cavity bleed, the agreement between the data and the correlation is better for the cavity data on the right side of the chamber than on the left. In correlating the data for the tests with cavity bleed, more measurements were available for comparison in the left side cavity.

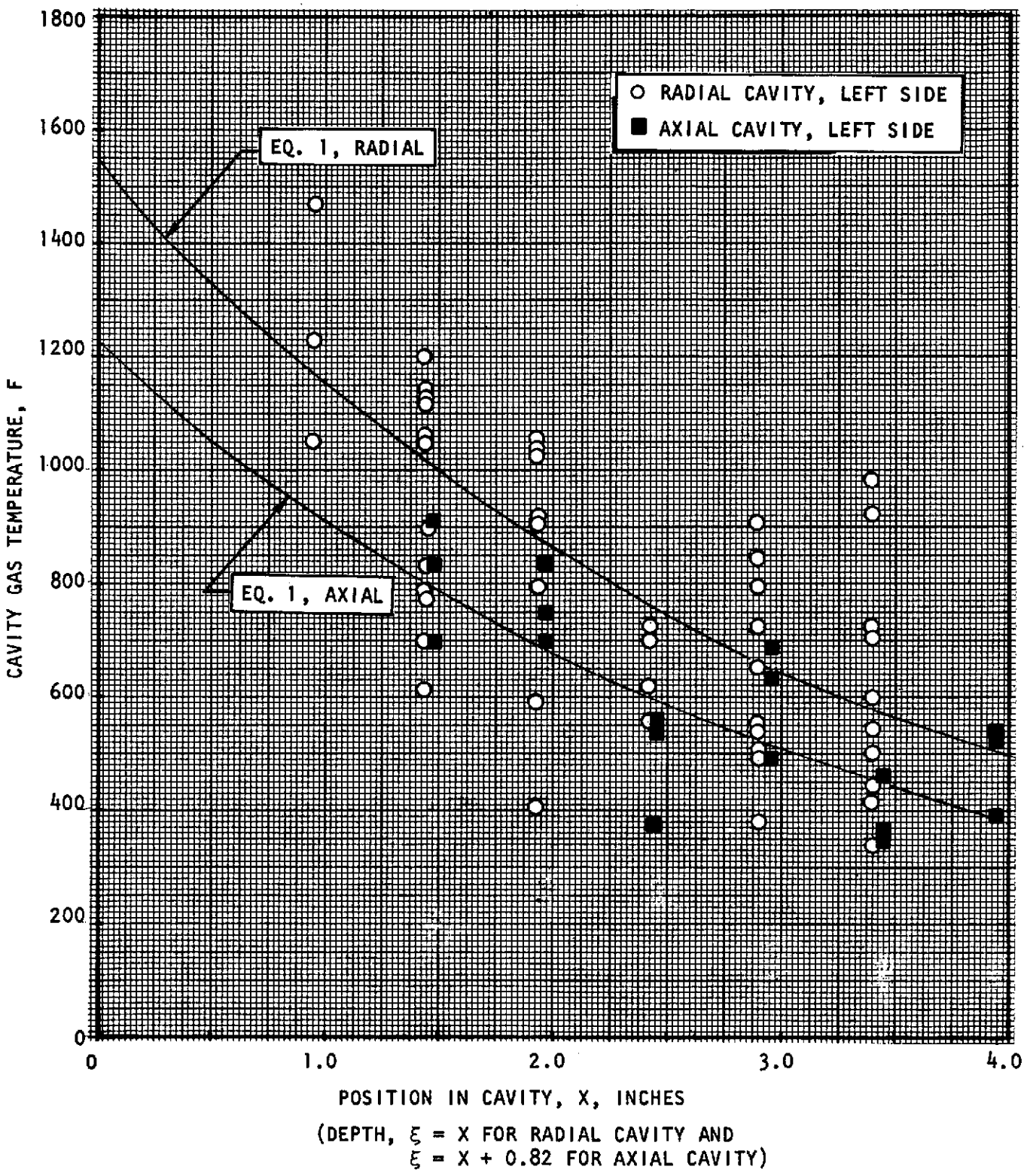

Figure 33. Comparison of Temperature Distributions With Radial and Axial Cavities With Results from the Cavity Temperature Model

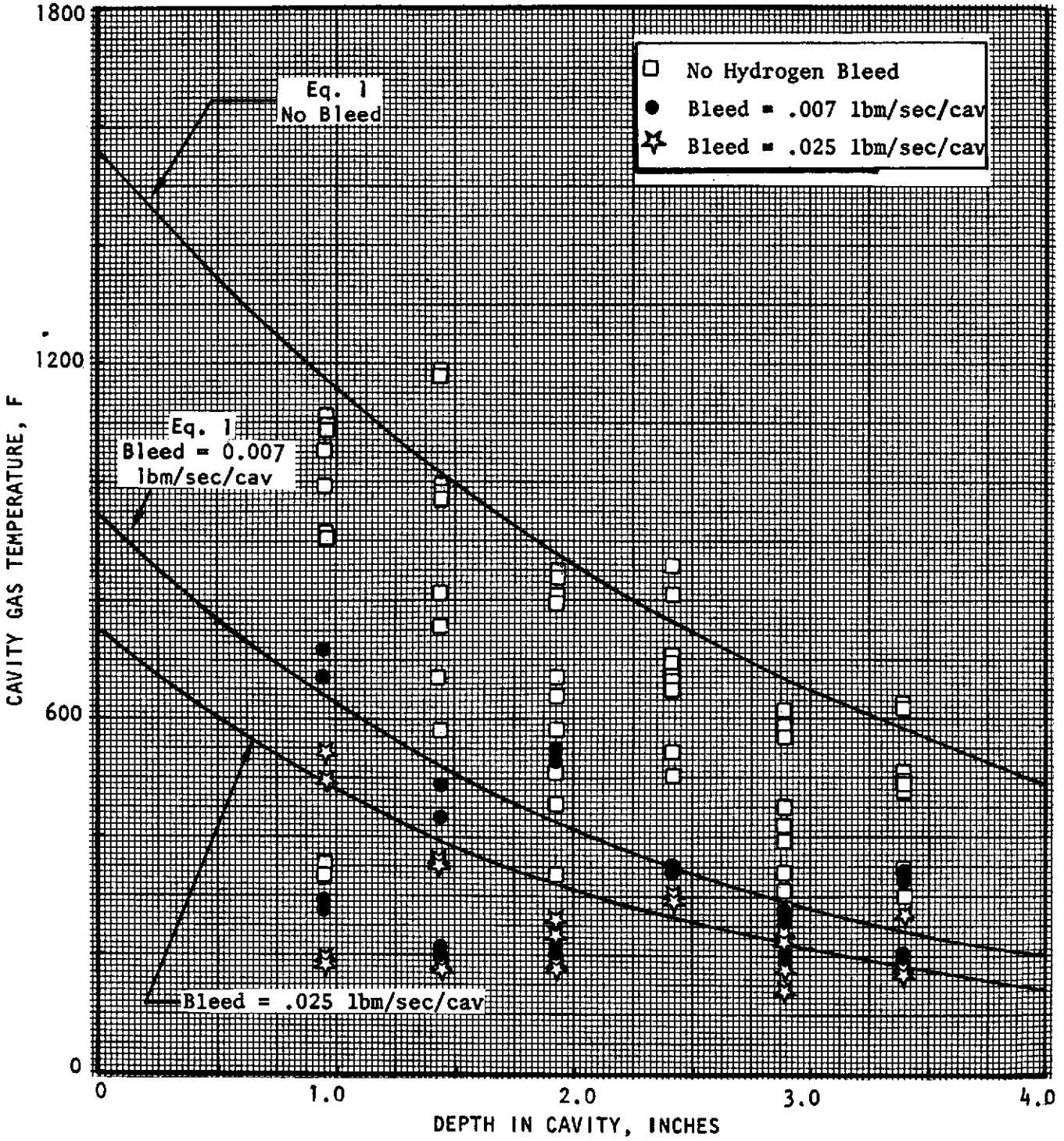

Figure 34. Effect of Hydrogen Bleed on Gas Temperature in Radial Cavities on Left Side of Chamber

Note that this temperature has been averaged only over the interval of cavity depth over which temperature data were obtained. For the axial cavities, this depth interval extended from 0.99 inch to 3.31 inches, while the total depth was 4.3 inches. For the axial cavities, the depth interval extended from 1.47 to 3.91 inches in a cavity with a total depth of 5.0 inches.

The corresponding average cavity gas temperature may be obtained from the correlation expression by integration of the measurement depth interval, i.e.,

$$\overline{T} = \frac{T_o}{M(\xi_2 - \xi_1)} \left[e^{-M\xi_1} - e^{-M\xi_2} \right] \qquad (2)$$

Average cavity temperatures calculated from this expression are also shown in Table 8. The agreement between the temperature values obtained from the correlation expression and from direct integration of the data is good for both the radial and 0.59-inch-wide axial cavities. Based upon the assumption that the gas temperature in the cavities was defined by the temperature of the gases swept back from the flow attachment point, the same value of T_o was initially assigned to both the 0.59- and 0.42-inch-width cavities.

TABLE 8. COMPARISON OF SPATIAL AVERAGE CAVITY GAS TEMPERATURES OBTAINED FROM DATA DIRECTLY AND FROM CORRELATION EQUATION 2

Configuration	Cavity Width, inch	Bleed Rate, lbm/sec	Experimental Average Temperature, F*	Correlated Average Temperature, F
Radial	0.59	0.000	850	840
		0.007	345	365
		0.0252	240	270
Axial	0.59	0.000	580	575
		0.007	260	245
Axial	0.42	0.000	355**	455(355)***
		0.007	140	205(160)***

*Trapezoidal rule integration.
**Based on data from cavity in left sidewall of chamber. Other average temperatures are based on data from right sidewall cavity.
***Figures in parentheses are calculated from T_o based upon conditions at axial location of 0.48-inch, which is intermediate between the downstream edge of the cavity and the attachment point. Other temperatures were calculated from T_o based on attachment point conditions.

Although this definition for T_o was both simple and attractive on physical grounds, a poor correlation was obtained when it was used with the data obtained from the 0.42-inch-wide axial cavity. Conversely, the mainstream gas temperature at the axial location of the downstream edge of the cavity could also be a reasonable choice for T_o. The difference between these two definitions would not significantly affect the prediction for the 0.59-inch-wide cavity because its downstream edge is near the attachment point (0.60 to 0.65 inch from the injector face). When the temperature at the downstream cavity edge was used for the 0.42-inch-wide case, a better agreement was obtained. As shown in Fig. 9, this value for T_o at a cavity width of 0.42 inch is 900 F. However, the best fit to the average cavity temperature data was obtained when T_o was 1150 F, which corresponds to the mainstream gas temperature at an intermediate axial location between the downstream edge of the cavity and the attachment location of the mainstream flow. The agreement is fairly good if the value of T_o corresponding to the temperature midway between the downstream edge of the cavity entrance and the attachment point is used (the numbers in parentheses of the last column of Table 8).

Note that a significant reduction in average cavity gas temperature with decrease in axial cavity width is indicated by the data (Table 8). For comparison, corresponding spatial average temperature results are shown in Fig.35 which were obtained previously in the Lunar Module Ascent engine-type hardware with an unbaffled injector and the NTO/N_2H_4-UDMH (50-50) propellant combination (Ref. 4).

Results From Cavity Gas Sampling

Gas samples were withdrawn from the acoustic cavity located in the left sidewall of the chamber during 11 of the motor firings. These samples were analyzed through use of the pressure-temperature measurement technique described earlier, to determine the mole fractions of water and noncondensible gases, and also by gas chromatography to determine the composition of the noncondensible gases. The results are summarized in Table 9 . The pressure-temperature data from four of the samples could not be used because of evident losses in sample pressure with time, probably due to leakage in the valves on the sample bottles but possibly due to solubility of the gas in the oil used in the pressure measurement line. The leakage in the sample bottle mixture globe valves, when it occurred, appeared to be seepage through the valve stem packing when the valves were in the open position. Therefore, the relative mole fractions of condensible and noncondensible are shown for only seven samples. Representative data from one of the latter samples are plotted in Fig. 24, described previously.

Also shown in Table 9 are results from the gas chromatographic analysis of the noncondensible gases. Nine samples were analyzed. Results from each of these analyses suggest that in addition to hydrogen, only small quantities of air were contained in the samples. The trace gases appear in roughly the same proportion as they occur in air. The air is probably due to imperfect vacuum in the sample bottle previous to sampling. Therefore, it may be concluded that the cavity gases are composed of only hydrogen and water.

Clearly, the gas sampling results indicate the mole fractions of hydrogen are >0.93 and those of water are <0.07. Unfortunately, no trend of composition with mixture ratio, chamber pressure, or cavity bleed coolant flowrate is evident from

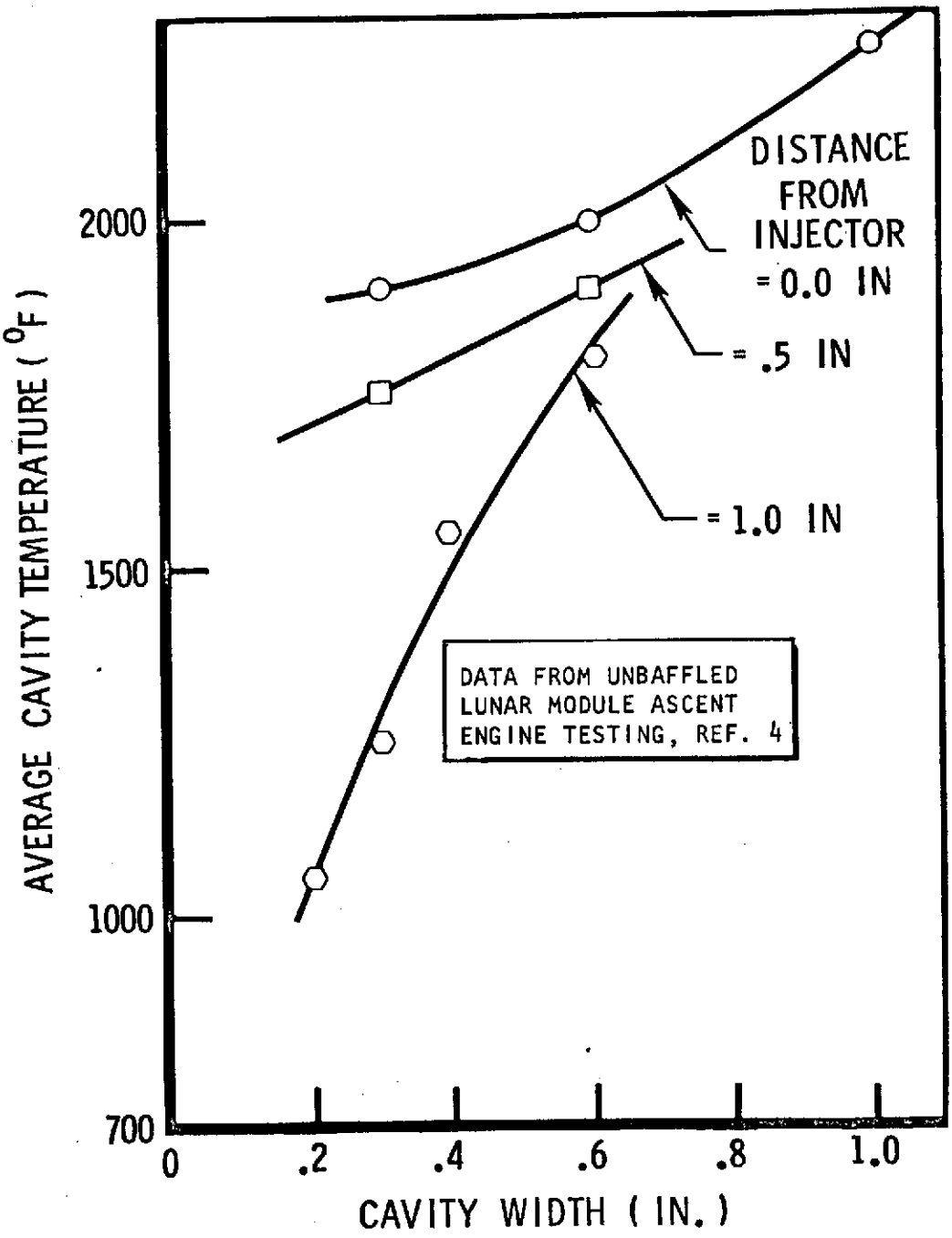

Figure 35. Measured Average Cavity Temperature versus Slot Width Obtained in Unbaffled Lunar Module Ascent Engine

TABLE 9. SUMMARY OF CAVITY GAS SAMPLE ANALYSIS

Run	Cavity Bleed Rate, lb/sec	Chamber Pressure, psia	Overall Combustion Chamber Mixture Ratio	X_{H_2O}	$X_{noncondensible}$	Composition Noncondensible Gases			
						$X^1_{H_2}$	$X^{1*}_{N_2}$	$X^1_{O_2}$	X^1_{Argon}
10	0.000	604	5.54	NS	NS**	0.998	0.002	Trace	Trace
11	0.000	608	5.49	0.060	0.940	0.999	0.001	None	None
15	0.007	888	6.59	NS	NS	NS	0.011	0.003	None
17	0.000	909	6.64	NS	NS	0.990	0.008	0.002	None
21	0.000	871	6.64	0.000	1.000	0.999	0.001	None	Trace
23	0.0071	896	7.03	0.065	0.935	0.999	0.001	Trace	None
24	0.0255	898	6.90	0.055	0.945	0.996	0.004	None	None
33	0.000	862	5.84	<0.01	>0.990	0.990	0.085	0.013	Trace
36	0.0069	900	6.52	0.000	1.000	0.989	0.011	Trace	None
38	0.000	1109	5.69	0.045	0.955	>0.99	Not Analyzed		
39	0.007	--	5.68	NS	NS	>0.99	Not Analyzed		

*X: Mole fraction of total gas; X^1 mole fraction of noncondensible portion of sample
**NS: Unsatisfactory results, usually due to leakage

the results. The fact that a high mole fraction of water was found in a sample obtained at the highest cavity bleed rate is a result that is difficult to explain theoretically. This lack of correlation may indicate a similar lack of sensitivity of the composition to these parameters or it may indicate a deficiency in the experimental techniques. Relative to design calculations, the lack of apparent correlation suggests the use of constant mole fractions with an uncertainty in the cavity gas composition of $X_{H_2O} = 0.04 \pm 0.03$. The corresponding average molecular weight is $\overline{MW} = 2.64 \pm 0.41$, or an uncertainty of 18.2 percent.

The accuracy of the value for the water mole fraction measured in Runs 23 and 24, $X_{H_2O} \sim 0.06$, is suspect because it represents a two-phase condition at the pressure and measured temperature conditions in the cavity. For example, in the case of Run 24 at a chamber pressure of 898 psia, the measured mole fraction corresponds to a partial pressure of 49 psia. However, the vapor pressure for water at the average cavity temperature of 620 R measured in Run 24 (see column 7 of Table 10) is only 4.8 psia; consequently, the remaining water must have existed in either a highly supersaturated condition or as a mist. In either case, it is unlikely that an accurate sample could be drawn through the 0.020-inch-diameter sonic orifice (see page 26) at the bottom of the cavity.

Analysis of Variation in Cavity Gas Composition

The composition of the gas contained in the cavities and the temperature existing at the cavity entrance were expected to be closely related and, therefore, an attempt was made to develop a relationship. The temperature at the cavity entrance may be inferred from the measured spatial average cavity temperature through use of the temperature correlation expression. Moreover, the gas composition at the cavity entrance, and presumably throughout the cavity, is ultimately determined by the engine combustion processes which are modeled by the CSS combustion model. Finally, the temperature at the cavity entrance should correspond at least approximately to an adiabatic combustion condition of the mainstream gas mixed with any cavity hydrogen bleed. Therefore, it should be possible to estimate the temperature at the cavity entrance from the composition, through use of thermodynamic equilibrium calculations or, alternatively, the composition may be estimated from the temperature. This approach was tried with the data.

From the stoichiometric relation $nH_2 + O_2 \rightarrow (n - 2)H_2 + 2H_2O$ for complete combustion, the measured mole fractions of water vapor and hydrogen in the cavity gas samples may be converted into the equivalent combustion gas mixture ratios (W_{O_2}/W_{H_2}) in the cavities. Correspondingly calculated mixture ratios, which ranged from 0.00 to 0.52, are shown in Table 10 (fourth column). By reference to Fig. 9 and 12, it can be noted that this range of cavity gas mixture ratios is well within the range of mixture ratios calculated with the CSS analytical model in the flow region upstream of the wall attachment point of the main gas flow field.

Values of equilibrium flame temperature T_f, corresponding to these equivalent cavity gas mixture ratios, are also shown in Table 10 (fifth column). The average cavity gas temperatures corresponding to assumption of these flame temperatures for T_o

TABLE 10. COMPARISONS OF CALCULATED CAVITY TEMPERATURE (BASED UPON MEASURED COMPOSITION) WITH MEASURED TEMPERATURE AND OF CALCULATED COMPOSITION (BASED UPON MEASURED TEMPERATURE) WITH MEASURED COMPOSITION

Run	Chamber Pressure, psia	Measured Mole Fraction, H_2O	Equivalent Gas Mixture Ratio	Equilibrium Gas Temperature (T_o), R	Calculated Cavity Gas Temperature From Gas Composition, R	Measured Cavity Gas Temperature, R	Mixture Ratio From Measured Gas Temperature	Calculated H_2O Mole Fraction From Measured Gas Temperature
11	608	0.060	0.49	1320	940	1230	0.82	0.10
21	871	0.000	0.00	520	515	825	0.35	0.044
23	703	0.065	0.52	1370	950	655	0.28	0.035
24	898	0.065	0.44	1220	775	620	0.24	0.03
33	862	<0.01	<0.08	520 to 640	520 to 565	725	0.47	0.06
36	900	0.000	0.00	520	515	538	0.12	0.015
38	1109	0.045	0.35	1030	695	855	0.75	0.09

were calculated through use of Eq. 2 . The results are shown in Table 10 (sixth column) and may be compared with the measured average cavity gas temperature (seventh column). The agreement is good for three samples (11, 36, and 38), but was poor for the remaining four samples.

Employing the reverse procedure, the gas composition was calculated from the spatial average of the measured temperatures (seventh column, Table 10) by using Eq. 2 to calculate T_o and then, assuming the calculated T_o to be an equilibrium flame temperature, calculate the corresponding mixture ratio and mole fraction of water. The results are shown in the last two columns of Table 10. As might be expected, agreement between measured composition and that calculated from the measured cavity temperatures for the various samples were equivalent to the agreement between the measured temperature and that calculated from the measured composition.

Implicit in the method used above to calculate cavity gas compositions from measured temperatures are the assumptions that the turbulent diffusion processes for both enthalpy and molecular species in the mixing layer* above the acoustic cavities are similar. Moreover, the composition within the cavity is assumed to be uniform despite the variable cavity temperature, an assumption which is not very realistic except for the case of no cavity bleed (where the temperature varies due to heat losses to the cavity walls without change in composition). Although a gradient in composition with depth in the cavity may be expected for the case of cavity bleed, the experimental data were not considered adequate to develop a correlation for a distribution of water vapor content within the cavity.

Interpreting the values of T_o as an equilibrium flame temperature, a correlation for the water vapor mole fraction and average molecular weight in the 0.59- and 0.42-inch-wide cavities was developed. The predictions of this correlation are shown in Fig. 36 and 37. According to the correlation, the mole fraction of water vapor measured in Runs 23 and 24 (Table 9) must be considered in error by 0.02 to 0.03.

Because the gas composition in the cavity must approach the composition of the purge gas for sufficiently large flowrate, the flatness of these curves for high bleed flowrate appears unrealistic. However, this effect may be due to the limited distribution of the incoming bleed (two orifices), which may drive a recirculating flow in the cavity.

A comparison of the gas densities and sonic velocities calculated for the measured cavity compositions and average temperatures with the corresponding values calculated from Fig. 36 and 37 and the cavity temperature model are shown in Table 11 The agreement is within 10 percent except for Runs 23 and 24, the data from which have already been questioned in the paragraphs above.

*The region above the cavity opening is considered to be a mixing layer rather than the usual boundary layer because the cavities are located upstream of the wall attachment point of the main combustion gas flow.

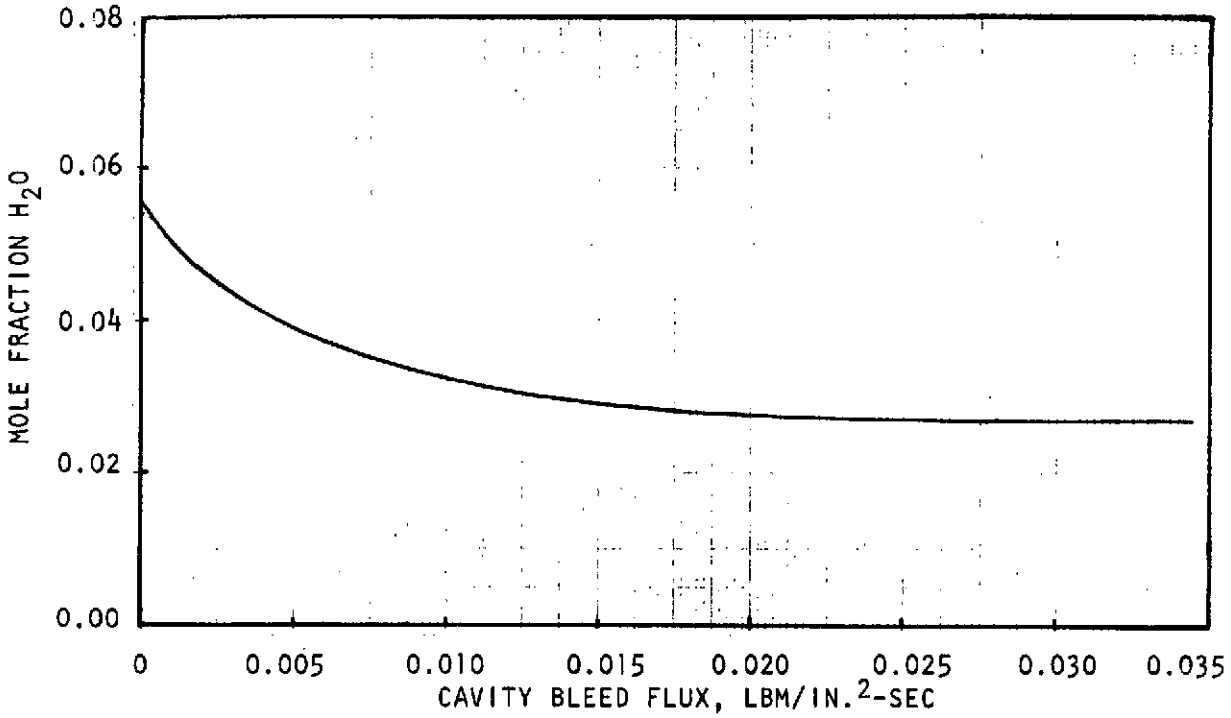

Figure 36. Predicted Variation of Water Content in Cavity Gas With Cavity Hydrogen Bleed Flux

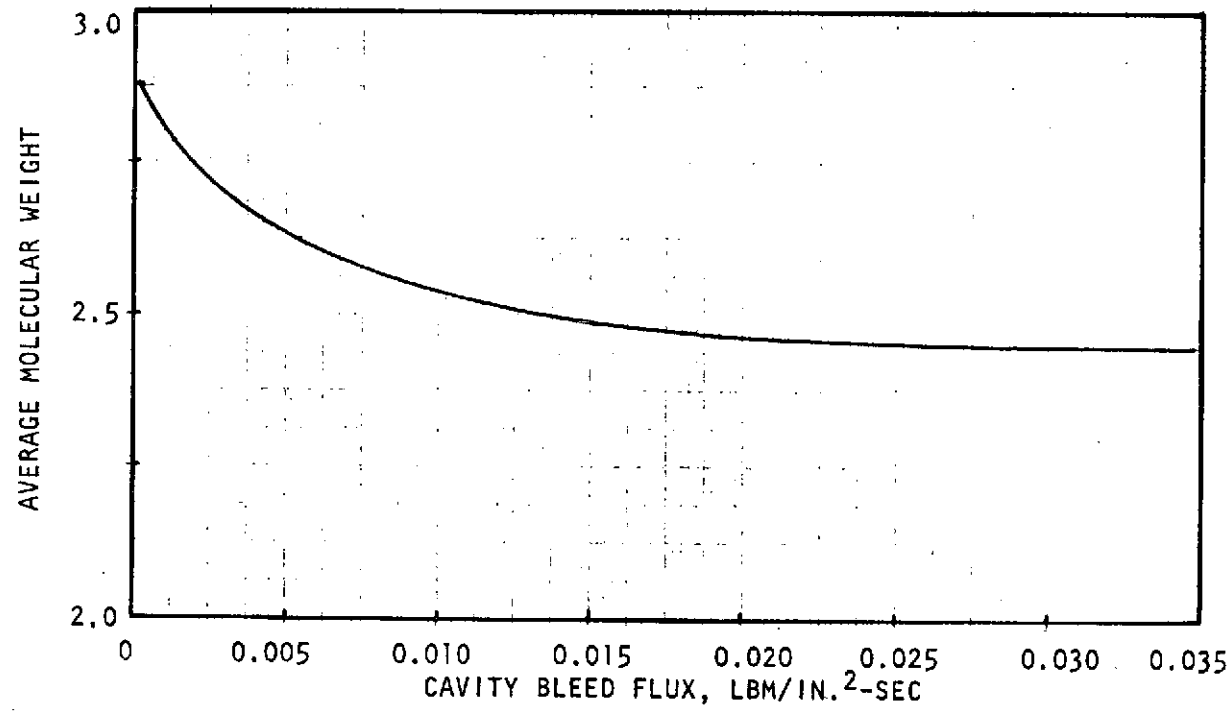

Figure 37. Predicted Variation of Cavity Gas Molecular Weight With Cavity Hydrogen Bleed Flux

TABLE II. COMPARISON OF GAS DENSITY AND ACOUSTIC VELOCITY CALCULATED FROM MEASURED CAVITY GAS TEMPERATURE AND COMPOSITION WITH VALUES CALCULATED FROM CORRELATIONS FOR TEMPERATURE AND MOLECULAR WEIGHT

Run	Gas Density Based on Measured Temperature and Composition, lbm/ft^3	Gas Density Based on Calculated Temperature and Composition, lbm/ft^3	Sonic Velocity Based on Measured Temperature and Composition, ft/sec	Sonic Velocity Based on Calculated Temperature and Composition, ft/sec
11	0.136	0.126	5360	5590
21	0.199	0.180	5330	5590
23	0.291	0.193	3960	4850
24	0.390	0.266	4050	4670
33	0.225 to 0.260	0.264	4990 to 4800	4660
36	0.314	0.307	4310	4355
38	0.334	0.339	4655	4660

CONCLUSIONS

The major objective of this program (i.e., experimental characterization of the density and sound velocity of the gases contained in acoustic cavities in H_2/O_2 combustor) has been achieved, although to a lesser extent than originally planned. Fewer data were obtained than originally planned because of unforeseen problems encountered in obtaining and fabricating the needed hardware. Nonetheless, sufficient data were obtained to provide a basis for at least preliminary future cavity designs. However, because the conditions within the acoustic cavities are likely to vary somewhat from engine to engine, additional cavity temperature measurements are desirable and are recommended for any future cavity-stabilized H_2/O_2 engines.

The following conclusions may be drawn from the data:

1. As expected from earlier, acoustic cavity and acoustic liner results, the temperature in the acoustic cavities was substantially below the thermodynamic equilibrium flame temperature corresponding to the overall mixture ratio. A maximum local temperature of 1510 F was measured in the acoustic cavity as compared to a flame temperature of 5800 F. Spatial averages of measured gas temperatures within the cavities ranged from 120 to 850 F.
2. The cavity temperature appears to decrease sharply with decreasing cavity width, based on limited data, and increasing cavity hydrogen bleed flowrate.
3. Measured cavity temperature was correlated, through the use of a heat transfer model, with the combustion flow field predicted by an analytical model for the steady-state combustion resulting from coaxial element injectors (the CSS combustion model).
4. Analysis of gas samples withdrawn from the cavities by a combination of pressure-temperature measurements and gas chromatography indicated the gas contained in the cavity is composed of 93.5 to 100 mole percent of hydrogen and 0 to 6.5 mole percent of water with only traces of atmospheric contaminants. The accuracy of the overall gas sampling technique is estimated to be approximately ±3 percent in hydrogen mole fraction.

RECOMMENDED DESIGN PRACTICE

The recommended approach for calculation of gas density and sonic velocity in cavities used in a H_2/O_2 engine system is:

1. Employ a steady-state combustion model (e.g., the CSS model) to calculate the axial temperature and mixture ratio profiles and the wall attachment point of the main gas flow field corresponding to the particular injector, thrust chamber, and operating conditions.
2. Choose a reference axial station for specifying the combustion gas flame temperature and (in the case of no cavity bleed) mixture ratio from the combustion model results. Until more data become available, a distance midway between the downstream edge of the cavity and the flow attachment point is recommended for this reference station.
3. Calculate the gas temperature at the entrance to the acoustic cavity, T_o, from the flame temperature at the reference station through the use of Fig. 38 which represents a nondimensionalized generalization of the curves of Fig. 32. The average cavity wall temperature, T_s, to be used with Fig. 38, may be taken as equal to the temperature of either the hydrogen bleed gas or the regenerative coolant around the cavity (if these are not nearly equal, the coolant temperature is probably preferable).
4. Determine the mixture ratio corresponding to temperature T_o from conventional thermodynamic equilibrium state conditions for the H_2/O_2 propellant combination as calculated, for example, by the JANNAF ODE computer program.
5. Calculate the mole fractions of hydrogen and water vapor in the cavity gas from the mixture ratio, employing the assumption that only hydrogen and water vapor exist in the cavity.
6. Calculate the average molecular weight of the cavity gas from the calculated composition:

$$\overline{MW} = 2.02\ (1.0 - X_{H_2O}) + 16.0\ X_{H_2O}$$

7. Calculate the temperature distribution and/or the mean cavity gas temperature from T_o and from Eq. 1 and/or 2, respectively.
8. The local and/or mean values of gas density and sonic velocity in the cavity may then be calculated from the usual ideal gas relations:

$$\rho = \frac{p_c\ \overline{MW}}{RT}$$

$$c = \sqrt{\frac{\gamma RT}{\overline{MW}}}$$

where

p_c = the static pressure at the cavity entrance which should be nearly equal to nominal injector end chamber pressure (but not the nozzle stagnation pressure)

γ = the specific heat ratio, can be assigned a value of 1.395 over the composition range of interest

9. With the cavity gas density and acoustic velocity defined in accordance with steps 1 through 8, the required cavity dimensions to produce a maximum cavity damping coefficient can be calculated by means of the computerized cavity damping model described in Ref. 1. The calculated results in terms of damping coefficient as a function of cavity depths and widths would be similar to the data shown in Fig. 1.

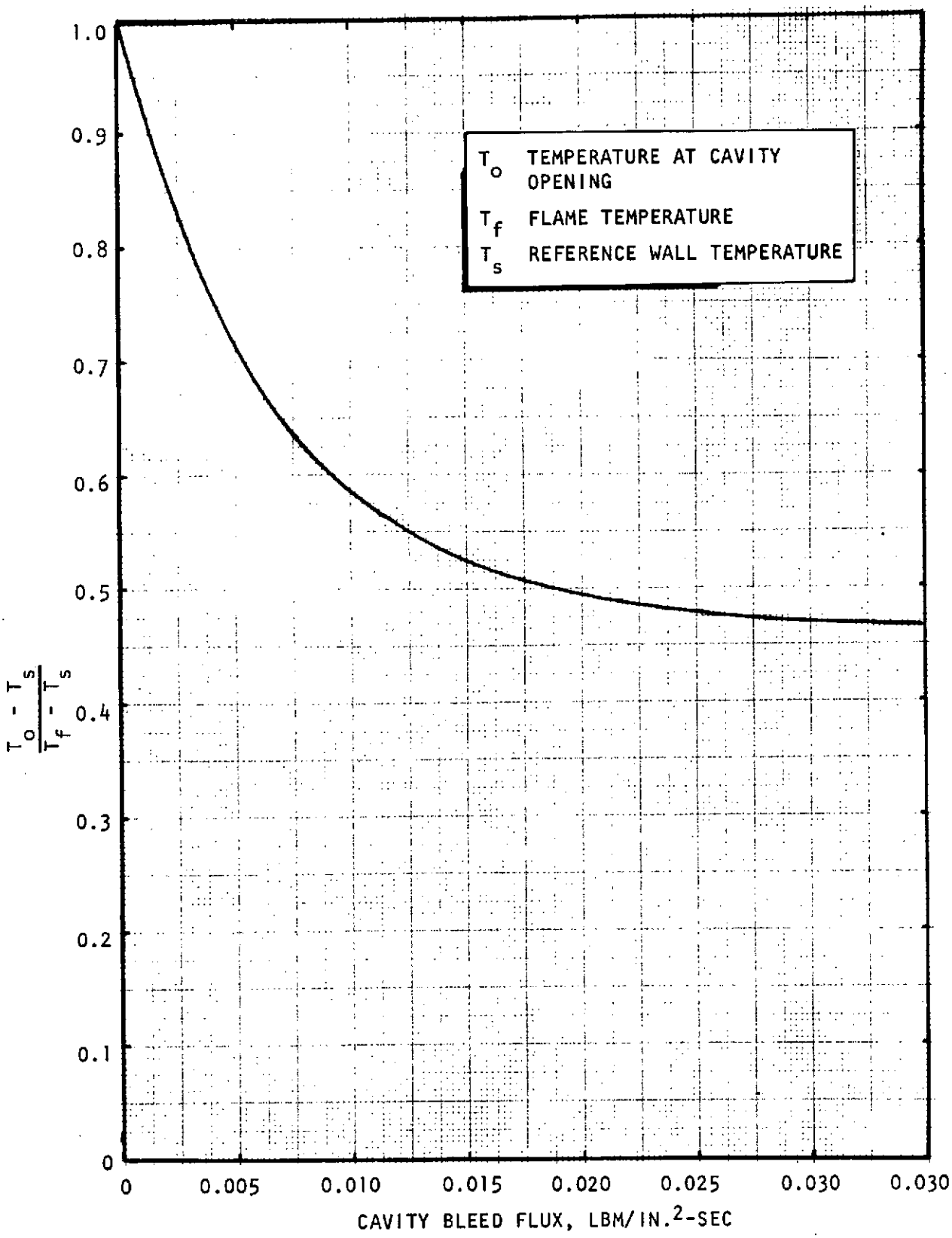

Figure 38. Generalized Correlation for Definition of Cavity Entrance Gas Temperature

REFERENCES

1. R-8416: Cast Segment Evaluation, Final Report, Contract NAS8-30182, Rocketdyne Division, Rockwell International, Canoga Park, California, February 1971.

2. R-7935: Lunar Module Ascent Engine Acoustic Cavity Study, Final Report, Contract NAS9-7498, Rocketdyne Division, Rockwell International, Canoga Park, California, August 1969.

3. Phillips, B.: Experimental Investigation of an Acoustic Liner With Variable Cavity Depth, NASA TN D-4492, National Aeronautics and Space Administration, Lewis Research Center, Cleveland, Ohio, April 1968.

4. R-8757: Evaluation of Acoustic Cavities for Combustion Stabilization, Final Report, NASA CR-115087, Rocketdyne Division, Rockwell International, Canoga Park, California, July 1970.

5. Sutton, R. D. and M. D. Schuman: "Liquid Rocket Combustion Analysis for Coaxial Jet Injection of Gas/Liquid Propellants," 7th JANNAF Combustion Meeting, CPIA Publication 204, Vol. 1, Chemical Propulsion Information Agency, Silver Springs, Maryland, February 1971.

APPENDIX A

CAVITY DAMPING MODEL

An analytical method was used for predicting the influence of an acoustic cavity configuration on engine stability. This method was based on an approximate separation of the damping effect of the cavities from the other stability related processes. This analytical approach concerns the use of analytical methods of linear acoustics to develop a quasi-linear model for cavity damping. A damping coefficient is calculated therefrom, which represents the damping or oscillatory energy dissipation contributed by the cavity exclusive of other stability related effects.

Cavity damping is estimated by approximate solution of an integral form of the time-independent wave equation (Helmholtz equation)*

$$\tilde{p}(\vec{r}) = \int G(\vec{r}|\vec{r}_o^{\,s})\ \vec{N}\ \nabla_o \tilde{p}(\vec{r}_o^{\,s})\ dS_o \qquad \text{(A-1)}$$

with the boundary conditions

$$\frac{\vec{N}\cdot\nabla\tilde{p}}{\tilde{p}} = \begin{cases} -j\,\dfrac{\beta}{c\zeta} & \text{at absorber} \\ 0 & \text{elsewhere} \end{cases}$$

The integral equation is solved by an iterational-variational technique. After insertion of appropriate expressions, and evaluting the integrals, this equation may be solved by standard root-finding methods to obtain the complex frequency or eigenvalue, the damping coefficient being proportional to the imaginary part of the eigenvalue.

By inserting an approximate expression in the integrand of the pressure expression (Eq. A-1) and evaluating the integral, an improved estimate is obtained. Thus, if $\xi^{(i)}$ is the i^{th} approximation for the pressure distribution at the entrance to a simple slot cavity, the i + 1 approximation is given by

$$\xi^{(i+1)} = -jky \int_S G(\vec{r}|\vec{r}_o)\ \xi^{(i)}\ (\vec{r}_o^{\,s})\ dS_o$$

Employing this notation, the variational characteristic equation may be written as

$$\int_S \xi^{(i)} \left|\xi^{(i)} - \xi^{(i+1)}\right| \ dS = 0$$

*A table of nomenclature for this Appendix is given at the end of the Appendix.

An iterative form of the characteristic equation for a radial slot cavity was used for the calculations done during this program, it being

$$\sum_{q,\eta} a_{\bar{m}q}^{(i)} \left| a_{\bar{m}\eta}^{(i)} - a_{\bar{m}\eta}^{(i+1)} \right| I_{q\eta} = 0$$

where

$$a_{\bar{m}q}^{(i+1)} = -jky\, \varepsilon_q \frac{J_{\bar{m}}(k_{\bar{m}q} r_w)}{k_{\bar{m}q} J'_{\bar{m}}(k_{\bar{m}q} r_w)} \sum_{\eta} a_{\bar{m}\eta}^{(i)} I_q$$

$$I_{q\eta} = \int_{z_s} \cos \frac{q\pi z}{L} \cos \frac{\eta\pi z}{L} \frac{dz}{L}$$

$$k_{\bar{m}q} = \sqrt{k^2 - \frac{q^2\pi^2}{L^2}}$$

and

$$a_{\bar{m}q}^{(0)} = \begin{cases} 1.0 & q = \bar{\eta} \\ 0 & q \neq \bar{\eta} \end{cases}$$

The Bessel function ratio was evaluated from the following expansion developed in Ref. A-1.

$$\frac{J_{\bar{m}}(k_{\bar{m}q} r_w)}{k_{\bar{m}q} J'_{\bar{m}}(k_{\bar{m}q} r_w)} = r_w \sum_{n} \frac{2\alpha_{\bar{m}n}^2}{(\alpha_{\bar{m}n}^2 - \bar{m}^2)(\alpha_{\bar{m}n}^2 - k_{\bar{m}q}^2 r_w^2)}$$

The damping coefficient is obtained by solving the characteristic equation for the allowed frequencies or eigenvalues, i.e.,

$$\phi = k r_w = (\omega + j\alpha)\, r_w / c$$

This characteristic equation applies to either standing or spinning modes of instability; the same damping coefficient is obtained in either case. A nonlinear expression for the cavity impedance, ζ, is used. This expression was obtained by analogy with the corresponding expression for a Helmholtz resonator. The impedance of the latter resonator is composed of a nonlinear resistance because of the jet losses and a linear reactance, at least in form. The linear reactance expression for a slot cavity may be obtained by solving the wave equation for the cavity. By adding a

nonlinear resistance term, an analogous specific impedance expression is obtained for a slot. For a partitioned, straight slot cavity configuration, it is

$$\zeta = \theta_1 - j\,[(\rho c)_s/\rho c]\,[\cot\,(\ell_s/r_w)(c/c_s)\phi]$$

The specific resistance θ_1 is written as

$$\theta_1 = \Gamma \hat{M}_s (\rho c)_s/\rho c$$

where $\hat{M}_s$ is the peak Mach number at the open end of the slot and Γ may be estimated analytically (Ref. A-2) or from impedance measurements (Ref. A-3).

For all of the damping calculations, the specific resistance of the cavity has been evaluated in terms of the local pressure amplitude. This has been done by solving the impedance expression,

$$\frac{\tilde{p}}{\rho c \tilde{u}_s} = \frac{\tilde{p}}{\gamma p_o \tilde{M}_s} = \theta + j\chi$$

for the velocity amplitude, noting that $\theta = \Gamma \hat{M}_s$. The amplitudes of the complex equations are obtained from their absolute values; thus

$$\left(\frac{\hat{p}}{\gamma p_o \hat{M}_s}\right)^2 = \left(\Gamma \hat{M}_s - \chi''\right)^2 + \left(\chi'\right)^2$$

where the substitution $\chi = \chi' + j\chi''$ has been made. By rearrangement

$$\left(\Gamma \hat{M}_s\right)^4 - 2\chi'' \left(\Gamma \hat{M}_s\right)^3 + \left(\chi''^2 + \chi'^2\right)\left(\Gamma \hat{M}_s\right)^2 - \left(\frac{\Gamma \hat{p}}{\gamma p_o}\right)^2 = 0$$

The last equation is solved by a numerical root finding method to determine the amplitude of the oscillating Mach number in the aperture and, therefrom, the specific resistance. Note that $\hat{p}$ and Γ appear as a combined nondimensional parameter in the calculation. Therefore, they may have interchangeable roles.

For the current program the radial cavity was treated as a partitioned, straight slot. The axial cavity was treated as an L-shaped resonator with a generalized reactance expression being used.

This reactance expression was developed for a resonator shape of the following form (two-dimensional):

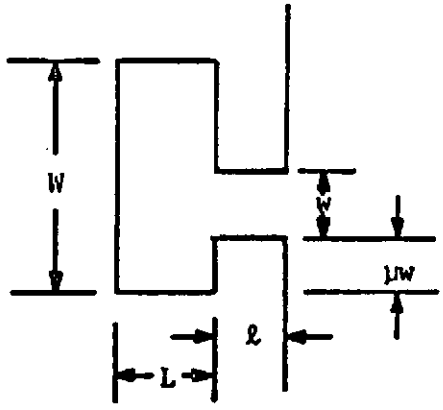

$$\chi = \frac{\tan k\ell - \sum_m \frac{\varepsilon_m}{wW} \frac{kA_{om}^2}{k_m \tan k_m L}}{1 + \tan k\ell \sum_m \frac{\varepsilon_m}{wW} \frac{kA_{om}^2}{k_m \tan k_m L}}$$

where

$$A_{om} = \int_{\mu w}^{(\mu+1)w} \cos \frac{m\pi y}{w} \, dy$$

This represents a zero-iteration approximation. An iterated form was also developed. The axial cavity was analyzed with L = w and μ = 0.0.

APPENDIX A REFERENCES

A-1. Oberg, C. L. and N. M. Kuluva: Analysis of F-1 Acoustic Liner," J. of Spacecraft and Rockets, Vol. 8, 11, pp. 1138-43, November 1971.

A-2. Oberg, C. L.: "Combustion Stabilization With Acoustic Cavities," J. of Spacecraft and Rockets, Vol. 12, pp. 1220-5, December 1971.

A-3. Oberg, C. L, W. G. Haymes, and T. L. Wong: "Solid Propellant Combustion Stability Suppression Devices," AIAI Paper No. 72-1051, presented at AIAA/SAE 8th Joint Propulsion Specialist Conference, New Orleans, November 29 to December 1, 1972.

NOMENCLATURE FOR APPENDIX A

a_{mq}	series coefficient
c	acoustic velocity
$G(\vec{r}\|\vec{r}_o)$	Green's function
I	Integral
$J_m(\ )$	Bessel function of first kind and order m
j	$(-1)^{1/2}$
k	β/c
L	chamber length
$\hat{M}_s$	peak oscillatory Mach number in slot
$\vec{N}$	unit normal vector
p	pressure
$\vec{r}$	position vector
S	surface area of acoustic cavity
z	axial chamber coordinate
β	complex angular frequency
Γ	resistance coefficient
γ	specific heat ratio
θ	specific resistance
ζ	specific impedance
χ	cavity reactance
ϕ	eigenvalue
$\xi^{(i)}$	ith approximation to pressure
ω	angular frequency

Subscripts

m,n,q,η	indices pertaining to eigenvalues
w	wall
o	source

APPENDIX B

CSS STEADY-STATE COMBUSTION MODEL FOR CONCENTRIC TUBE INJECTION ELEMENTS

The CSS computer program (Ref. B-1) calculates the atomization and subsequent vaporization downstream from a concentric tube-gas/liquid injection element, as shown in Fig. B-1. The analysis is quasi-one-dimensional, implying the assumption that recirculation and/or stratification of the mixture of injection gaseous propellant and gaseous combustion products are both negligible, which should be valid for closely spaced injection elements. Input data are required describing the physical and thermochemical properties of the propellants and equilibrium combustion products together with the geometry of the injector element and combustion chamber. The analysis includes treatment of any transpiration coolant supplied at the injector face.

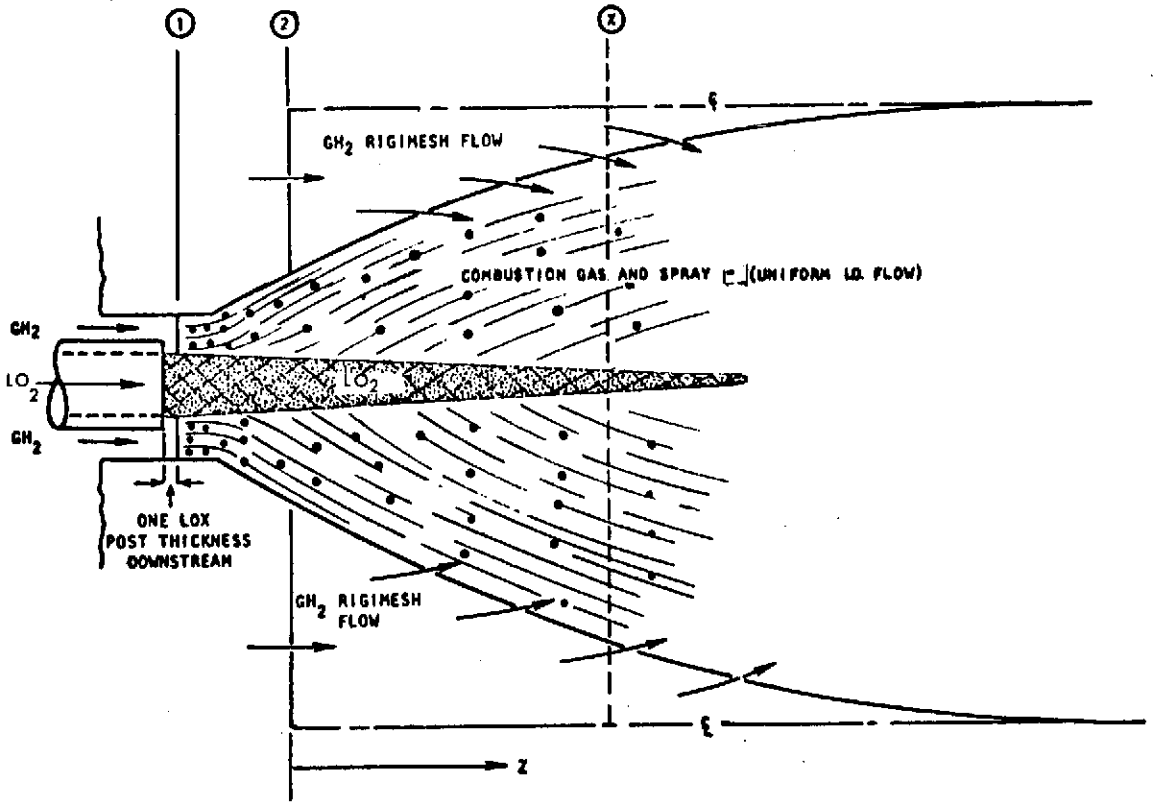

Figure B-1. Conceptual Model of Uniformly Flowing Coaxial Injector Element

The analysis is begun at point of initial contact between the concentric gas and liquid streams (Fig. B-1). This contact usually occurs in the "cup region," formed by recessing the liquid oxidizer post. In this region, the high velocity gas stream

begins stripping and atomization of the liquid jet. These processes must be included in the analysis. Small drops are formed and, depending on local flow and geometric conditions and flame speed, the propellants may ignite within the cup. Even when burning does not occur in the cup, the constrained two-phase flow has a significant effect on atomization and subsequent combustion in the main chamber.

In the analysis the gaseous fuel is assumed to fill the annular area between the jet and fuel cup. Conservation equations for both the liquid jet and combustion gas/spray flow in the cup region and chamber flows are utilized in the model, which include spray droplet atomization, heating, burning, and droplet drag. In the chamber, the radial pressure is assumed to be uniform at each axial location and the sum of the cross-sectional areas of the liquid jet, combustion/spray field and transpiration ("Rigimesh") flow (for which conservation equations are also supplied) following solution of all the conservation equations is required to equal the cross-sectional area of the chamber. However, if no Rigimesh flow is used in the injector, in the analysis the combustor flow field emanating from an element is allowed to expand at constant pressure until the flow fills the chamber.

Equations are included in the model to describe the liquid stripping rates from the jet and the resultant dropsize distribution. Consequently, input data regarding dropsize information are not required; rather, the distribution is calculated as a function of flow field conditions and jet axial position. The controlling parameters in the model are: (1) the stripping rate of the liquid jet, M_A; (2) the mean dropsize produced by stripping from the jet, $\bar{D}$; (3) the droplet heating and burning rates; (4) the droplet drag coefficient; and (5) the rate of mixing of the Rigimesh flow with the element flow.

A correlation for the droplet drag coefficient is utilized which was obtained from measurements on accelerating, burning droplets in a convective flow field (Ref. B-1). The rate of mixing of the Rigimesh flow is important only if that flow is abnormally large but it must be specified at any level.

An improved burning (and heating) rate drop model is used which may be used for both subcritical and supercritical conditions and which allows steady-state combustion analyses and performance predictions to be made up to 5000 psia pressure or greater. The equations are similar to the familiar El Wakil equations (Ref. B-3), but the boundary condition has been changed to allow for the existence of an external mass flux. This change allows smooth computation through the critical point. Additionally, allowance is made for high-pressure effects, due to the presence of other gases, in the computation of the vapor surface mole fraction and the "heat of vaporization." This has been done through use of the Redlich-Kwong equation of state and fugacity relationships (Ref. B-4).

The expressions being used for the rate of jet stripping and the resultant drop sizes are shown at the top of the next page.

A. STRIPPING RATE

$$M_A \sim C_A \left[\frac{\mu_j (\rho_g U_r^2)^2}{\sigma_j/\rho_j}\right]^{1/3} \pi D_j (\Delta Z)$$

C_A: ATOMIZATION COEFFICIENT

B. MEAN DROP SIZE

$$\bar{D}_n \sim B_A \left[\frac{\mu_j (\sigma_j/\rho_j)^{1/2}}{\rho_g U_r^2}\right]^{2/3}$$

B_A: DROP SIZE COEFFICIENT

The coefficients C_A and B_A are regarded as empirical coefficients to be obtained from available data. The remaining parameters in each expression are calculated in the model. Different values for C_A and B_A are used in the cup region and in the chamber because the fuel is not constrained in the chamber as it is in the cup.

Values for B_A and C_A for the cup region have been determined from two sets of data existing for the cup ΔP in the injector of large LO_2/hydrogen with concentric tube injection elements. The ΔP was determined experimentally by comparison of the injection pressure drop with and without post recess and at equivalent operating condition. Consistent pairs of B_A and C_A were determined which, when used in the model, predicted the values of ΔP as the measured values. The curves of C_A versus B_A for the two engines were then plotted on the same graph to locate their intersections, which were taken as the best values for these coefficients and assumed valid for a wide range of engines. With these values for the coefficients, in the cup region, the values of C_A and B_A for the chamber were then determined for two separate but similar coaxial injectors by comparison of measured and predicted c* efficiencies in short thrust chambers. Finally, the validity of the resultant values of C_A and B_A for both the cup and main chamber was confirmed by comparison of predicted and measured results for a range of chamber pressures, injector element geometries and thrust chamber configurations.

The CSS model represents an advancement over conventional spray combustion models in that both the atomization and vaporization in the region close to the injector, wherein most of liquid is initially confined as a continuous jet with limited gas contact, are analyzed whereas most analyses begin downstream at the axial station where fully developed spray is assumed to have been formed.

APPENDIX B REFERENCES

B-1. Sutton, R. D. and M. D. Schuman: "Liquid Rocket Combustion Analysis for Coaxial Jet Injection of Gas/Liquid Propellants," 7th JANNAF Combustion Meeting, CPIA Publication 204, Vol. 1, Chemical Propulsion INformation Agency, Silver Springs, Maryland, February 1971.

B-2. Rabin, E. A. et al.: Displacement and Shattering of Propellant Droplets, AFOSR-TR-60-75, Rocketdyne Division, Rockwell International, Canoga Park, California, 1960.

B-3. El Wakil, M. M.: Experimental and Calculated Temperatures and Mass Histories of Vaporizing Fuel Droplets, NACA TN 3480, January 1956.

B-4. Chueh, P. L. and J. M. Prausnitz: "Calculation of High-Pressure Vapor-Liquid Equilibria," Industrial and Engineering Chemistry, Vol. 60, 1968, pp. 34-52.

APPENDIX C

PRIEM-GUENTERT COMBUSTION STABILITY MODEL

The Priem-Guentert model (Ref. C-1) for analysis of transverse combustion instability in rocket engines was formulated in terms of conservation equations for two-phase flow in a stationary annular volume element of very small axial length and thickness. In this thin annular element, variations of the dependent variables in the tangential directions were retained but gradients in the radial and axial directions were neglected. A quasi-steady-state propellant vaporization rate, expressed as a function of the axial velocity difference (ΔV) between the combustion gas and liquid droplets, is used to represent the burning rate of the propellant. The normalization of the set of nonlinear equations for the combustion pressure yielded a number of parametric groups. When the controlling equations were solved on a high speed digital computer, zones of engine operating conditions were found in which a tangential instability was predicted to be initiated by an initial pressure disturbance. The boundaries of the unstable zones were found to depend on certain of the parametric groups, notably $\mathcal{L}$, the burning rate parameter, and $\Delta V'$ ($\Delta V' = \Delta V/c$), where c is the local speed of sound). The burning rate parameter, $\mathcal{L}$, is defined as:

$$\mathcal{L} \equiv \frac{mR}{CR}$$

where

m = fraction of total propellant burned per unit length of combustor

R = radius of combustor (or annular element)

CR = combustor contraction ratio

Stability maps were obtained by plotting the neutral stability limit, A_p (the minimum reduced pressure disturbance amplitude required to initiate a sustained instability) versus the burning rate parameter, $\mathcal{L}$, for various values of $\Delta V'$. An example of such neutral stability curves is shown in Fig. C-1. Note that stability is lowest when the burning rate is high but the gas-liquid velocity difference is low.

Because $\Delta V'$ and $\mathcal{L}$ are both functions of distance from the injector (these parameters may be calculated with the aid of appropriate steady-state spray combustion models), the stability maps in $\Delta V'$ versus $\mathcal{L}$ parameter space can be converted into stability maps in real space within the combustion chamber.

Work at Rocketdyne (Ref. C-2) has eliminated several of the simplifying assumptions employed by Priem in the initial development of his model. The vector form of the equations used by Priem was converted to Cartesian coordinates to permit a computerized solution for rectangular combustors (such as the linear aerospike thrust chamber of this program) comparable to the solutions obtained for the usual cylindrical chamber. Also, the nondimensional burning rate expression used by Priem, which was

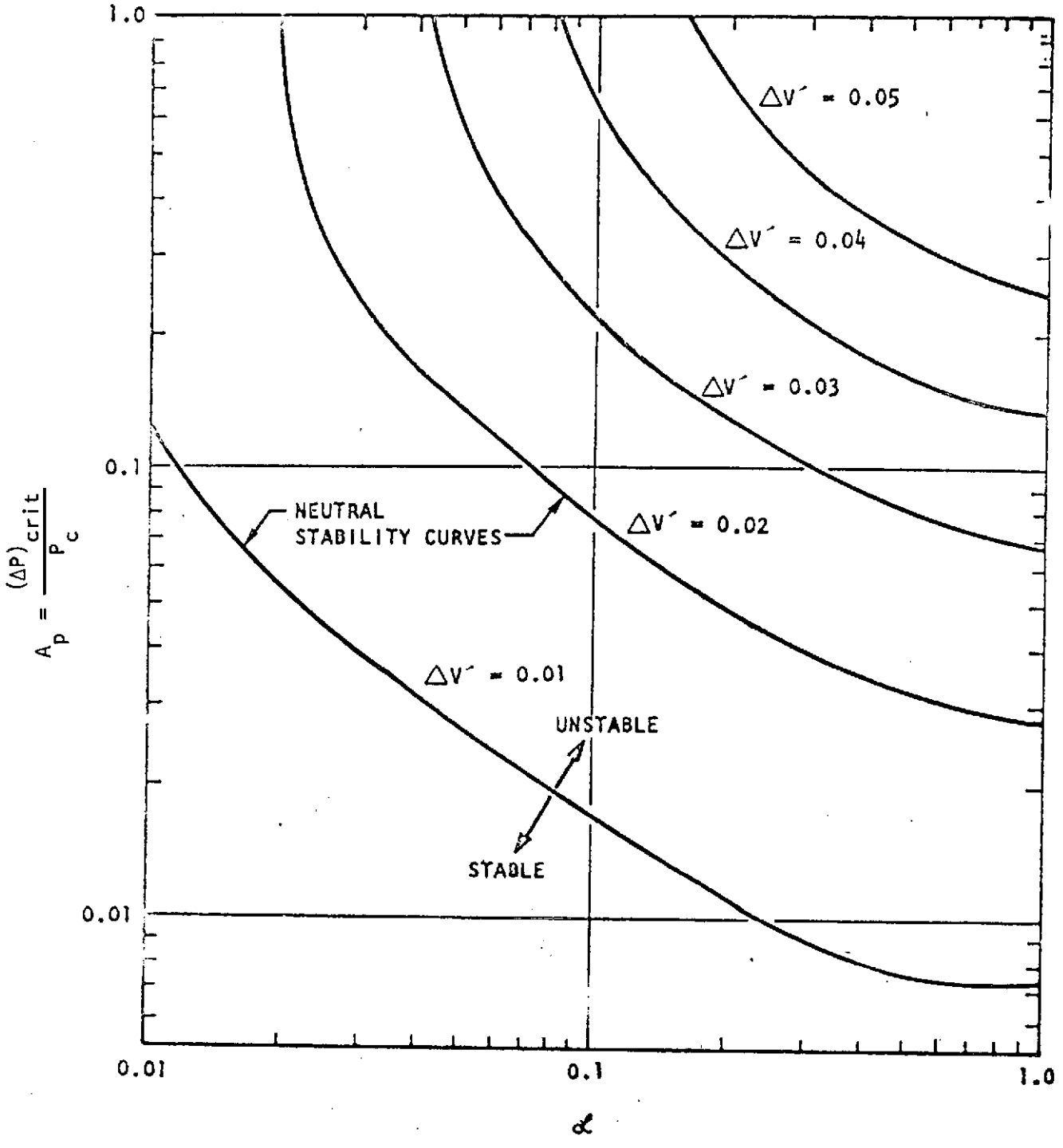

Figure C-1. Typical Neutral Stability Limit Curves

invalid for low $\Delta V'$ (where stability limits are critical), has been extended to apply to any relative velocity. In addition, the Priem model was modified to include the effects of gas/spray drag. With these model extensions, the overall stability index A_p was defined graphically through numerous calculations in terms not only of the primary dimensionless parameters $\mathcal{L}$ and $\Delta V'$, but also of the secondary parameters MAP, K_1, K_2, and K_3, which are defined by:

$$MAP = \frac{M_{VAP}\ c}{2\pi R \times \text{injection density}}$$

$$K_1 = 3.33\ Sc^{-1/3}\ Re^{-1/2}$$

$$K_2 = \frac{3\ C_D\ R\ M_{VAP}}{4\rho D}$$

$$K_3 = \frac{3\ C_D\ R\rho}{4(\rho D)_{drop}}$$

where

C_D = droplet drag coefficient

D = droplet diameter

M_{VAP} = density flux of unvaporized propellant

Re = Reynolds number based upon drop diameter and sound velocity

Sc = Schmidt number

ρ = gas density

APPLICATION OF THE PRIEM MODEL

To apply the Priem model, the steady state gas flow field is usually determined through use of steady-state spray combustion models such as the CSS coaxial element analysis (described in Appendix B) or the DER computer program (Ref. C-3). These steady state models predict the variation with axial position of gas velocity, fraction of propellant burned, gas density, mass concentration of unburned propellant, drop size and drop velocity. From these quantities, the values of the parameters, $\mathcal{L}$, $\Delta V'$, MAP, K_1, K_2, and K_3 may be calculated at each axial location.

As shown in Fig. C-1, the value of $\Delta V'$ has a large effect on the stability limits. Ordinarily, the axial location where the absolute value of $\Delta V'$ is a minimum is the most sensitive region of the combustor; in fact, the model always predicts instability where $\Delta V'$ is equal to zero. However, because of both turbulence and three-dimensional effects, $\Delta V'$ cannot reasonably go to zero for a given axial station; consequently, a minimum value of 0.01 (corresponding to the level of turbulence measured by Hersch (Ref. C-4) in a rocket combustor) is assigned to the most sensitive zone.

Graphical correlations of previously calculated numerical results have been developed which allow A_p to be calculated from $\mathcal{L}$, $\Delta V'$, K_1, K_2, and K_3. The resultant value of A_p can then be plotted as a function of axial location such as that shown in Fig. 13 and 14 of this report.

APPENDIX C REFERENCES

C-1. Priem, R. J. and D. C. Guentert: Combustion Instability Limits Determined by a Non-Linear Theory and One-Dimensional Model, NASA TN D-10409, October 1962.

C-2. Coultas, T. A. and R. C. Kesselring: "Extension of the Priem Theory and Its Use in Simulation of Instability on the Computer," Second ICRPG Combustion Conference, Aerospace Corp., El Segundo, California, CPIA Pub. No. 105, May 1966.

C-3. Combs, L. P.: "Liquid Rocket Performance Computer Model With Distributed Energy Release," Final Report for Contract NAS7-746, NASA CR-114462, Rocketdyne Division, Rockwell International, Canoga Park, California, June 1972.

C-4. Hersch, M.: "An Experimental Method of Measuring Intensity of Turbulence in a Rocket Chamber," ARS Journal, 31, 1 January 1961, pp. 39-46.

APPENDIX D

ESTIMATION OF THE EXTENT OF SIDEWALL COOLANT LEAKAGE

The extent of coolant leakage through cracks that developed during the test program can be estimated from an overall heat balance. Each of the sidewalls of the linear aerospike thrust chamber were cooled by hydrogen gas that flowed from an inlet manifold at the nozzle throat, up to and around the acoustic cavity openings, through a critical flow orifice, and then discharged to the atmosphere. The weight flow of hydrogen gas that was actually discharged, $\dot{w}_M$, was determined with a critical flow orifice, by means of temperature and pressure measurements immediately upstream of the orifice. The temperature of the gas before entry into the sidewall coolant passages, T_i, was also measured in the manifold at the nozzle exit.

Assuming little heat transfer occurs within the cavities, an overall energy balance may be written as

$$\int_A (q/A)\, dA = \dot{w}_R c_p \Delta T_c \qquad \text{(D-1)}$$

where the left side of the equation is the integral of the local gas side heat flux over the sidewall, $\dot{w}_R$ is the real flow of hydrogen through the sidewall coolant passages, and ΔT_c is the temperature rise from the throat to the critical orifice thermocouple. The local heat transfer coefficient, h, is defined by

$$q/A = h\, \Delta T_f \qquad \text{(D-2)}$$

where ΔT_f is the gas-to-wall temperature potential. Correlations for the heat transfer coefficient are available which may be written as

$$h = C_h P_c^{0.8} \qquad \text{(D-3)}$$

or

$$\frac{h}{P_c^{0.8}} = C_h, \text{ a constant} \qquad \text{(D-4)}$$

Moreover, if the variation of ΔT_f throughout the series of motor firings* is neglected, then

$$\frac{q/A}{P_c^{0.8}} = C_h \Delta T_f, \text{ a constant} \tag{D-5}$$

from which

$$\frac{1}{P_c^{0.8}} \int_A (q/A)dA = C_2, \text{ a constant} \tag{D-6}$$

Substituting Eq. D-1 into Eq. D-6

$$\frac{c_p \dot{w}_R \Delta T_c}{P_c^{0.8}} = C_2 \tag{D-7}$$

or, finally

$$\frac{\dot{w}_R \Delta T_c}{P_c^{0.8}} = C_3, \text{ a constant}$$

The last approximate relationship is useful because, if leakage of coolant hydrogen occurred at the open end of the acoustic cavities, then $\dot{w}_M$ would be less than $\dot{w}_R$. The variation of the quantity $(\dot{w}_M \Delta T_c/P_c^{0.8})$ through the course of the motor firing program is, therefore, a measure of the degree to which leakage was developing. A corresponding normalized parameter, ψ, was defined by

$$\Psi = \frac{(\dot{w}_M \Delta T_c/P_c^{0.8})_{\text{individual test}}}{(\dot{w}_M \Delta T_c/P_c^{0.8})_{\text{average for all tests}}} \tag{D-8}$$

This nondimensional form of the expression was used for the actual comparison.

*Although ΔT_f varies with mixture ratio, the product $C_h \Delta T_f$ is relatively independent of mixture ratio.

APPENDIX E

CAVITY GAS TEMPERATURE ANALYSIS

An approximate one-dimensional analytical model for the temperature distribution within the acoustic cavity was developed to aid rational correlation of the temperature data. This model was developed from the elemental energy balance shown in Fig. E-1.

The following assumptions were employed:

1. An essentially one-dimensional temperature variation, in the y direction of Fig. E-1.
2. No chemical reaction within the cavity
3. Constant wall temperature, which implies sufficient heat sink effect of the cavity walls to maintain the surface temperature everywhere within the cavity close to its initial temperature, T_{so}.
4. Constant average values for the overall thermal conductivity k_T within the core of the cavity gas volume and the gas-to-wall heat transfer coefficient, $\bar{k}_T$ and $\bar{h}$.
5. Stepwise change in gas composition at the open end of the cavity produced by hydrogen gas bleed at the bottom of the cavity.

Accordingly, a differential heat balance may be written as

$$\bar{k}_T A_c \frac{d^2T}{dy^2} = \bar{h}P\,(T-T_{so}) - C_p\,\dot{w}_{H2}\,\frac{dT}{dy} \qquad \text{(E-1)}$$

where P and A_c are the perimeter and cross-sectional area of the cavity, respectively. By rearrangement

$$\frac{d^2T}{dy^2} - \frac{\bar{h}P}{\bar{k}_T A_c}(T-T_{so}) + \frac{C_p}{\bar{k}_T}\left(\frac{\dot{w}_{H2}}{A_c}\right)\frac{dT}{dy} = 0 \qquad \text{(E-2)}$$

Because T_{so} is assumed constant,

$$dT = d(T-T_{so}) = d\Delta T$$

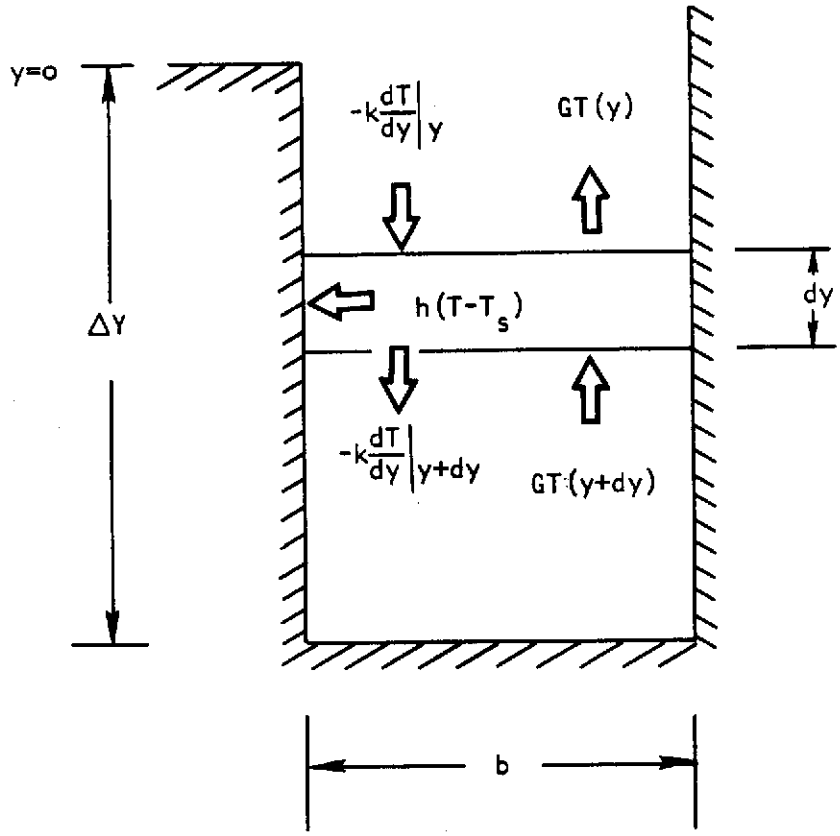

NOTE: $G = \dot{w}_{H2}/A_c$

Figure E-1. Elemental Heat Balance Used to Model Cavity Gas Temperature Distribution

and Eq. E-2 may be rewritten as

$$\frac{d^2\Delta T}{dy^2} + \frac{C_p}{\bar{k}_T}\left(\frac{\dot{w}_{H2}}{A_c}\right)\frac{d\Delta T}{dy} - \frac{\bar{h}P}{\bar{k}_T A_c}\Delta T = 0 \qquad \text{(E-3)}$$

The general solution to Eq. E-3 may be written as

$$\Delta T = A \exp\left[\frac{\left(-C_1 + \sqrt{C_1^2 + 4C_2}\right)y}{2}\right] + B \exp\left[\frac{\left(-C_1 - \sqrt{C_1^2 + 4C_2}\right)y}{2}\right]$$

where $C_1 = C_p\, \dot{w}_{H2}/\bar{k}_T A_c$, $C_2 = \bar{h}P/\bar{k}_T A_c$, and A and B are to be determined from the boundary conditions. Because ΔT must go to zero as y approaches infinity (i.e., at the bottom of very deep cavities), A = 0. Also, at y = 0, $\Delta T = \Delta T_o$. Therefore, the solution may be written as

$$\Delta T(y) = \Delta T_o \exp\left[\frac{\left(-C_1 - \sqrt{C_1^2 + 4C_2}\right)y}{2}\right] \qquad \text{(E-4)}$$

The coefficient C_2 varies with cavity dimensions as

$$C_2 = K_2\left(\frac{P}{A_c}\right) \qquad \text{(E-5)}$$

where

$$K_2 = \bar{h}/\bar{k}_T$$

Similarly, the coefficient C_1 varies with cavity bleed flowrate as

$$C_1 = K_1\left(\frac{\dot{w}_{H2}}{A_c}\right)$$

where

$$K_1 = C_p/\bar{k}_T$$

However, Eq. E-4 has been developed as a theoretically based expression to be used in correlation of the cavity temperature data. Therefore, the coefficients K_1 and K_2, have been treated as empirically determined parameters. For this purpose the latter expression has been generalized, with the addition of another parameter, to

$$C_1 = K_1\left(\frac{\dot{w}_{H2}}{A_c}\right)^n \qquad \text{(E-6)}$$

Accordingly, the cavity gas temperature may be expressed as

$$T = T_{so} + (T_o - T_{so}) \exp\left[-\frac{K_1}{2}\left(\frac{\dot{w}_{H2}}{A_c}\right)^n - \sqrt{\frac{K_1^2}{4}\left(\frac{\dot{w}_{H2}}{A_c}\right)^{2n} + K_2\left(\frac{P}{A_c}\right)y}\right] \quad \text{(E-7)}$$

The average temperature over any portion of the cavity ($y_1 < y < y_2$) is given by

$$\overline{T}_y = \left(\frac{1}{y_2 - y_1}\right) \int_{y_1}^{y} T \, dy \quad \text{(E-8)}$$

where T is given by Eq. E-7. The coefficients K_1, K_2, and n have been determined by curve fitting the temperature data to Eq. E-7 and E-8.